Imperial College of London
Materials Department

Metrology of the Electrocaloric Effect Based on an Infrared Imaging Technique

Maciej Konstanty Rokosz

Submitted in part fulfilment of the requirements for
the degree of Doctor of Philosophy of
the Imperial College London, December 2016

The copyright of this thesis rests with the author available under a Creative Commons Attribution Non-Commercial No Derivatives licence. Researchers are free to copy, distribute or transmit the thesis on the condition that they attribute it, that they do not use it for commercial purposes and that they do not alter, transform or build upon it. For any reuse or redistribution, researchers must make clear to others the licence terms of this work.

©Copyright by Maciej K Rokosz 2016

Abstract

In recent years the electrocaloric effect has gained the substantial interest of researchers due to its potential applications in commercial cooling. The high theoretical efficiency of electro-thermal conversion places this phenomenon as a potential alternative to commercial vapour-compression refrigerators. Success in such solid state cooling is anticipated to lead to global scale energy savings and reduction in the emission of greenhouse gases.

Most of the focus has been directed towards the achievement of high values of the electrocaloric effect temperature change ΔT_{EC}. High values of around 10 K and more have been reported. However little attention has been given to the methods of measurements and their uncertainties.

This work aims to use a metrological approach to study the electrocaloric phenomenon, to compare certain methods and to explore these measurements and their uncertainties. There are various ways to quantify the electrocaloric effect and various parameters influence the direct measurements of ΔT_{EC}. Here a direct method using infrared imaging is employed for the spatial and time-resolved temperature measurements of electrocaloric bodies. A set of the parameters influencing theΔT_{EC} is determined. Based on these quantified contributions, an uncertainty for such measurements is reported. The calibration of the imager is performed to validate the traceability of measurements, and a further set of characterisation apparatus was implemented to establish its performance.

A bulk $Ba_{0.65}Sr_{0.35}TiO_3$ sample was employed as a cross reference specimen in an inter-laboratory comparison involving infrared imaging and two types of differential scanning calorimetry.

Within the scope of this work, two commercial ceramic material compositions were characterised; a multilayer capacitor and a PMN-PT ceramic. First, $BaTiO_3$ in form of a multilayer ceramic capacitor was used to establish the optimal performance of such a structure and to investigate the in-situ measurements. In this measurement there were substantial differences in ΔT_{EC} depending on where on the sample (surface vs. interior) the measurement was made and an explanation for this difference is suggested. Second, the polycrystalline $Pb(Mg_{1/3}Nb_{2/3})-PbTiO_3$ ceramic sample was used investigate other sources of uncertainties arising from the mechanical coupling during electrocaloric measurements, estimated to account for up to 20% of the observed electrocaloric effect.

Acknowledgements

To Imperial College London and National Physical Laboratory for the scholarship under the Partner Research Institution (PRI) Scheme are acknowledged. Also appreciation for the funding from European Metrology Research Programme (EMRP) Project NEW09 METCO. The EMRP is jointly funded by the EMRP participating countries within EURAMET and the European Union.
The author would like to thank Syfer Ltd., for providing multilayer ceramic capacitors and supporting information.

I would like to greatly thanks to my all supervisors, Dr Tatiana Correia, Dr Jenny Wooldridge, Dr Alexandre Cuenat, Dr Andrey Berenov and Prof Neil Alford, for all the encouragement, inspirations and support throughout my PhD journey.
Especially many thanks to Dr Correia for help in enabling a collaboration with Imperial College London, which led eventually to this PhD. Also for great support at emerging researcher career by building up good habits and for the inspiration with Electrocalorics.

Furthermore, I would like to thanks to my dear colleagues and friends from National Physical Laboratory for all the coffee breaks (scientific discussions), advice, challenges, training etc. especially to Till Buchacher, Rob Simpson, Hector Leon Corte, Mark Steward, Peter Woolliams, Kevin Lees, Ekaterina Selezneva, Greg Walsh and many, many more.
Lastly to my parents and family for their support during the PhD time!

'Życie to proces stawania się sobą na miarę jaką sobie wyznaczasz.'

Adam Dębowski

'The solution becomes obvious once we assume that the cube is massless and in a vacuum.'[1]

Jason Hempstead

'The starting point of all achievement is desire.'

Napoleon Hill

[1]Source: http://www.theboobcube.com/solutions.html

Contents

Abstract **i**

Acknowledgements **iii**

1 Introduction **1**

1.1 Statement of originality 1

1.2 Goal of thesis 1

1.3 Publications 1

1.4 Structure 2

2 Background literature **4**

2.1 Historical overview 4

2.2 Measurement uncertainties 6

2.3 Electrocaloric effect 7

2.3.1 Cross–couplings 11

2.3.2 Theoretical approximations 15

2.3.3 Other caloric effects 18

2.4 Electrocaloric materials 21

2.5 Summary 24

3 Review of existing methods **26**

3.1 Temperature and entropy 26

3.2 Contact temperature methods 28

3.2.1 Thermocouples 30

3.2.2 Resistance thermometers 30

3.2.3 Electrocaloric examples 32

3.3 Calorimetric methods 32

3.3.1 Adiabatic calorimeter 34

3.3.2 Differential scanning calorimeter 37

3.3.3 General remarks on calorimeters 40

3.4 Non-contact methods 41

3.4.1 Non-contact methods – EC measurement examples 42

3.5 Other methods of measuring ECE 43

3.5.1 Fast response infrared photometry 43

3.5.2 Scanning thermal microscopy 43

3.5.3 Thermal wave method 44

3.6 Indirect method – indirect estimation 44

3.7 Comparison of methods 45

4 Metrology of the electrocaloric effect **48**

4.1 Ferroelectric tester 49

4.2 Electrocaloric facility set-up 51

4.3 Introduction to metrology, uncertainties 56

4.4 Calibration 58

4.4.1 Uncertainty of reference source 58

4.4.2 Calibration to ITS-90 58
4.4.3 Non–uniformity 62
4.4.4 Calibration – Summary 67
4.5 Uncertainty budget 67
4.5.1 Measurands 67
4.5.2 Uncertainty analysis 68
4.5.3 Sensitivity/Noise 69
4.5.4 Short term drift 71
4.5.5 Stability of the measurement artefact 71
4.5.6 Alignment (focus) 72
4.5.7 Size-of-source effect 75
4.5.8 Emissivity 76
4.5.9 Environment factors 79
4.5.10 Electric field 80
4.5.11 Conclusions 85

5 Characterisation of measurement setup 88

5.1 Non-uniformity and micro-scale size-of-source effect based on carbon nanotubes 88
5.1.1 The artefact 89
5.1.2 Setup 92
5.1.3 Results 92
5.2 Lowest temperature change based thin film resistor 95
5.2.1 Motivation 96
5.2.2 Artefact 96
5.2.3 Procedure and setup 97

5.2.4 Results and discussions 97

5.3 Assessment of temperature change in the setup 100

5.3.1 Motivation 101

5.3.2 Artefact 101

5.3.3 Setup and procedure 102

5.3.4 Results and discussions 103

5.4 Conclusions 107

5.4.1 Optical performance – the non-uniformity and size-of-source effect . 107

5.4.2 Lowest temperature change 108

5.4.3 Assessment of the setup 108

6 Inter-lab comparison **110**

6.1 Motivation 110

6.2 Calorimetric equipment 111

6.3 Polycrystalline BST ceramic 112

6.3.1 Dielectric properties 112

6.3.2 Polarisation Electric field loops 113

6.3.3 Leakage current 114

6.3.4 Heat capacity 115

6.3.5 Indirect estimation of ECEs 115

6.4 Measurement Procedures 116

6.4.1 Differential scanning calorimeters 116

6.4.2 Infrared thermography 118

6.5 Results and Discussion 118

6.5.1 Electrocaloric heat energy 118

6.5.2 Electrocaloric temperature change 119

6.6 Conclusions 123

7 Commercial samples: multilayer structures and mechanical coupling 125

7.1 Motivation 126

7.2 $BaTiO_3$ Multilayer ceramic capacitor 126

7.2.1 Specimen specification 127

7.2.2 Cross-section preparation 128

7.3 Results 128

7.3.1 Ferroelectric properties 128

7.3.2 Dynamics of the electrocaloric effect 129

7.3.3 Electrocaloric effect in MLCC cross-section 131

7.3.4 Electrocaloric effect as a function of temperature 133

7.4 Discussion 134

7.4.1 Dynamics of electrocaloric effect 135

7.4.2 Data extraction method 138

7.4.3 Optimal electrocaloric performance 140

7.4.4 'Temperature losses' in the measurement 141

7.4.5 Electrocaloric effect – cross-section 143

7.4.6 Direct and indirect electrocaloric effect 143

7.5 Conclusions 143

7.6 Motivation 145

7.7 Polycrystalline PMN-PT relaxor ceramic 145

7.8 Characterisation 146

7.8.1 Electrical and mechanical properties 146

7.8.2 Direct measurement 147
7.8.3 Indirect estimation 148
7.8.4 Secondary contributions to the electrocaloric effect 150
7.9 Discussion 153
7.10 Conclusions 156

8 Thesis conclusions **158**

8.1 Summary of thesis achievements 158
8.2 Inter-laboratory comparison 159
8.3 Investigations in commercial samples 160
8.4 Future developments 161

Bibliography **162**

A Calibration Facility at NPL **182**

A.1 Facility 182

B Uncertainty table for electrocaloric effect example **185**

C Characterisation of bulk resistor **186**

D Element analysis of X7R capacitor **189**

E Permissions **191**

List of Tables

2.1 List of coupled effects between electric mechanical thermal properties . . . 13

2.2 Orders of magnitudes in between coupled effects 14

2.3 List of selected electrocaloric materials. 25

3.1 Comparison of electrocaloric methods 47

4.1 Metrological definitions vocabulary 57

4.2 List of infrared camera calibrations 60

4.3 List of uncertainity contributions in temperature measurements of electroaloric sample 69

4.4 Uncertainty budget 86

5.1 Designed dimensions of the size-of-source artefact islands diameter d and the gap in between each CNT island. 90

7.1 Specifications of $BaTiO_3$ multilayer ceramic capacitor 127

A.1 Uncertainty budget for the H_2O cooled blackbody reference 183

B.1 Full uncertainty budget 185

D.1 Results of elements composition analysis on the X7R capacitor dielectric layer and connection terminal. 190

List of Figures

2.1 Heckmann cross-coupling diagram 8

2.2 Schematic diagram of multiferroic couplings with themal properties 19

2.3 Classification of dielectric materials in Venn type diagram. 21

3.1 Schematic representation of partial errors ΔT_{error} during contact temperature measurement 29

3.2 The basic schematic diagram of the temperature evaluation in a calorimeter. 33

3.3 Schematic diagram of an adiabatic calorimeter 35

3.4 Schematic diagram of a differential scanning calorimeter. 38

4.1 Ferroelectric tester facility 50

4.2 Photograph of the electrocaloric test rig at NPL. 52

4.3 Schematic diagram of an electrocaloric sample holder 54

4.4 Schematic of calibration setup 59

4.5 Calibration of infrared imager versus temperature standard 61

4.6 Calibration of infrared imager 61

4.7 Thermal uniformity at low temperature range 64

4.8 Thermal uniformity at high temperature range 65

4.9 Schematic of microscale infrared calibration issues. 66

4.10 Example of direct electrocaloric temperature change measurement results . 68

4.11 Sensitivity mneasurement of noise equivalent temperature difference of the infrared camera 70

4.12 Short therm drift 71

4.13 Schematic of defocus 73

4.14 Effect of focus on acquired temperature 74

4.15 Size-of-source effect for various areas 76

4.16 Emissivity error 78

4.17 Schematic diagram of the tilted surface with relation to the ideally parallel specimen 82

4.18 Applied voltage verification; the plot of relative voltage to set voltage for 1 kV range. 83

4.19 Applied voltage verification; the plot of relative voltage to set voltage for 10 kV range. 84

5.1 Configuration schematic of carbon nanotubes afteract for investigation of size-of-source effect 89

5.2 Scanning electron microscope images of the carbon nanotubes artefact . . . 90

5.3 Thermal uniformity based on carbon nanotubes 93

5.4 Characterisation of carbon nanotubes size-of-source effect 95

5.5 Schematic of resistive artefact for detection of minimum resolvable temperature change 97

5.6 Infrared thermograph of ressitive artefact for minimum resolvable temperature change 98

5.7 Effect of emissivity on a temperature change 99

5.8 Power and temperatures acquired with infrared and thermocouple 100

5.9 Setup diagram of a bulk resistor characterisation 102

5.10 Example of measurement procedure of bulk resistor 103

5.11 Characterisation of measurement setup based on temperature changes in resistive artefact 104

5.12 Temperature change of the resistor's as a function of temperature 106

6.1 Schematic diagram of a calvet differential scanning calorimeter adapted for electrocaloric measturement. Schematic not to scale. 112

6.2 Relative permittivity 113

6.3 Polarisation vs. electric field loops 113

6.4 Leakage current 114

6.5 Specific heat capacity at zero electric field 115

6.6 Indirect estimation as a function of electric field 116

6.7 Directly measured electrocaloric heat energy 119

6.8 Comparison of electrocaloric temperature changes measured at different laboratories 120

7.1 Scanning electron microscope image of cross section of the fractured $BaTiO_3$ multilayer ceramic capacitor 128

7.2 Polarisation vs. electric field loops 129

7.3 Diagram of electric field waveforms 129

7.4 Capacitor temperature difference ΔT_{IR} for short range of pulse lengths . . 130

7.5 Capacitor temperature difference for long various pulse lengths 132

7.6 Cross-section thermograph of multilayer ceramic capacitor 132

7.7 Electrocaloric temperature change measured at the cross-section of multilayer ceramic capacitor 133

7.8 Indirectly estimated electrocaloric performance of X7R capcaitor 134

7.9 Direct temperature change as a function of temperature measured ΔT at multilayer ceramic capacitor cross-section 135

7.10 Magnitude of electrocaloric effect as a function of electric field pulse length 138

7.11 Optimum performance of electrocaloric multilayer device 141

7.12 Schematic of multilayer capacitor structure 141

7.13 Rrelative permittivity 146

7.14 Measurement of P–E and D–E loops. 147

7.15 Direct measurement of electrocaloric effect 148

7.16 Indirectly estimated electrocaloric effect 148

7.17 Electric field criticality 150

7.18 Computed thermal expansion and piezoelectric coefficient 152

7.19 Mechanical contribution to electrocaloric effect 152

A.1 Uncertainity of blackbody reference as a function of temperautre 184

C.1 Temperature resistance coefficient for the resistor 187

C.2 Heat capacity of the resistor 187

C.3 Additional plots of temperature change characterisation inside of the chamber188

D.1 An example of the EDX results acquired on X7R capacitor. 189

Chapter 1

Introduction

1.1 Statement of originality

I confirm that except for those parts in which it is explicitly stated to the contrary, this project is my own work. It has not been submitted for any degree at this or any other academic or professional institution.

1.2 Goal of thesis

The goal of this thesis is to investigate direct electrocaloric effect (ECE) measurements, leading towards standardisation of ECE measurements, based on a non-contact spatially resolved infrared technique. Based on metrology, this work will aim to enable the development of tools citable for comparing various electrocaloric (EC) materials.

1.3 Publications

The following thesis resulted in three publications:

1. 'Experimentally validated finite element model of electrocaloric multilayer ceramic structures' published in *Journal of Applied Physics* [1].

2. 'Investigations of Secondary Contribution to Electrocaloric Effect in Relaxor PMN-PT Ceramic' published in *Ferroelectrics* [2].

3. 'Electrocaloric induced retarded ferroelectric switching' published in *Applied Physics Letters* [3].

1.4 Structure

Chapter 1: Introduction

Chapter 2: Literature review:

1. Introduces the concepts of the electrocaloric effect, how it is derived, other related effects, selection of material and introduction to uncertainties.

Chapter 3: Review of existing methods:

1. Focuses on the common methods used for measuring electrocaloric materials.

Chapter 4: Metrology of electrocaloric setup

1. Presents the set-up of a test rig developed and used throughout the experimental work in this thesis.
2. Considers calibration of infrared camera to temperature standards and addresses the uncertainty budget of electrocaloric temperature change.

Chapter 5: Characterisation of electrocaloric setup

1. Aims for deeper understanding of the measurement setup based on characterisation of reference materials, such as carbon nanotubes and resistors imitating an electrocaloric specimen.

Chapter 6: Application of metrology to electrocaloric materials

1. Employs an electrocaloric specimen for comparison of two different techniques across three labs.

Chapter 7: Investigation of electrocaloric effect in commercial samples

1. Assesses the transient behaviour in promising structures for future cooling application, the multilayer capacitor and examines challenges associated with addressing electrocaloric performance.
2. Researches the sources of additional error due to mechanical coupling not included in the definition of the electrocaloric effect.

Chapter 8: Thesis conclusions:

1. Concludes the work the major findings gathered throughout this work and finalised with further work recommendations.

Chapter 2

Background literature

2.1 Historical overview

The electrocaloric effect (ECE) has been drawn to the attention of researchers recently, due to possible solid-state cooling applications under the application of an electric field. According to Moya's work [4], the origins of electro thermal couplings, goes back over two millennia. The observation of debris attracted when tourmaline rocks were heated, was noted by the Greek philosopher Theophrastus. As a consequence this led to the discovery of the pyroelectric effect [4], one of the cross-coupled effects in certain materials, relating the thermal and electric properties.

The first formal evidence was discussed in 1878 by Sir W. Thompson [5]. In his theoretical paper, based mostly on experiments of his own and Mr. Joule on rubber, pointed out the possible thermal and entropy change in the presence of external fields (e.g. electric, magnetic, mechanical). Nevertheless, the hypothesis was that an electrical force, namely an adiabatically applied electric field, would produce a reversible temperature change within a solid material. This had been observed in a Rochelle salt ($KNaC_4H_4O_6 \cdot 4H_2O$) and demonstrated the electrocaloric effect in 1930 [6]. More than a decade later, in 1943 the ECE was quantitatively measured on Rochelle Salt [7]. Yet, the difficulties to perform the measurement on very small temperature change around 0.003 °C [8] limited

the number of investigations of the electrocaloric phenomenon.

Focus was renewed by research upon non-linear dielectric materials in 1950s, due to the discovery of perovskite structure $BaTiO_3$ ceramic [9], but also contributed to other compositions such as $KNbO_3$ [10], $LiNbO_3$ [11] and $PbTiO_3$ [12]. The investigation in new promising ferroelectric materials, because of their applications of the coupled properties, mostly the piezoelectricity and pyroelectricity, enabled research expansion also into electrocalorics. The ECE in ferroelectric material was first reported in 1962 for $BaTiO_3$ (BTO) and was around 0.4 °C [13]. Other studies of ferroelectric materials family resulted in discoveries of ECE exhibiting various magnitudes 0.3 °C in $SrTiO_3$ [14], 1.6 °C change in Sn-doped lead zirconate titanate $Pb(Zr_{0.455}Sn_{0.455}Ti_{0.09})O_3$ (PZT) [15] and finally 2.4 °C in multilayer $PbSc_{0.5}Ti_{0.5}O_3$ (PST) [16]. The one of the highest EC ΔT in ceramic bulk materials was quantified in the PST. This exhibited up to 1.6 °C [17] was implemented into a device by Sinyavskii, who later concluded that with the current low ΔT selection of materials the application of the ECE for cooling applications would be unlikely [18]. Furthermore, due to the temperature scaling with the thickness of EC material, the thick films and multilayer structures were investigated [19]. Thus from the first publication of ECE in Rochelle salt back in 1930 [6] to the Sinyavskii findings over 60 years of research accounted for around ≈ 90 publications in 2014 [20].

Interest was renewed in 2006 with the discovery of giant ECE in the vicinity of a phase transition in the doped PZT thin film, reporting an extraordinary EC $\Delta T = 12\,K$ [21]. This discovery restarted the EC investigations once more with a special target on development of new materials and structures, especially in the form of thick (including multilayer structures) and thin films. As a consequence the number of reports significantly increased from around 90 by 2006, to nearly 270 publications by June 2013 [20] and to 370 in March 2016 [22]. Some of the reported values ranged from around 10 K [21, 23, 24] to more than 50 K [25] in the EC temperature change. Unfortunately, there is no standardised technique to assess the ECE and no commercial EC measurement setup. Discrepancies in reported values were observed [26]. Hence the question of accuracy and uncertainties of quantified ECE arises. The errors, difficulties in measurement procedures

and differences between measurement techniques are the concerns of the so-called metrology, on which this thesis is focused.

This chapter aims to highlight the problems related to electrocaloric measurements. Firstly, the concept of measurement uncertainties is discussed, and the definition of what the ECE is and the formalism related to theoretical derivation. Later examples of electrocaloric materials are shown.

2.2 Measurement uncertainties

In metrology most measurements are indirect measurements; the quantified entity is estimated based on known relations via calibration to define the entity (e.g. to measure temperature with an IR detector based on the knowledge that the IR light emitted by the body is related to temperature on the surface, the incident IR radiation is converted into an electrical signal, amplified and converted into an estimate of body temperature). Metrology treats all measurable quantities with reference to a standard unit or a combination of one or more of the basic units e.g. in SI units measure of time is s, the heat capacity is JK^{-1} etc. Furthermore it treats the measured (estimated) quantity as an imperfect guess with certain boundaries to the real magnitude which is always referable back to the standard of this quantity. The probability boundaries that limit the confidence of the 'true value' location is called the uncertainty. These uncertainties of measured value are stated with their confidence bands, an interval of given probability of finding the true value within. These limits are described by coverage factor k. As an example, let us consider a measurement of a 1 m metal bar with a calibrated instrument resulting in (0.998 ± 0.001) m. The coverage factor was $k = 1$ of normal distribution. This means that the true value of length is expected to exist within the interval in a range between 0.997 m and 0.999 m with confidence of 68%[1].

The principle of the electrocaloric effect measurement is simple, however not trivial.

[1]For normal distribution the coverage factor k is equal to σ standard deviation; $\pm 1\sigma$ covers around 68%.

Namely the small temperature changes are a consequence of large electric field, which leads to non-linear properties [27]. Therefore, since the uncertainty is one of the important points on the 'road map' of this thesis, the literature review focuses around this theme.

2.3 Electrocaloric effect

The electrocaloric effect is defined as the ability of some polar (dielectric) materials to change temperature, when an electric field is applied or removed under adiabatic conditions. Electrocaloric materials contain disordered and randomly oriented electric dipoles, which align upon the application of an electric field. Consequently, the decreased material entropy which is manifested by an increase of its temperature, is the so-called electrocaloric exothermic change commonly exhibited as a peak. Conversely, in conventional EC materials, withdrawal of an electric field, increases material entropy and forces it to cool down, as an electrocaloric endothermic change [28]. There are 'reverse materials' which inversely to the conventional electrocalorics during application of ΔE will cool down e.g. PST [29].

One may find a more generic definition e.g. according to Glass and Lines: 'the ECE is a temperature change of a crystal which results from an adiabatic application of electric field' [27]. Such a definition states the cause of the effect, rather than point out the exact origin of the ECE, since this has not been yet fully understood [21, 19, 28, 22]. However, this statement simply is reduced to electrocaloric compliance defined by the pyroelectric coefficient p^E and Maxwell relation (for constant stress and strain), namely:

$$-\left(\frac{\partial T}{\partial E}\right)_S = \frac{T p^E}{c^E} \tag{2.1}$$

Where the c^E corresponds to the thermal capacity under constant electric field, which is often considered as heat capacity under short-circuit conditions.

Let us consider in terms of macroscopic theory the perfect elastically deformable dielectric

(in particular ferroelectric) body and assume that it is possible to describe all its properties, regardless of any atomic structure, by three independent mechanical, electrical and thermal variables out of the following pairs:

- temperature and entropy,
- stress and strain,
- electric field and polarisation.

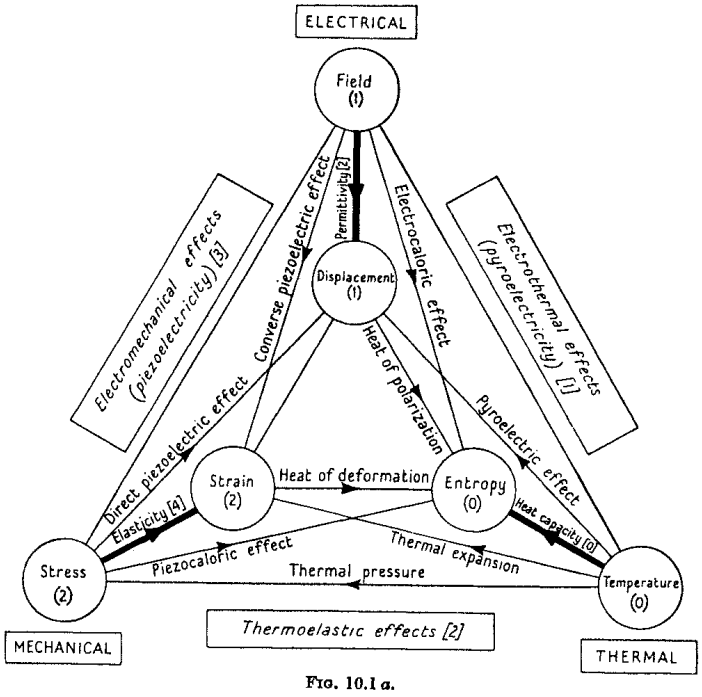

FIG. 10.1 a.

Figure 2.1: Schematic of the cross-coupling of the ferroelectric body, with respect to 6 independent variables; Heckmann diagram reproduced with permission based on Nye [30]. The tensor rank of the variables is shown in round brackets and the tensor rank of the properties in square brackets.

Founded on the above assumption certain cross-couple effects go back to Heckmann's considerations [31] and can be identified i.e. piezoelectric, piezocaloric effects etc. are allowed, as depicted conceptually in Figure 2.1 and will be discussed in greater detail in section 2.3.1 (p. 11).

Based on these interdependent variables the energy equation can be formed. According to the first and second laws of thermodynamics, a small change of an elastic dielectric solid

material's internal energy $\mathrm{d}U$ (per unit of volume) is described by a sum of infinitesimal quantities of heat Q received and work done W on to the body (the same volume):

$$\mathrm{d}U = \mathrm{d}Q + \mathrm{d}W \tag{2.2}$$

The work done on the volume of this body by electrical and mechanical forces (as a consequence of quasi-static transformation, with respect to their fields) and by assumption of the reversibility of thermal processes, the second law of thermodynamics ($\mathrm{d}Q = T\mathrm{d}S$) allows us to rewrite the equation 2.2 into:

$$\mathrm{d}\,U = T\,\mathrm{d}S + \sigma_{ij}\,\mathrm{d}u_{ij} + E_i\,\mathrm{d}D_i \tag{2.3}$$

where $\mathrm{d}u_{ij}$ is strain (the infinitesimal displacement of elementary volume $\mathrm{d}V$), $\mathrm{d}D_i$ is electrical displacement, $\mathrm{d}S$ is entropy, caused by the application of external stress σ_{ij}, electric field E_k and temperature T, respectively. The tensor notation (herein defined by Voigt notation; the subscript $_{ij}$, where $i, j = 1, 2, 3$) includes the anisotropy of mechanical and electrical properties of the solid.

Defining potential Gibbs free energy G as:

$$G = U - TS - \sigma_{ij}u_{ij} - E_iD_i \tag{2.4}$$

the differential of which, and according to equation 2.3, is:

$$\mathrm{d}G = -S\,\mathrm{d}T - u_{ij}\,\mathrm{d}\sigma_{ij} - D_i\,\mathrm{d}E_i \tag{2.5}$$

From here one obtains the following partial derivatives defining the principal material properties (the inner corners on Heckmann diagram; see Figure 2.1):

$$\left(\frac{\partial G}{\partial T}\right)_{\sigma,E}\mathrm{d}T = -S \tag{2.6}$$

$$\left(\frac{\partial G}{\partial \sigma_{ij}}\right)_{T,E} \mathrm{d}\sigma_{ij} = -u_{ij} \tag{2.7}$$

$$\left(\frac{\partial G}{\partial E_i}\right)_{\sigma,T} \mathrm{d}E_i = -D_i \tag{2.8}$$

Further derivation of the principal effects, results in the well-known Maxwell relations:

$$-\left(\frac{\partial^2 G}{\partial T \partial \sigma_{ij}}\right)_E = \left(\frac{\partial S}{\partial \sigma_{ij}}\right)_{E,T} = \left(\frac{\partial u_{ij}}{\partial T}\right)_{\sigma,E} = \alpha_{ij} \tag{2.9}$$

$$-\left(\frac{\partial^2 G}{\partial \sigma_{ij} \partial E_i}\right)_T = \left(\frac{\partial u_{ij}}{\partial E_i}\right)_{\sigma,T} = \left(\frac{\partial D_i}{\partial \sigma_{ij}}\right)_{E,T} = d_{ijk} \tag{2.10}$$

$$-\left(\frac{\partial^2 G}{\partial E_i \partial T}\right)_\sigma = \left(\frac{\partial D_i}{\partial T}\right)_{\sigma,E} = \left(\frac{\partial S}{\partial E_i}\right)_{\sigma,T} = p_i \tag{2.11}$$

where α_{ji}, d_{ijk} and p_i are thermal expansion, piezoelectric and pyroelectric coefficients, respectively. Equation 2.11 suggests that pyroelectric effect is thermodynamically equivalent to isothermal entropy variation (i.e. electrocaloric effect) and as a consequence one obtains the following relation:

$$dS = \left(\frac{\partial D_i}{\partial T}\right)_{\sigma,E} \mathrm{d}E_k \tag{2.12}$$

and its integral form:

$$\Delta S = \int_{E_1}^{E_2} \left(\frac{\partial D_i}{\partial T}\right)_{\sigma,E} \mathrm{d}E_i \tag{2.13}$$

where E_1 and E_2 are the initial and final applied electric fields, respectively.
Considering the heat capacity Cp of the electrocaloric material $Cp \equiv T\left(\frac{\partial S}{\partial T}\right)_E$, the electrocaloric temperature change $\mathrm{d}T$ can be written as:

$$\mathrm{d}T = -\frac{T}{Cp}\left(\frac{\partial D_i}{\partial T}\right)_{\sigma,E} \mathrm{d}E_i \tag{2.14}$$

and, assuming Cp is independent of E, the electrocaloric temperature change ΔT can be obtained as follows:

$$\Delta T = -\frac{T}{\rho Cp} \int_{E_1}^{E_2} \left(\frac{\partial D_i}{\partial T}\right)_{\sigma,E} \mathrm{d}E_i \tag{2.15}$$

where ρ is the EC material density.

The above definition yields the theoretical derivation of the electrocaloric effect firstly as solely based on the pyroelectric coefficient, suggesting a reversibility of the effect during heating and cooling. Moreover, it suggests the exchangeability of pyroelectric with electrocaloric coefficients (discussed further in Section 2.3.1). This brings us to another controversy: namely, the adiabatic temperature change is measured at a constant external stress and an electric field, but in order to be measured, the electric field must be changed. This is correct from the thermodynamic perspective since the EC thermodynamic equations of the equilibrium state consider the effect and its definition as a steady-state phenomenon. Nonetheless, the transient electrocaloric heat has been measured for different slew rates (speeds of electric field application), which resulted in the tuning of the ECE magnitude [32]. In this study most of the difference in EC δT can be accounted by a relatively longer thermal time constant, time of heat propagation through material, than a time of rising electric field to the maximum level. This implies lack of adiabatic conditions during measurements, hence dissipation of the heat to surrounding, but does not exclude the possibility of additional unquantifiable uncertainties from misusing the steady state equations in the measurement process of ECE which is a transient phenomenon. The steady state equations are correct only with respect to certain assumptions and estimations which are carefully discussed in section 2.3.2.
The eq. 2.15 is the most common and widely used description of electrocaloric effect, especially after 2006 [21] when the giant effect was estimated in a PZT thin film.

2.3.1 Cross–couplings

Having defined the electrocaloric effect, the general macroscopic thermodynamic model and its thermodynamical equivalence to pyroelectric effect and their implications will now be discussed in a domain of cross coupled effects (and their consequence based on the established model). To begin with, the model of 3 pairs of 6 independent variables was proposed by Heckmann in 1925 [31]. This robust graphical classification of cross coupled properties was developed around 2 decades before the knowledge of ferroelectricity, where

most of these effects are enhanced.

Therefore the proposed explanations were developed for linear materials. This was expanded by Nye in his book [30], on which most of the description below will be based.

Let us start from the three principal effects defining the outer and inner apexes of the triangles. As depicted in Figure 2.1 the mechanical, electrical and thermal properties can be described by the three main principal effects (linear effects):

- elasticity (change of strain), as a small change of stress $d\sigma_{kl}$ resulting in a change of strain: $\epsilon_{ij} = s_{ijkl}\, d\sigma_{kl}$[2], s_{ijkl} – elastic compliance;
- permittivity (electric displacement), as a small change of electric field dE_j producing electrical displacement: $dD_i = \kappa_{ij} dE_j$, κ_{ij} – permittivity tensor;
- heat capacity (change of entropy), as a reversible process considering unit volume, when entropy: $dS = (\frac{C}{T})dT$, T – absolute temperature, C – heat capacity per unit volume.

With the aid of a Heckmann diagram one may simply read out possible connections between the properties. These further show the existence of couplings in various combinations of electromechanical, thermoelastic and electrothermal. The number of 9 cross-coupled effects can be caused by the following independent variables ('forces'): σ_{ij} – stress, E_i – electric field and T – temperature. Each of these can be fully represented by 3 crystal properties (as a results of the external 'forces'; inner corners of the diagram), which are ϵ_{ij} – stress, D_i – electric displacement and S – entropy. Their differential forms are:

$$d\epsilon_{ij} = \left(\frac{\partial \epsilon_{ij}}{\partial \sigma_{kl}}\right)_{E,T} d\sigma_{kl} + \left(\frac{\partial \epsilon_{ij}}{\partial E_k}\right)_{\sigma,T} dE_k + \left(\frac{\partial \epsilon_{ij}}{\partial T}\right)_{\sigma,E} dT \tag{2.16}$$

$$dD_i = \left(\frac{\partial D_i}{\partial \sigma_{jk}}\right)_{E,T} d\sigma_{jk} + \left(\frac{\partial D_i}{\partial E_j}\right)_{\sigma,T} dE_j + \left(\frac{\partial D_i}{\partial T}\right)_{\sigma,E} dT \tag{2.17}$$

[2]Subscript "$_{k,l}$" is used due to the full fourth-rank tensor notation.

$$dS = \left(\frac{\partial S}{\partial \sigma_{ij}}\right)_{E,T} d\sigma_{ij} + \left(\frac{\partial S}{\partial E_i}\right)_{\sigma,T} dE_i + \left(\frac{\partial S}{\partial T}\right)_{\sigma,E} dT \tag{2.18}$$

In order to simplify, the equations 2.16, 2.17 and 2.18 for clarity, are named and represented with the corresponding constrains in Table 2.1.

Table 2.1: Possible coupled effect in a crystal according to the equations 2.16, 2.17 and 2.18.

		σ (stress)		E (electric field)		T (temperature)
ϵ (strain)	=	elasticity	+	converse piezoelectric	+	thermal expansion
D (electric displacement)	=	direct piezoelectricity	+	permittivity	+	pyroelectricity
S (entropy)	=	piezocaloric effect	+	electrocaloric effect	+	heat capacity

This leads to the estimated magnitudes of the coupled effect and necessity to state the measurement conditions under which these inter-related properties are investigated. The matter of appropriate conditions is discussed later, but the full relations between coefficients measured under different conditions with respect to all principal effects can be found in Nye [30]. Typical magnitudes for non-metallic and non-ferroelectric crystals are presented in Table 2.2. Hence, these coefficients suggest that some of the magnitudes will be negligible, so the cross-coupling will be non-existent or at least negligible. These values are estimated without consideration of any spread in their components of each tensors, nor in relation to the temperature. Most of the properties measured at different conditions have only a small contribution of around 1% or even less 0.1% i.e. the piezoelectric contribution to the measured permittivity at isothermal conditions or the thermoelastic contribution to the measurement of heat capacity between clamped and free Cp at constant E-field, respectively. Hence, when quantifying any property of the highly coupled materials such as ferroelectric, the coupled effects should be determined, in order to establish the true total value of such property.

For example in the case of the pyroelectric effect the relative difference between properties measured in crystals vary in around the order of magnitude. Thus in the pyroelectric

Table 2.2: Estimated magnitudes of coupled effects for crystals (non-metallic and non-ferroelectric) at room temperature [30].

	σ	E	T
ϵ	10^{-11}	3×10^{-12}	10^{-5}
D	3×10^{-12}	10^{-10}	3×10^{-6}
S	10^{-5}	3×10^{-6}	10^{4}

literature [33] we find it described in terms of primary, the change pyroelectric current at constant strain and secondary effects, result of the piezoelectric contribution originated from thermal expansion. Simply, a pyroelectric crystal which is free to change its shape will produce an extra contribution to dielectric displacement via thermal strain. This additional path can be followed on the Heckmann diagram as T$\rightarrow\epsilon\rightarrow$D, which according to polar crystal properties and theoretical considerations [34] is a directional effect. Depending on the material, if the primary or secondary origin of the pyroelectric effect is positive or negative, large or small, they are summed to evaluate the total value of the effect. For instance in $BaTiO_3$ a total pyroelectric coefficient is -200 $\mu C\, m^{-2}\, K^{-1}$, whereas the primary and secondary coefficients are +60 and -260 $\mu C\, m^{-2}\, K^{-1}$, respectively [34]. Typically, the secondary contribution is found to be less in comparison to the primary, especially for ferroelectrics [33]. The pyroelectric coefficient is frequency dependent [35] and strongly temperature dependent due to the substantial ionic rearrangement of crystal structure during the phase transition. The pyroelectric effect vanishes above the curie temperature when a material changes its symmetry to a nonpolar point group (becomes centrosymmetric) [34].

The secondary contribution in the electrocaloric community has been rather neglected. This has been estimated to be around 26% in the ferroelectric polymer , the P(VDF–TrFE)[3] 55/45 mol% copolymer [36] and is investigated in this work (see Section 7.5 also in Ref. [2]).

[3]Which stands for poly (vinyledene fluoride–trifluoroethylene).

2.3.2 Theoretical approximations

In order to recognise the potential sources in uncertainties (see Section 2.2), an analysis into the estimations, assumptions and measurement conditions for the theoretical derivation has to be accomplished. Unfortunately in the EC literature, one cannot find detailed and clear approximations on the final effect, nor any uncertainty consideration within both indirect estimation or direct measurements. It has been performed in the pyroelectric materials and the effect of the boundary conditions and secondary contributions for valid representation of pyroelectric compliance P_i has been understood [33]. All of these factors with short descriptions are listed below:

1. Process is adiabatic:

   According to the thermodynamic laws, this assumes that the energy is transferred only as work, therefore no other losses such as heat loss through electrical contacts, mechanical loss etc. are present.

   The adiabatic conditions are theoretical by definition and are non-existent in a real scenario, and can be only assumed once the thermal constant is much slower than the speed of measurement, or when body is isolated from the exterior environment. This however, is not always the case and affects results obtained via measurements [37].

2. The material under test is linear:

   The body's intrinsic properties are interrelated linearly; each of the coupled effects between the temperature, stress and dielectric displacement are linear.

   For most ferroelectric materials this assumption is right once the applied E-fields are very low. In contrast, to achieve the highest ECE, considerable E-field are required, and can go from 3 $MV\,m^{-1}$ for bulk materials up to more than 100 $MV\,m^{-1}$ for thin films. The ferroelectric materials are non-linear by default and strongly dependent on a transient changes of temperature, stress or electric field [38].

3. The material under test is homogeneous and isotropic:

   The body is built from as ideal single phase crystal structure. Secondly that the

properties are the same irrespective of the direction of measurement.

Due to the complex atomic structures, polar crystals exhibiting EC properties are known for their relatively high anisotropy similar to other materials from this family e.g. piezoelectric PZT or a piezoelectric relaxor PMN-PT[4], or a pyroelectric SBNO[5].

4. The heat capacity is electric field independent:

   This assumption is not valid and may lead to errors in estimation of measured ΔT_{EC}. That aspect of the field dependency was used to measure an entropy change as a function of temperature at given fields $\Delta S(T)_E$ and estimate an ECE in BTO [39]. More on this topic is covered in Ref [22, and references therein].

5. The volume is constant:

   The thermodynamic equations of state consider a constant volume, whereas small volume changes of around 1% can be estimated. The simultaneous existence of anisotropic thermal expansion and piezoelectric effect, due to application of electric field and changes of body temperature are present and would correspond to secondary contributions.

6. The stress is constant:

   In principle there is no external stress applied during EC cycle, however, under the application of high electric field the electromechanical effects are present. The internal stress arising from simultaneous piezoelectric displacement is present.

7. Higher order couplings are negligible:

   The possible couplings under the external forces are depicted in Figure 2.1 and indicate 9 different configurations.

8. The ECE is a static property:

   The temperature change is assumed to be independent of the frequency (slew rate): so the time does not affect the magnitude of ECE.

   Bai et al. [32] studied BTO multilayer capacitors with respect to dynamics of the

[4]Which stands for $Pb(Mg_{1/3}Nb_{2/3})O_3 - PbTiO_3$.
[5]Which stands for $Sr_{0.5}Ba_{0.5}Nb_2O_6$.

ECE (in a region close to thermal time constant) where the ramp rate directly affected the measured magnitude. Other properties such as dielectric permittivity or pyroelectric are known for their strong dependency on the frequency, which in electrocalorics are generally not included.

9. Thermodynamic quantities of physical properties are the same once under electric field:

   It has been shown that the physical properties of solids change under electric field and they vary from the thermodynamic variables; ferroelectric materials do not fully obey the Maxwell equations [38]. According to Munn the real physical properties in compare to the thermodynamic versus are not rotationally invariant, hence no equal. Both will coincide only at the case of constant strain and rotation, which is not present under application of electric field to a body.

These assumptions are reasonable in the thermodynamic representation, as theoretical estimation of simplified effects. It is believed that once these assumptions are made the contributions/errors are negligible. Nonetheless, it is most likely that ferroelectric materials are not constrained by all of the assumptions [27, 38]. Nye points out the complexity of the interactions in such materials [30], e.g. secondary mechanical contribution which was confirmed in $P(VDF - TrFE)$ $55/45 mol\,\%$ polymer [36]. In general, the equations of state hold true in static conditions.

All of the above agree with the findings of Liu et. al work [22], where some of their assumptions leading to several misunderstandings were clarified. For instance, the unexploited kinetics of ECE (treated as static phenomenon), the constant and independent heat capacity and the polarisation measured as a function of electric field, which depends on the cycling frequency, are some of them. Moreover, in estimation of ECE where the polarisation electric field are acquired at around kHz frequency, can cause neither adiabatic nor isothermal conditions [22]. Hence, the indirect estimation can be overestimated by 40% [40]. Further research has shown that once the measurement conditions are set to the sufficiently low level of frequency ensuring the isothermal conditions, the validity of indirect estimation can be achieved even for relaxor material [41].

Not only the complexity of the couplings depicted in Heckmann's diagram, based on their simultaneous existence, but their dynamics should be considered too. One important note on the Heckmann work is that in his original manuscript he discussed the coupling triangle with respect to internal and external origin of variables in the system rather than only a thermodynamic isolated model.

2.3.3 Other caloric effects

Contrary to the thermoelectric materials, where the temperature gradient is caused by the continuous flow of electrical current, the caloric materials' temperature change is manifested once the external force is applied or removed. These effects are named according to the origin of their driving fields and are characterised via adiabatic temperature change, isothermal entropy change or isothermal heat [4]. As depicted in Figure 2.2, caloric effects can be determined when applying various 'forces' leading to interlinked properties. The thermal properties of a body, as in EC materials are coupled to the electrical properties, are also permitted with the mechanical (stress σ and strain ϵ) and magnetic (magnetic field H and magnetization M) properties are named as mechanocaloric and magnetocaloric effects, respectively. A body possessing more than one of cross-coupled properties is called multiferroic[6].

Mechanically coupled – mechanocaloric

Lord Kelvin first defined cross-coupling when experimenting with Joule on the 'mysterious' temperature changes during elastic deformation of rubber [5].
In these materials, once a mechanical force is applied the reversible thermal changes can be observed. Depending on the form of applied stress to the body two types of effect are distinguished:

1. Barocaloric, when an isotropic stress is applied, via hydrostatic pressure change.

[6]Defines materials simultaneously exhibiting more than one primary coupling.

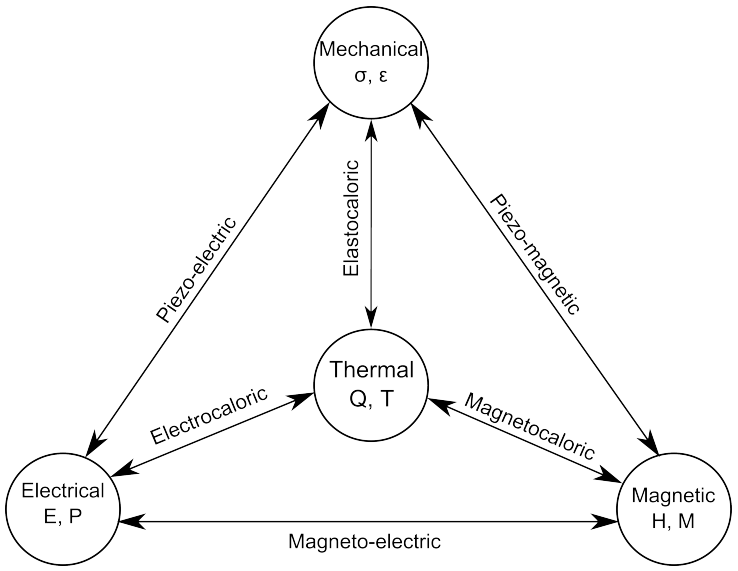

Figure 2.2: Schematic diagram of multiferroic coupling in solids with the connecting thermal relations. Reproduced from [42].

2. Elastocaloric, once the body is exposed to a uniaxial stress[7].

These effects are present in ferroic [43, 44] and non-ferroic materials e.g. shape memory-alloys [45, 46]. Similar to EC materials, giant effects have been reported in the literature [4, 45, 46]. The significant limiting factors (mostly losses) have been found such as a frictional heating for elastocalorics [47]. And for the barocalorics the effect might be underestimated due to the elastic heat leaks [43].

From an electrocaloric perspective, even though this has not been measured yet [4], this can bring mechanical tunability[8], especially for ferroelectric materials and enhance their performance [48]. The strain affects the polarisation and the ferroelectric transition, hence the enhancement of ECE can be obtained [49]. The mechanical clamping has been investigated in chapter 2 of Ref. [20, and references within]. One may find an excellent and more extended review on this topic in Ref. [4] and its continuation in Ref. [50].

[7]Note that quite often in textbooks the 'piezocaloric effect' is used.

[8]Ability to tune the desired property e.g. electrocaloric, by application of external 'force' i.e. creating a mechanical strain in to a system.

Magnetic coupled – magnetocaloric

The magnetocaloric effect (MCE) is an analogous phenomenon to the electrocaloric effect, however the entropy change is manifested under application of magnetic field. The similarities have been pointed out in some electrocaloric research [51, 52, 53]. Nearly a decade ahead of electrocalorics is the discovery of giant magnitudes in magnetocalorics [54]. Some EC work points to a magnetic 'equivalent' as an example of more advanced MCE one, especially when it comes to regeneration techniques and implementation into device [53]. Additionally, the comparison of energy conversion between these effects has been shown [52].

Prefix 'ferro' in ferromagnets and ferroelectrics is misleading due to lack of the iron in the electric counterpart. This is rather used in relation to analogy between spontaneous magnetisation and electric spontaneous polarisation. Despite the similarities and analogies between electric or magnetic fields thermally coupled caloric effects, there are major differences too. From the crystallography perspective the crystal properties interrelated with magnetic materials are based on axial symmetry (axial tensors), whereas the electric counterpart is based on polar symmetry (polar tensors) in its nature [34]. In other words, ferromagnets operates due to asymmetry in electronic spin, whereas ferroelectrics because of polar ordering, asymmetry in charges either ionic or electric or both [55]. These are reflected in the weak strain coupling for magnetic materials and strong strain coupling in electrical materials [27]. The atomic scale length is greater in ferroelectrics than in ferromagnetics, the ratio between electro/magneto dipoles interaction is significant ~ 19000 [55]. Also further differences are: existence of free charges reducing local fields, strong coupling between the polarization andthe lattice, inhomogenities, local fields and others, which can be also associated with electrocalorics. More on this topic is covered in Rebes book "Modern physics of ferroelectrics" [55].

2.4 Electrocaloric materials

By definition, all EC materials will belong to the family of dielectrics, due to their nature of electrical polarisability. The non-centrosymmetric crystals, which possess a unique axis of symmetry are polar materials. A special case where the polar state can be switched on or reversed between two or more orientational states with electric field are called ferroelectric [27]. This is depicted among other classes of the dielectric crystals, categorised with respect to their properties, in the Venn-type diagram in Figure 2.3.

As electrocaloric materials belong to the set of dielectric materials, all will possess ECE of rather small magnitude. Historically treating the phenomenon was predicted in the XIX century [5], and much later first was found in the Rochelle Salt crystals [6] and more then 30 years later precisely measured $\Delta T_{EC} = 4\ mK$ [8]. This breakthrough was due to initial discovery of ferroelectricity in the Rochelle salt, in which the effect was expected to be significantly larger. Due to its small magnitude, the effect was investigated in a subset of a ferroelectrics [56], which naturally possess non-linear properties originating from the hysteresis behaviour. The electrical, mechanical and thermal hysteresis are omnipresent in these materials, as well as the strong frequency dependence for the subclass of relaxors.

Naturally, the focus of the researchers was towards these 'new' non-linear materials,

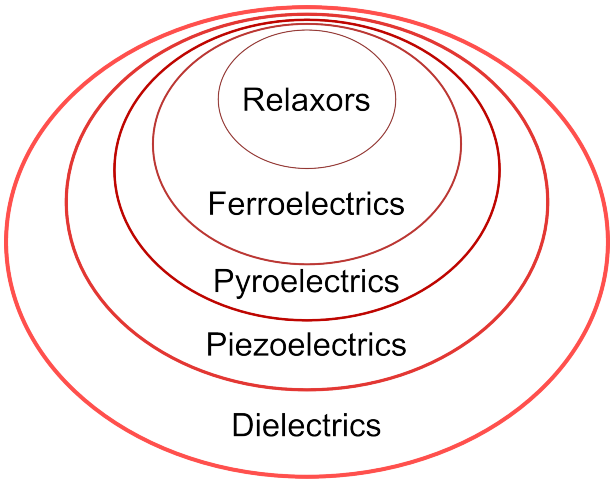

Figure 2.3: Classification of dielectric materials in Venn type diagram.

where the electro-thermal coupling was far stronger and with more pronounced magnitudes easier to be measured. Scientists come up with different ways to enhance the effect by a

means of doping [57, 58], engineering misfit strain [59, 60] or designing structure ie. grain size [9, 61] etc.

Most of the current EC materials are based on the Perovskite structure (ABO_3). The blend of two coexisting phase ferroelectric materials, especially in the vicinity of the morphotropic phase boundary, are known to achieve larger EC couplings [62] and sometimes more diffused (relaxed) EC response over a wider temperature transitions. This led to interesting mixtures with higher dielectric and piezoelectric coefficients, such as PZT ($Pb(Zr,Ti)O_3$), BCZT ($(Ba,Ca)(Zr,Ti)O_3$), PMN-PT ($Pb(Mn,Nb)O_3{-}PbTiO_3$), NBT-BT ($(Na,Bi)TiO_3{-}BaTiO_3$) etc. These ceramic materials are the most commonly investigated, yet there are other 'non-conventional' materials possessing significant and very large magnitude of ECE e.g. liquid crystals [63] or ferroelectric polymers [64].

There are various ways to classify ferroelectric materials for instance as Subburao [65] by the chemical composition into nearly 30 groups e.g. perovskite type, manganites, tungsten bronze type oxides, molybdates etc. Alternatively, in Ozbolt's work [28] EC materials has been classified into three categories namely monocrystals, ceramics (includes the bulk, thick and thin films) and separately polymers (thick and thin films).

The selected materials of various compositions and forms are shown in Table 2.3. There are several review articles discussing the various electrocaloric materials specifically [28, 19, 66] and other reviewing ECE including EC materials [4, 22, 50, 53].

Here only two ceramic materials are discussed, see below;

BTO

$BaTiO_3$ is one of the most important dielectric and widely used ferroelectric oxide materials. Simultaneously developed in United States, Germany and Russia in the 1940s, was used to prove that the ferroelectricity is not only associated with the hydrogen bonding [9]. Because of the high dielectric constant and lead free composition is at the same time the most studied ferroelectric material [9]. Also due to its commercial availability, BTO samples are quite often investigated for ECE [1, 32, 67, 68, 69].

Numerous studies of polycrystalline bulk [13] and thick film [70] BTO have been conducted.

Also, single crystals have been investigated due to the sharp first-order phase transition [71, 48, 72]. Various dopants and blends of BTO-based materials have been studied $(Ca, Na, Sr)TiO_3$ resulting in various ΔT_{EC} and T_c for each composition see Chapter 6 in Ref. [20] e.g. $Ba(Zr_xTi_{1-x})O_3$ (BZT) [73], $Ba(Ti_{1-x}Sr_x)O_3$ (BTS), $Ba(Sr_xTi_{1-x})O_3$[58, 74], or $Na_{0.5}Ba_{0.5}TiO_3 - BaTiO_3$ (NBT-BT) [75]. These are classified as alternative lead-free EC materials.

Relaxor PMN-PT

The inorganic ferroelectric relaxor $Pb(Mg_{1/3}Nb_{2/3})O_3 - PbTiO_3$ is well known for its good piezoelectric properties [76] and high pyroelectric effect [77] (thermodynamically equivalent to ECE), which made it initially interesting for studying the electrocaloric effect.

(1-x)PMN-xPT[9] is a complex ceramic solid solution of two well-known polar materials, the ferroelectric relaxor $Pb(Mg_{1/3}Nb_{2/3})O_3$ (PMN) ceramic [78] and the ordinary ferroelectric $PbTiO_3$ (PT). The phase diagram has been studied from $x = 0$ (pure PMN) to $x = 70\%$ [77, 79, 80]. In the vicinity of morphotropic phase transition the expected structures of non-ferroelectric cubic crystals (above T_C) and a rhombohedral structure below $x < 0.34$ and tetragonal above 0.34, have been confirmed. However, the additional study of complex structures via high resolution X-ray diffraction [81] confirmed the existence of a pseudo-cubic structure (which included three monoclinic phases [82]) and corresponded to a polarisation rotation allowing large piezoelectric responses [76].

To clarify, relaxors are the subclass of ferroelectric materials, which possess unique properties such as: a strong characteristic frequency dispersion of dielectric permittivity [83], broadly diffused phase transitions [84], the critical nature observed on electric field-composition-temperature diagram [85], dual peak of electrocaloric temperature change [86], electric field induced reversible relaxor-ferroelectric phase transition [87] and many others [20]. A theory of polar nano-regions (PNRs) has been proposed to understand these abnormal behaviours.

[9] General formulate is where x shows percentile of each of phases; for short rather the PMN-xPT is used.

This has been shown by Randall et al. [88], and later verified by extensive study with X-ray and neutron diffuse-scattering [89, and citations within]. There are two distinct approaches suggesting either fixed disordered distributions causing the random electric field, or similar to polar glasses, glass-like behaviour, with randomly interacting nano-domains due to random fields [20]. The special model of spherical random-bond-random-field [90] has been proposed to explain polar nano-regions interacting between themselves and between local electric fields leading to a clearer perspective on relaxor materials. However, numerous anomalies are not understood fully, due to similarity in average and local structural characteristics [83].

The electromechanical properties of PMN-PT have been used commercially in actuators and for sensing applications (e.g. sonars). The strong electrothermal coupling makes it a potential candidate for future prototypes [91]. Hence, the scientific interest [16, 92, 93, 94]. Same examples are presented in the list of EC materials, see Table 2.3. For more details, a comprehensive review of ECE in PMN-PT [20] and for other relaxor materials can be found in Ref. [16, 76, 78, 83, 92, 95].

2.5 Summary

The electrocaloric effect has been reported in the literature for the various forms (thermal masses), namely bulk, thick films, thick multilayer structures and especially thin films, due to their reported higher temperature changes. Measurement with different methods or estimated values have been reported in literature. Some discrepancies have been noticed depending on the research groups, forms of materials measurement technique etc. (see Table 2.3). Strictly speaking, from a metrology perspective, the unquantified uncertainty places doubts on reported values. Thus the necessity of reporting the measurement techniques has been recognised as an important factor in presenting the results, particularly for the estimated values in thin films.

Table 2.3: List of selected electrocaloric materials.

Material	Form	T_{peak} $[K]$	ΔT $[K]$	ΔE $[MVm^{-1}]$	Measurement technique	Ref.
$Ba_{0.65}Sr_{0.35}Ti_{0.997}Mn_{0.003}O_3$	ThF/B	293	-3.08	13.0	IE	[58]
BST	ThF	/	-15	50	$\star$	[96]
Copolymer P(VDF-TrFE 55/45)	ThF	340	-12	120	AdC	[97]
$BaTi_{0.895}Sn_{0.105}O_3$	B	301	-0.61	2.0	IE	[98]
$BaTiO_3$	SC	402	-0.9	1.2	DT	[71]
$BaTiO_3$	SC	412	-1.6	1.0	DSC	[39]
$BaTiO_3$	SC	397	-0.87	4.0	DSC	[71]
$BaTiO_3$	B	391	-0.40	0.8	DT	[13]
$BaTiO_3$	MLC	352	-4.0	35.2	DSC	[32]
NBT	B	413	-0.34	5.0	DSC	[75]
BNT-0.3BT	B	423	-2.10	5.0	IE	[99]
Irradiated P(VDF-TrFE 68/32)	ThF	306	-20	160	$*$	[24]
$(NH_2CH_2COOH)_3 \cdot H_2SeO_4$	SC	295	-0.18	0.2	AdC	[100]
$(NH_2CH_2COOH)_3 \cdot H_2SO_4$	SC	323	-0.11	0.2	AdC	[101]
$PbSc_{0.5}Ta_{0.5}O_3$	B	291	-1.80		IE	[102]
PLZT 8/65/35	B	385	-2.20	8.8	AdC	[93]
PMN	B	451	-2.60	9.0	AdC	[93]
PMN[111]	SC	274	-0.11	1.0	AdC	[93]
PMN-0.3PT	B	429	-2.70	9.0	AdC	[93]
PMN-PT 90/10	B MLC	323	-0.55	2.9	AdC	[16]
PMN-PT 90/10	B	296	-1.25	1.5	DT	[92]
Rochelle salt $(NaKC_4H_4O_6 \cdot 4H_2O)$)	SC	295	-0.0036	0.14	AdC	[6]

Where the abbreviations are: SC – single crystal; PC – polycrystalline; MLC – multilayer ceramic capacitor and for measurements techniques: DT – direct temperature; ID – indirect estimation; DSC – differential scanning calorimeter AdC – adiabatic calorimeter and IR – infrared camera. Also $\star$ – atomistic simulation and $*$ – specially designed infrared photometric setup.

Chapter 3

Review of existing methods

Development in electrocaloric effect science has been focused more on achieving greater magnitude, rather than 'how to measure the Electrocaloric effect'. Therefore, the indirect estimation outnumbered the direct measurements of electrocaloric effect (ECE) [20, 22]. As a consequence, many efforts have recently been made to develop direct measurement methods for electrocaloric heat Q_{EC} (ΔS, often named as entropy change) or temperature change (ΔT or ΔT_{EC}). These thermodynamic concepts are introduced shortly to give the reader an understanding of the fundamental principles of derived temperature and its scalability which is contrary to other fundamental units in the international system of units (SI unit scale).

3.1 Temperature and entropy

Before considering the measurement of the 'energetic states' of EC materials two interrelated measurands are considered, namely temperature and heat, which are interrelated by the term of an entropy change.

Temperature, as a concept, is a scalable measure, a quality, of how 'cold' or 'hot' is a body of interest – the system. Temperature is a property of any material, thus independent

of size (volume or density), describing the thermodynamic energetic state of the system. It is an expression of how much microscopic particles (i.e. molecules, ions, atoms) are vibrating inside the system. An average of these kinetic energies can be calculated with the Boltzmann constant k_B, $E_{avg} = \frac{1}{2}k_BT$. Thermodynamically speaking, temperature can be related to some fundamental physical or chemical state and can describe its energy level, as an absolute thermodynamic temperature independent of any other arbitrary material properties. Thus any change of a body state from point A to point B, for instance by adding heat, can be well defined in the thermal equilibrium conditions and easily related to its temperature. However, the thermodynamics deal with an ideal state A and B, regardless of their structure, supporting the assumption that this equilibrium model is based on homogeneity of the systems. Otherwise the local thermodynamic states can be considered as regions of varying local properties; temperature distribution in the system. To achieve the thermodynamic temperature measurement is a very difficult and time-consuming process. Therefore metrologists introduced the standardised defined scale, of which the most modern version is the International Temperature Scale of 1990 (ITS-90) [103]. Thus temperature is measured as a reference to the predefined scale of fixed points, which refers to thermodynamic values used to calibrate the e.g. standard platinum resistance thermometers for the range of interests and to keep traceability to the standard. These points are typically melting or freezing points of metals e.g. tin, zinc; boiling points e.g. hydrogen, helium; triple points e.g of water, mercury (so the solid, liquid and vapour states are at equilibrium; more precisely the melting or freezing points at the vapour pressure) [104].

Entropy (denoted as S) is theoretical substance-like body, so can be created, spatially distributed, transferred etc. within matter and outside of it. The absolute value of entropy can be derived in statistical mechanics from the distribution of microscopic configurations Ω representing a thermodynamic system as $S = k_B\, ln\Omega$. Thus entropy is regarded as the disorder of the microscopic structure of the system. Entropy is an extensive property with SI unit JK^{-1}. It changes with the size (volume) of a body, and can be normalised to the volume (e.g. m^3) or quantity of the matter (e.g. mol, g). According to the 2nd

law of thermodynamics, which joins the entropy change and absolute temperature T_{Abs} with a rate of reversible heat Q_R (see Eq. 3.1). Each system flows to more favourable lower energy states (heat flows from hot to cold; high disorder matter is 'slowed down' by lower disordered one). For practical reasons, the entropy change term ΔS is used. Because of heat exchange with the environment, the entropy change can be measured in a calorimeter with good accuracy, as a heat change in the system. This treats a body placed in idealised conditions (e.g. isothermal; thus thermal equilibrium) in relation to its environment; so the system can be quantified with respect to the controlled surrounding.

$$\Delta S = \int \frac{\delta Q_R}{T_{Abs}} \tag{3.1}$$

3.2 Contact temperature methods

The measurement of a solid body temperature problem can be solved by both non-contact and contact methods. Evaluation of a body temperature based on surface probing with a liquid or gas surrounding is the most common difficulty in contact methods. One may encounter the three fundamental temperature errors, which arise from such an approach, and are referred to as partial errors [105]. These are shown in Figure 3.1 where on left-hand site is a body at original state and on the right-hand site is the body disturbed during the measurement of the temperature at the surface. The red lines represents the temperature, y axis, with respect of the length on x axis. For the simplicity let us assume a thermal steady-state case, where source of the heat is inside of the body with a finite temperature T_{true} which is higher than temperature of air T_{air} (or any gaseous media). Also that the convection and conduction are the main heat transfer mechanisms. Note that the T_{true} is not important for the following discussion, however, it is higher than temperature of the surface T_{surf}.

The first partial error $\Delta T_{error\,1}$ is a consequence of the original temperature field deformation. Once the surface is in contact with temperature sensor e.g. thermocouple, TC, the investigated surface is under the influence of a more intense heat flow at an

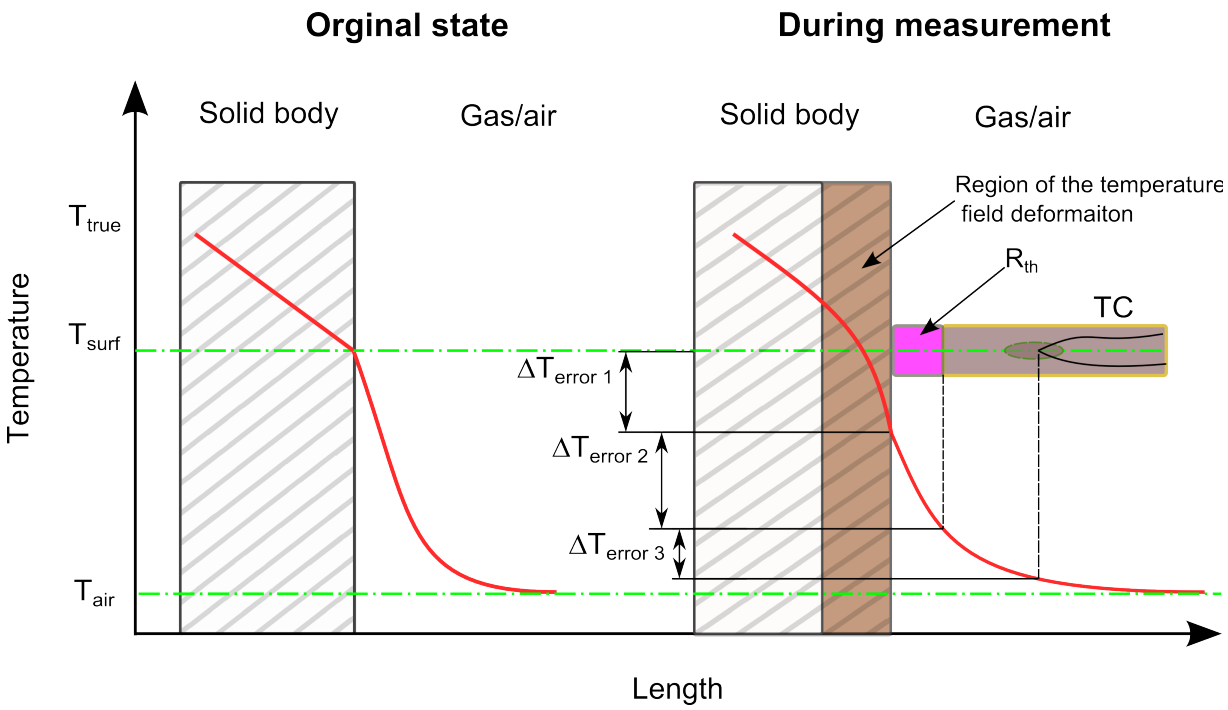

Figure 3.1: Representation of partial errors ΔT_{error} concept during contact temperature measurement shown on an example of a semi-finite solid body without temperature sensor (left-hand site) and with a temperature sensor (right-hand site), here a thermocouple TC. Red line shows the temperature progression along the length from true temperature T_{true} inside of a body, to a surface temperature T_{surf}, to the temperature of gaseous media (air) T_{air} and the temperature progression with temperature offset due to the partial errors, when a TC is introduced. Schematic not to scale.

adjoining area in compare to surface at original state. Thus the drop in the original surface temperature T_{surf} is encountered by the value of $\Delta T_{error\,1}$ at the region of the deformed temperature field.

The second partial error $\Delta T_{error\,2}$ is caused by a thermal contact resistance R_{th} of the sensor with a surface area of the body. A non-ideal contact will cause the drop of temperature across this point by the corresponding value of $\Delta T_{error\,2}$. This error depends on the multiple factors i.e. force of contact, cleanses and smoothness of measured surface etc.

Finally the third partial error $\Delta T_{error\,3}$ is a drop on the temperature solely based on the distance of the sensing point from the surface of the specimen. This is mostly affected by the design of the sensor e.g. isolated thermocouple, where the sensing point is only few millimetres away from the tip of shielded probe.

3.2.1 Thermocouples

A thermocouple (TC) is a passive temperature sensor that produces voltage once exposed to temperature gradient via the Seebeck effect. More precisely this effect is described by the voltage generation along an electrical conductor resulting in the difference of temperatures across the considered length. The 'thermo-couple' is built out of at least two different conductors bonded together forming a differential potential at their join. An electromotive force expressed in volts, typically is measured directly from the TC. To improve the accuracy of absolute values, before connecting the TC to the measurement instrument, a reference cold junction at 0 °C (water with ice) is used. The typical sensitivity of TC is around 40 μV per 1 °C and it varies for type and the operating range.

There are various types of thermocouples and they are standardised e.g. in Ref. [106, 107] and the most common ones are J, T and K types.

The advantage of this solution is small, inexpensive and self-powered sensors, can be easily used and are interchangeable due to their standardised design. The limiting factor of the TC might be the accuracy which mostly is limited down to less than a degree Celsius, depending on the temperature scale [104].

3.2.2 Resistance thermometers

Resistance thermometers measure the temperature changes on a sensor made of wires, chip etc., by means of directly measured electrical resistance change. There are many types of resistive temperature detectors (RTDs) and their type, shape, operating range will vary by application. It is worth noting that the RTDs are active sensors, therefore a small current needs to be applied in order to acquire the resistance values. Typically most of the sensors are made with two connections only and to improve the performance temperature sensitivity different connection configurations are possible e.g. for high precision 4 terminal method. Furthermore, the 2 distinct categories of RTDs can be recognised, depends on the material they are made of, namely platinum resistive thermometers

and thermistors.

Platinum resistance thermometers

The temperature scale standard, the ITS-90, defines the temperature in a range of $14 - 1230\ K$ by the Standard Platinum Resistance Thermometers (SPRTs). These are the most accurate sensors with uncertainty down to ± 0.001 °C or less, however are only suitable to use in research laboratories under controlled conditions, where the best accuracy is required. The industrial equivalent are so-called IPRTs, also the Pt100s/Pt1000s, alternatively all named as RTDs. The industrial PRTs are made of films or wires based on the alumina substrates (or inside alumina tubes).
Pt100 is a standardised platinum sensor commercially used, which has the resistance of 100 Ω at 0 °C (analogically 1 $k\Omega$ for Pt1000) and it is rigorously defined by the international specification IEC (BS EN) 60751:2008. The sensitivity of Pt100 sensors is approximately 0.4 $mV\ °C^{-1}$ for the standard conditions. This sensor achieves the uncertainty of ± 0.01°C for the range of −100 °C to +250 °C (and tenths of °C for ~ 600 °C).

Thermistors

Thermistors are semiconductor based temperature detectors. In RTDs the resistance changes linearly with the temperature. However thermistors are not standardised sensors, thus the specification must be confirmed with the manufacturer's datasheets rather than any universal standard. Typically sensors are made from small beads of various semiconductor (most commonly with the negative temperature coefficient: resistance decreases with temperature) material possessing resistances of several $k\Omega$ allowing 2-wire sensing without significant errors. The disadvantages of these sensors are the non-linear response, limited operational span to few hundreds °C, sensitivity to decalibration/damage due to the overheating and the small thermal mass making them susceptible to self-heating errors.

3.2.3 Electrocaloric examples

Contact thermometry is a straight forward method to measure any temperature variations in science and engineering. Such practice seems to be more practical and reasonable in most of the cases, such as bulk and multilayer structures, rather than the indirect estimation [22], which carries a threat of unquantifiable uncertainties. Nonetheless, only relatively few reports can be found, where such are present in the literature [108, 109, 68, 71, 14]. Thermocouples were used to assist the infrared measurements and aid in estimation of emissivity [67, 110]. Moreover in some examples the indirect and direct temperature reading have been adequately predicted [71, 15]. Such a method usually is non-adiabatic, thus a significant heat exchange to environment should be avoided. For this reason a fast voltage ramping is suggested in order to reduce the heat leaks [19]. A poor contact between specimen and sensor will cause lag in the thermal time response, which is reflected in flattened responses of measured values under application/withdrawal of electric fields [68].

The way of eliminating the surrounding effects is achieved by controlling and this partially can be accomplished by dual TC setup, by placing a specimen in a silicon oil bath, then measuring temperature of both oil and sample [92]. Similarly by employing on additional heater to specimen [26]. The aforementioned setup presented by Lu et al. [26] is already classified as a calorimetric method, in which the environment is precisely controlled.

3.3 Calorimetric methods

Calorimetry refers to the measurement of what is broadly understood as a heat or a heat flow rate. Calorimetry was continuously developed for more than 200 years along with the development of thermodynamics describing the nature of matter (and its states e.g. vapours, solids, and liquids) as a result of a heat exchange.

There are numerous variations of these heat measurement devices, varying from classical calorimeters in chemical reactions instruments e.g. drop calorimeter, bomb calorimeter,

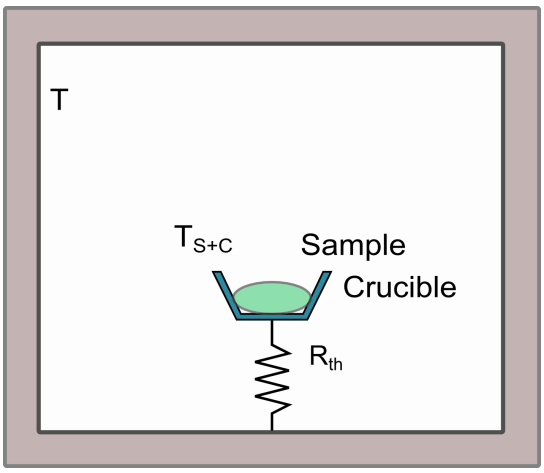

Figure 3.2: The basic schematic diagram of the temperature evaluation in a calorimeter.

etc. to other more modern devices, which were implemented for electrocaloric measurements, such as an adiabatic or more practical dynamic (scanning) differential calorimeters.

The basic representation (see Figure 3.2) of any calorimeter can be simplified to the setup containing the system, composed of a sample and its container (crucible), and the thermostatic surrounding T in which is placed. The system T_{S+C} and the thermostat, with reasonably stable and uniform temperature T, are connected together via contact resistance R_{th}. The heat flow is measured via known thermal resistance R_{th}. Depending on the R_{th} there are two types of calorimeters. The diathermal, where the thermal resistance is the lowest, or the adiabatic type, where no heat is exchanged hence the R_{th} is the highest [111].

In practice calorimeters can be classified in various ways arising from the fact that one instrument can operate in various modes resulting in different properties and uncertainties. Nevertheless, in general calorimeters can be classified by three criteria namely, principle of operation (heat-compensation or heat-accumulation), mode of operation (static: isothermal, adiabatic, etc.; or dynamic: scanning of surrounding, adiabatic scanning, etc.) and construction (as a single or twin/differential measuring system).

The most commonly used setups such as adiabatic calorimeter and differential scanning calorimeters are discussed. Examples for each method adapted for electrocaloric measurement are described and the details, such as design, operation principle and source of uncertainty are presented.

3.3.1 Adiabatic calorimeter

An adiabatic calorimeter is an instrument employed to examine the heat change in controlled lossless environment. Various nomenclatures e.g. ideal, close to ideal, semi-adiabatic, isoperibol calorimeter, depending on the precise aspect of classification have been suggested [111]. Here the 'adiabatic calorimeter' is used.
Since this method can significantly vary, the main principle of operation will be mentioned and the rest will be discussed with respect to examples used in the electrocaloric community.

Adiabatic calorimeter – operation principle

The adiabatic calorimeter can be set up so that the exchanged heat is either by reducing the temperature difference or by elevating the level of the thermal resistance, between the system under test and the thermostatic surrounding (i.e. oil bath).
The temperature difference between the system under test and thermostatic surrounding is adjusted to the zero level by a precision controller. Hence the setup is operating in an 'active' mode by measuring the power required to compensate the heat changes inside the specimen/holder system. These are measured via set of thermocouples or PRT's on or close to the specimen.
The second route of operation relies on the adequate thermal insulation and heat measurement of the system. Due to the lack of an idealised thermal insulation in nature, such quasi-adiabatic systems are subjected to correction defined by a calibration of residual heat leaks. A specimen is equipped with a temperature/heat sensor measuring controlled release of heat to the thermostat (here treated a heat sink; so specimen thermal mass $<< Cp_s * m_s$).

Adiabatic calorimeter – design and EC examples

In the current EC literature, only two groups developed their own variation of a specially adopted adiabatic calorimeters.
One is at the Jožef Stefan Institute, Slovinia. A high-resolution calorimeter was specially

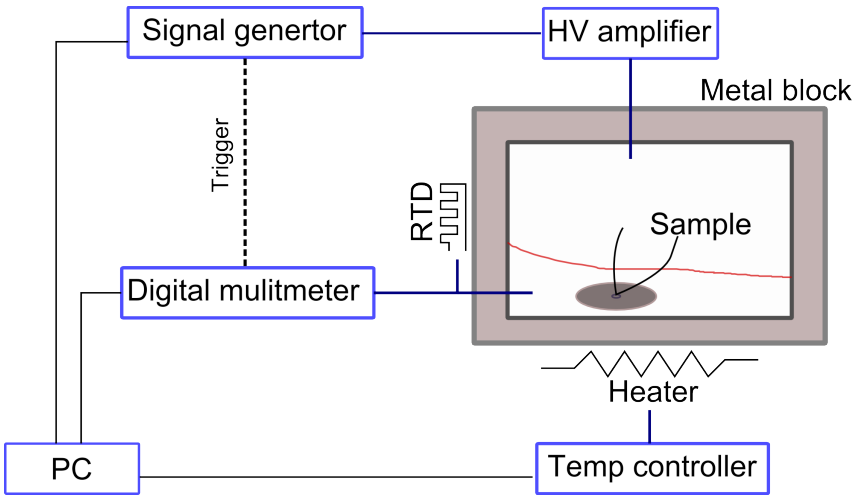

Figure 3.3: Simplified schematic of the EC adiabatic calorimeter. Adapted from [20].

designed (including electrical HV feedthroughs) and built for electrocaloric materials [112]. This setup was used by Kutnjak and his group to initially study the latent heat of the relaxors phase transition with respect to electric field [85]. It was possible due to the instrument's ability to operate in an ac mode[1] (sinusoidally heated) and relaxation mode (step or linear ramped power[2]) [113]. Various examples of directly measured ECE have been reported for bulk or thick film ceramics [93, 114]. Also, a successful study of a thin polymer film has been achieved [26]. The setup schematic depicted in Figure 3.3 consists of a classical adiabatic calorimeter enclosed in an outer guarded thermal shielding copper can (not depicted in the diagram), with a centrally placed bath block made of copper (in Figure 3.3 referred as metal block[3]) [111]. Hence, the system provides a very precisely controlled thermal bath stability within 0.1 mK. Uniform heating of the bath block is achieved by a flexible heater wrapped around the bath and stabilised based on temperature readings from an integrated thermistor. Additionally, the platinum resistance thermometer (PRT) is immersed in the bath to obtain temperature readings of the bath.

The measurement setup accommodates specially prepared samples with a small beaded thermistor directly attached to the surface, either by heat or electrically conductive paste. The various shapes e.g. circular or rectangular for different thickness's, are permitted [20,

[1] The ac mode provides the superior resolution and precision of $Cp \approx 0.01 - 0.1$ %.

[2] Allows to quantitatively measure a small latent heats as precise as 0.1 mJ, useful in studies of supercritical regions of phase transitions.

[3] For better performance quite often silver is used instead of.

and Ref. therein].

The power measured by this setup, is delivered by the sample due to the electrocaloric effect. The necessary driving voltage is delivered by a high voltage amplifier[4] connected to an arbitrary waveform generator. The system is triggered with a digital multimeter in order to acquire the adiabatic EC temperature change via computer.

Another unique adiabatic calorimeter was developed at Zhang's group at Penn State University [26]. In contrast to the setup at Jožef Stefan Institute, the specimen is integrated with a resistive heater and allows operation in the non-adiabatic mode [113]. The variation in this system is monitored by either a fast infrared sensor, or a heat flux sensor integrated between a specimen and substrate (see references

Adiabatic calorimeter – sources of uncertainties

The advantage of the adiabatic calorimeter is that the precise measurement of heat can be achieved in adiabatic conditions with thermal bath stability within 0.1 mK. For bulk and thick films, a relatively fast thermal response in order of milliseconds to seconds is achieved, because of the small thermal mass of the beaded thermistor [20]. The rigorous internal thermal model of the electrocaloric measurement in an adiabatic calorimeter was evaluated by Kuntjak and Rozic [117]. Due to the great precision, the simplified fitting method is applied with an error varying between $1 - 5$ %. However this systems relies on the zero-dimensional model [117] of the 'beaded thermistor' and relies solely on the 'known' values of the temperature of the bath and the heat capacities of the sample (with and without electrode) and thermistor. Unfortunately these known parameters contain uncertainties, which typically add up accordingly the law of uncertainty propagation and have to be assessed in a process for the setup individually [118], hence are unknown to the author. Additionally, the complexity of this technique arises from the necessity to prepare samples with a manually embedded thermistor [117, 20]. Thus it is recommended to evaluate the possibility of random errors due to such operation.

[4]This depends on the thickness of the specimen.

3.3.2 Differential scanning calorimeter

Modern differential scanning calorimeters (DSCs) are commercially available and currently the more common used to quantify the ECE, than adiabatic calorimeters. However such standard equipment is not designed to accommodate the investigation of ECE. They need to be modified to adopt the electrical feed-throughs and additional high voltage source [73].

Differential scanning calorimeter – operation principle

The standard DSC is based on 'a method of measurement in which the measurand is compared with a quantity of the same kind, of known value only slightly different from the value of the measurand, and in which the difference between the two values is measured' [119]. Hence a specimen and a reference with similar masses are thermally ramped in the controlled environment. A differential temperature value is recorded, as the thermoelectric voltage. The signal is proportional to a difference in heat necessary to maintain their temperature equal. Thus the heat capacity is obtained by the signal and a calibration factor of a DSC. Similarly to calorimeters, two ways of acquiring the power/heat flux are possible, either via difference in heating rates in comparison to a reference or the power compensated to maintain each cell at constant temperature.

Differential scanning calorimeter – design and EC examples

Two types of the DSCs namely, the heat flux DSC and power compensated DSC (power supply at constant rate) are used.

The double pan heat flux calorimeter is commonly used [19]. An example of such a setup is depicted at Figure 3.4. This type of calorimeter is composed of two symmetrical pans thermally connected to ensure a balanced heat flow. Crucibles are employed to insert a specimen and a reference (or empty crucible) and are placed on top of the pans. Depending on the operational range the equipment is designed to contain thermocouple

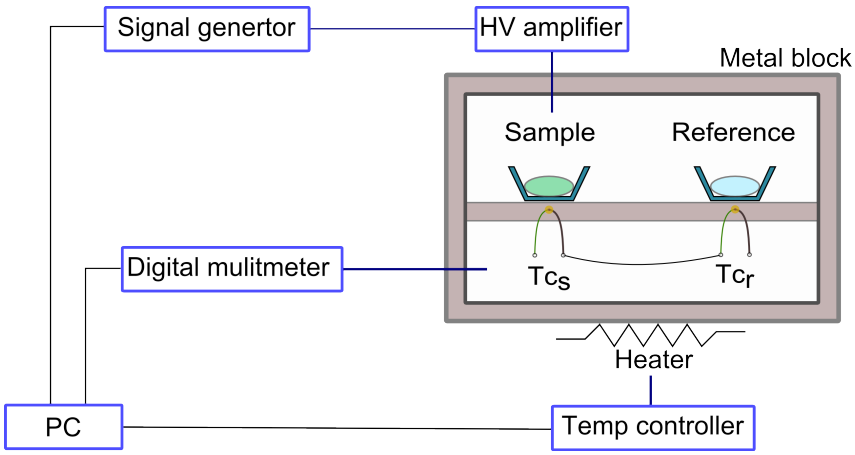

Figure 3.4: Schematic diagram of a differential scanning calorimeter.

metals offering the best performance. Thermocouples are attached to the bottom of each pan in series (or sometimes set-up of two thermopiles), thus providing the differential signal. The metal furnace for stability reasons is made either of silver or copper, and surrounded with thermal shielding, which is not presented on the schematic diagram. Most of the apparatus is commercially available, hence their popularity. Nonetheless, such apparatus has to be adapted to permit the feedthroughs for high voltage connection. Such a calorimeter usually combines the synchronised combination of a power amplifier (here denoted as HV amplifier), function generator and a PC for system automation. In same cases, a commercial DSC is used with a combination of a commercially available ferroelectric tester providing much broader analysis of EC specimens, e.g. P–E loops or leakage current measurements [98, 120].

Each system has its own calorimetric time constant, usually quite high to ensure the precision of the measurement. This will vary depending on the individual system, which is used to interpret the enthalpy curve. In order to extract the heat from the measurement, the heat flow rate over time measured by DSC has to be integrated and then multiplied by a given calorimetric constant. Typically the direct measurement of electrocaloric heat is a long process ($> 30\,min$) [39]. This is because of the time needed for sample to reach isothermal conditions, which are required for the stability and precision and are limited by a calorimeter thermal time constant.

The power compensation differential scanning, sometimes named heat flow DSC, is rarely employed to measure ECE. Mainly it is used for a heat capacity measurements and glass transitions of polymer materials e.g. PVDF [119]. In comparison to a classical heat flux DSC instead of employing the differential thermocouple in one chamber, it contains platinum resistive thermometers integrated in a controlled environment with two identical metallic chamber equipped with resistive heaters each. Hence the key difference is that it precisely measures the power difference in resistive heaters, required to increase temperature of a sample with respect to a reference. The advantage of this system is very low thermal time constant and ability to measure sharp, sensitive phase transitions.

Differential scanning calorimeter – sources of uncertainties

Any DSC is associated with the uncertainties such as temperature scale calibration, choice of appropriate reference or conditions. DSC measures difference in Cp with regard to a reference of choice (i.e. quartz standard or empty crucible). There are specific procedures in place which should be used to reduce uncertainty [121]. For optimal performance a sample/reference of similar shape, thermal mass or thermal properties is required to deliver high accuracy and low uncertainty. Furthermore, the slew rate of heating may affect the output result [119]. This methods relies on good thermal contact thus the sample shape and positioning inside the crucible is important, since it may significantly affect the observed results.

DSC setups are employed in the electrocaloric measurements as a heat meter placed in a controlled environment measuring changes under application of external electric field to EC specimen; the $\mathrm{d}Q/\mathrm{d}E$ is measured. Similar to direct surface temperature measurements, the DSC is not an adiabatic system. Hence it is suggested to use fast changes of electric field during EC measurement in order to reduce the losses [19]. Additionally, the time constant will depend mostly on the individual apparatus rather than specimen parameters such as mass or thermal properties.

Losses through the electrical contact need to be considered. Any heat leaks may contribute to reduce the acquired signal, which in consequence will lead to underestimation of the

ECE. The type and thickness of wires employed to deliver high voltage to EC sample may be chosen to reduce this contribution e.g. thin platinum wire, which has at least 3 times less thermal conductivity than copper. In order to avoid these dissipative errors the calibration procedures with a known or resistive sample have been already demonstrated [120, 73, 122].

3.3.3 General remarks on calorimeters

Calorimetric techniques are precise, however time consuming, due to their accurately controlled and shielded environments. High resolution calorimeters are capable to quantify the first-order phase transition at BTO ΔT_{EC} or the heat capacity anomaly at vicinity [72]. Whereas DSCs are commercially available solutions compromising a quality of achievable results resolution over a better measurement time and affordability.
For these techniques common errors and uncertainties will depend upon instrument, specimen and its preparation, measurement procedure, sampling rate, environment, rounding errors etc. Additional care is recommended since measurements are sensitive to measurement of a specimen mass, thermal losses, thermal contact between specimen and crucible and also to time dependent factors.
For the ECE, which is transient phenomenon, it is important to include time aspect in a measurement procedure. The uncontrolled measurement procedure neglecting the specimens thermal properties and thermal constant of a calorimeter can potentially lead to errors.

Considering the simple case where ΔT is calculated from calorimetric measurements, two values of Cp and Q_{EC}, both of them measured individually, are employed quite often without consideration of uncertainties. These propagate according to the law of uncertainty propagation [118], whereas the errors, if reported in literature do not seem to follow that rule. The case study of uncertainty propagation is investigated in Chapter 6. Secondly, when the T_{EC} is extracted from the calorimetric measurements, the heat capacity relation is used ($\Delta T = \frac{\Delta Q_{EC}}{Cp}$). Apart from the propagating uncertainty, instead the

heat capacity at 0 field $Cp_{E=0}$, is used and treated as field-independent. This has been experimentally shown to be not valid since the ECE was calculated from differences in heat capacity as a function of temperature $Cp(T)$ values measured at various E-fields [39]. The error of this assumption was predicted [22, 123].

3.4 Non-contact methods

Non-contact thermometry techniques refer to radiation thermometers such as infrared thermometers, radiation pyrometers, bolometers or even the more sophisticated thermal cameras. There are sensors which can measure a single spot on the object surface, e.g. pyrometers or multiple spots (array) e.g. thermal cameras. Infrared thermography allows us to acquire the temperature distribution of investigated surface.

Non-contact temperature measurements are based on the physical principle of the thermal emission. This can be considered as particles releasing energy due to their oscillations caused by the temperature. This correlation depends on the state of the matter, so the distinction between gases, liquid and solids has to be made. However, here only solid matter is under investigation, thus exclusively the surface thermal emission will be considered.

The mechanism of this phenomenon can be seen from two interrelated perspectives. Firstly as photon emission, where the photons are the zero mass particles with discrete quantities of energy. Secondly as an electromagnetic wave. These can be represented as the photonic emission energy W_e because of the oscillation of matter particles at the given wavelength λ ($\lambda = \frac{c}{f}$, f is frequency) by $W_e = \frac{hc}{\lambda}$. Where the h is the Planck constant and c is the speed of light.

The temperature emission exists at the infrared (IR) wavelength. These, for practical reasons, are typically split into three wavelength bands namely:

- near IR for 780 nm — 1.5 μm;
- mid IR for 1.5 μm — 20 μm;

- far IR for 20 μm — 1000 μm.

The emitted energy W_e from the surface depends on various aspects such as direction of the emission, the energy distribution for a spectrum of the wavelengths etc. This leads to the most important law governing thermal spectroscopy; Planck's law, which treats the emitted energy as a function of wavelength at the given temperature. It is expressed by the power irradiated by the ideal blackbody (b), the spectral radiance $L_{\lambda,b}$, per unit surface area and unit of solid angle:

$$L_{\lambda,b}(\lambda, T) = \frac{2hc_0^2}{\lambda^5[exp(hc/\lambda k_B T) - 1]} \qquad W\ m^2\ \mu m^{-1}\ sr^{-1} \tag{3.2}$$

where k_B is the Boltzmann constant, T absolute temperature of the blackbody. The law for short wavelengths reduces to Wien's law (this is used in Section 4.2).

3.4.1 Non-contact methods – EC measurement examples

The infrared camera has been employed for several electrocaloric materials e.g. polymers [110, 124] or multilayer structures [67]. The key features are spatial and time resolution implemented in a rather simple technique. For electrocalorics an initial comparison of infrared imager with other techniques have been made, e.g. with thermocouples [67] and as well as with DSC [110]. Moreover, because of its ability of non-contact measurements at a distance, infrared imagers are employed for other caloric effects [125, 126, 127]. This technique is useful not only due to its ability of fast sampling rate allowing measurements at close to adiabatic conditions, but also as one enabling a multi stimulus measurements for multi-caloric materials [22].

Recently, infrared imaging of heat flow in a multilayer structure has been performed, showing spatial capabilities on an electrocaloric specimen [69].

3.5 Other methods of measuring ECE

There are other techniques and these are briefly mentioned below.

3.5.1 Fast response infrared photometry

A unique setup has been developed, where thin cotton string-nets of low thermal conductivity were attached to a plastic sample holder [128], with an infrared sensor [24]. This method achieves a very fast response of a few milliseconds beneficial for detection of rapid ECE effects in thin films [20].

3.5.2 Scanning thermal microscopy

This technique employs a scanning probe microscope, and specially designed probes to measure a surface temperature at around micro-size/sub-micron level. Probes are nano-meter size sensors either, a resistive thermometer [67] or a bolometer [129]. The probe, which is usually not in contact with the sample, records the temperature changes under EC pulses with a resolution of 80 μm [67]. It appears that the transient results are strongly affected by the distance of the tip from the surface under measurement [41, 67]. This technique, due to its microlevel capabilities, has been applied in the measurement of thick films, both on a substrate [41] and in multilayered structures [67]. The adiabatic conditions can be met when the investigated volume is sufficient [22]. However, when the relaxor PMN-PT thick films were investigated, non-adaibatic conditions were present [41], due to the fast heat leaks to the substrate. These are caused by small and similar thermal masses of the substrate and active material.

3.5.3 Thermal wave method

A thermally modulated technique was introduced to determine the spatial distribution of polarisation in thin film polymers [130, 131]. This has been employed for evaluation of a frequency dependent pyroelectric current [132, 133, 134]. Due to the principle of operation the technique is named a laser intensity modulation method, for short LIMM, since the fast oscillating infrared laser (from $kHz - MHz$) introduces a complex thermal wave [135]. Due to the modulated intensity-frequency the desired periodic heat penetration depth can be achieved and can be directed to a desired location via a fast response galvanometer mirror scanner. Rapid surface scanning can be achieved. The current is measured via a sensitive current amplifier connected to a lock-in amplifier for noise reduction [135].
A relaxor PMN-PT 160 nmthin specimen has been measured [136]. The $\Delta T_{EC}\ \Delta E^{-1}$ coefficient has been estimated by integration of the pyroelectric current for various E-fields. To the author's knowledge this method has not been used elsewhere than group from Solid State Electronics Laboratory at Technische Universität Dresden [136, 137, 138]. This simple technique, despite the difficulty in extraction of depth penetration or polarisation values and complex mathematics [135], it is a quite promising approach for the measurement of ECE in thin films. It would require more development to achieve the quantitative, rather than qualitative data in EC measurement, i.e. Kleiner et al. used calibration described in Ref. [136, and references therein].

3.6 Indirect method – indirect estimation

This most common technique employs the equation 2.15 to derive the EC temperature change from the dielectric polarisation change with respect to temperature and electric field (section 2.3). The estimate describes the EC temperature change based on pyroelectric effect. It can be found in the literature [34] that these effects are inverse. Nevertheless, such seeming equality does not include the fundamental constraints, especially the measurement conditions which are different for each of the effects [30]. In contrast to the electrocalorics,

for pyroelectrics in case of measurement conditions are carefully addressed during measurements of pyroelectric coefficients to avoid errors [33].

Recent studies suggest the heat capacity variation applied under electric fields mentioned before, sensitivity of indirect estimations to quality of P–E loops (frequency dependence [139]) and that the numerical integrations/fittings or contributions of latent heat are not considered by the basic equation (equation 2.15) [140] etc. [22]. Hence the indirect EC estimation is prone to display an erroneous results with unquantified uncertainties. However, very recently it has been shown that once the measurement conditions are chosen carefully, high quality results can be obtained, even for in a relaxor material [41].

Nonetheless, to avoid confusion author's suggests instead of using the misleading term 'indirect measurement' to name it indirect estimation.

3.7 Comparison of methods

For indirect estimation method, three classes of temperature and two classes of heat measurements have been reviewed.

Even though the indirect method may be erroneous, seen in the volume of publications, the indirect values are those most frequently reported [22]. This is due to the inexpensive electrical tester/in-house built circuits, relatively fast time of electrical measurements and simple extraction method.

Contact thermometry methods are a simple and attractive alternative and supplementary to the indirect estimation. However, this method carries the systematic errors related to contact thermometry e.g. small mass of EC specimens in relation to the thermometer. Additional random errors are possible especially due to poor thermal contact, heat leaks or effects of environment.

Calorimeters are by simplification, extension of thermal contact methods, performed at controlled and stabilised environment. A stability of 0.1 mK is achievable, which allows precise measurement of various materials e.g. sharp first-order phase transitions. The price for the precision is a relatively long time required to achieve such performance.

Calorimeters are usually in-house built in order to meet the requirements. On the other hand, the differential scanning calorimeters obtain a similar performance for moderately low-cost commercial instruments. Additional invasive modifications are usually required, however, there are DSCs using double tube furnaces which easily accommodate additional changes. For the DSCs to meet their precision, the time-consuming baselines corrections for each sample are required.

Scanning thermal microscopy is a rather unexplored technique for electrocaloric applications. Fast response can be achieved by the micro-thermometer tips, which allows the measurement of thin films. It is a sensitive method and at the same time a quite difficult technique. Most of the atomic force microscopy based techniques, due to the tip sizes and complexity of physics interrelated with measurement process are qualitative rather than quantitative methods. The sensitivity of this technique is comparable with good infrared cameras.

Infrared imaging is a robust method allowing spatial and temporal investigation of surface temperature and its gradients. This technique is a powerful tool to investigate temperature change from a distance under application of any stimulus not only for electrocaloric. However, it is not widely used in the electrocaloric community. The main disadvantages are the sensitivity to the environment and the price of the sensitive instrumentation.

The summary of the comparison is shown in Table 3.1.

Table 3.1: Comparison of most common electrocaloric measurement methods.

Techniques	Type	Advantages	Disadvantages
Hysteretic $P-E$	Indirect	Well-known method Estimates electrocaloric effect in bulk and thin film materials	Assumes Cp independent of E-field Assumes specimen at equilibrium (e.g. Maxwell relations valid) Calculation errors e.g. due to data fitting
Contact thermometry	Direct	Relatively precise Price Off-shelf product	Limits in size Poor contact sample's surface leads to errors Bulky samples only Possibility of shorting (with HV) Need to be fitted for each sample
Adiabatic Calorimetry	Direct	In-house apparatus optimised to EC requirements Small samples allowed (including thin films) High sensitivity and precision	No off-the-shelf Time consuming Specimen requires special adaptation
Differential Scanning Calorimetry	Direct	Precise Small samples allowed Relatively high accuracy	No off-the-shelf EC DSC Modification may contributes to errors Lower accuracy due to small heat flows Difficult to measure thin films Time consuming
Scanning Thermal Microscopy	Direct	Low thermal mass of the tip to measure thin films Relatively Precise	Single point can measure at the time of each EC cycle Not suitable for simultaneous thermal mapping Surface effects influencing results e.g. attraction of tip due to humidity
Infrared Imaging	Direct	Relatively precise Spatially-resolved Robust technique No alteration of specimen required Non-invasive Measurement of bulk (possibly thin films)	Difficult measurement of reflective samples Uniformity of the surface required Emissivity effect on absolute temperature Measures surface temperature only

Chapter 4

Metrology of the electrocaloric effect

Electrocaloric Setup

In this thesis, two measurement methods have been used to evaluate the electrocaloric performance of materials, namely:

1. Indirect method: P–E hysteresis method, which measures electric field-induced (E) polarisation (P) response, which in turn can be used to calculate the electrocaloric effect in materials, using Maxwell's relations.

2. Direct Method: uses an infrared (IR) imager to measure electrocaloric temperature change, through the measurement of radiation coming from the sample while application/remova of an electric field.

4.1 Ferroelectric tester

Hardware

The polarisation and also mechanical displacement as a function of electric field, so called P–E or D–E loops, for the range of stabilised and discretised temperatures were acquired using an AixACCT TF Analyser 2000 Tester, as shown on Figure 4.1 (a). The test rig is made of several modules allowing a range of ferroelectric measurements. The current setup consists of the TF Analyser 2000 itself, SIOS laser controller unit, impedance analyser HP 4192 LF, temperature controller based on Eurotherm 2416 module, the two external amplifiers; Trek 610E $\pm 10\ kV$ high voltage and the Tegam Model 2350 $\pm 200\ V$.

(a) (b)

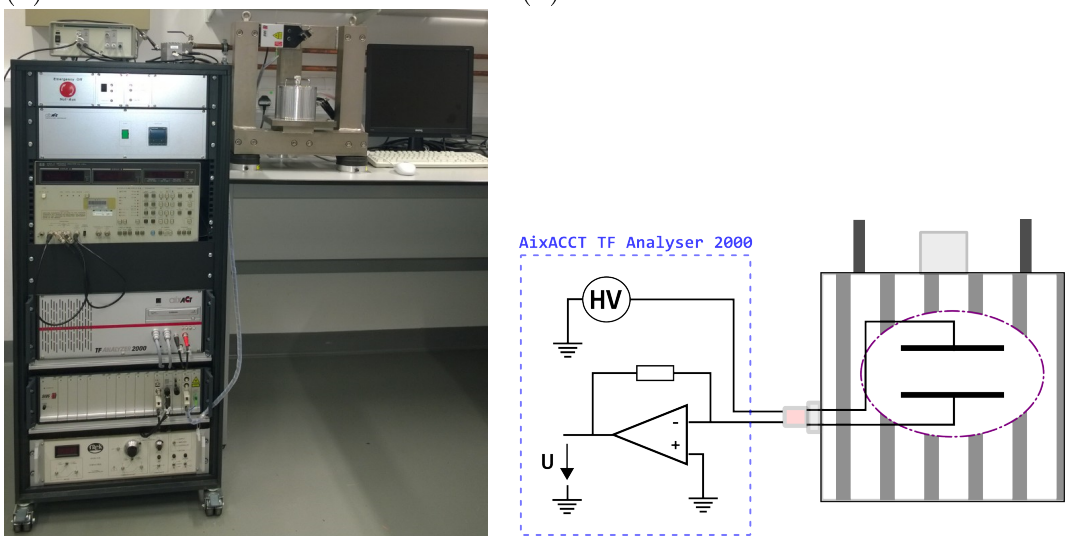

Figure 4.1: The ferroelectric tester Aixacct TF2000 analyser shown as (a) a photograph and (b) concept diagram (not to scale) including sample holder with capacitive sample inside, connected to AixACCT system (to virtual ground measurement circuit).

Aixacct's sample holder consists of a bottom fixed electrical contact and a top adjustable spring-loaded electrical probe enabling measurement of its displacement with SIOS SP-S 120 laser interferometer from the top. This sample holder permits measurements in a controlled temperature environment from room temperature (RT) up to 250 °C.
The ferroelectric analyser provides high precision current measurements especially for small capacitances based on the Virtual Ground principle, where high impedance operational amplifier fitted with a feedback resistor is used to reverse the current and the voltage, see diagram in Figure 4.1 (b).

Data processing

The electrocaloric effect can be indirectly obtained by measuring field-induced reversible polarization (P–E loops) and using Maxwell equation (see Section 2.3). Data on P–E loop for different temperatures are converted from AixACCT file format into matrices via a Matlab script. Once the implemented code is run, the shape-preserving piecewise cubic interpolation upon P and E data for individual environment temperature is run, and the equations 2.13 and 2.15 are subsequently solved. This method is rather straightforward and has provided accurate predictions of electrocaloric response for a number of materials.

But its universality and validity recently has been brought into question following reports revealing discrepancies in electrocaloric data measured directly and indirectly in relaxor materials [26]. In order to reduce and/or eliminate unquantifiable uncertainties of the indirect method, the direct measurement of electrocaloric temperature change must be used to assess electrocaloric performance.

4.2 Electrocaloric facility set-up

The system for the direct measurement of the electrocaloric effect based on infrared thermal imaging was developed and based at the National Physical Laboratory (see Figure 4.2). It comprises of a vacuum furnace allowing state-of-the-art electrocaloric effect measurements under air or vacuum environment down to $5 \times 10^{-7} mbar$, in the range of temperatures from 25 up to 250 °C ± 1°C.

The system is composed of an **active workbench** with a **chamber** with integrated **thermal stage** on the top of it, where a **sample holder** is utilised for specimen mounting and is measured with a **camera** attached to **positioning** stage embedded in vertical aluminium frame. These parts in bold are described below:

Camera

In the current facility an infrared (IR) camera Infratec ImageIR 8320 is used. This state-of-the-art instrument is based on a cooled InSb photon detector focal-plane array of size 640 $\times$ 512 pixels operating in the range of medium wavelength infrared spectrum, namely $2.0 - 5.7\ \mu m$. The sensor uses a dynamic range up to 16 bit analog-to-digital converters. To achieve superior thermal resolution $< 20\ mK$ a Stirling cooler is employed to maintain the sensor in an environment $< 80\ K$. High speeds of acquisition, more than 1 kHz frequency for the $^1/_4$ frame mode, resulting in time resolution $\approx 1\ ms$ (line mode allows $> 2\ kHz$) are achievable. The spatial performance is ensured via 3x infrared microscopic lens with a fixed focal length of nominally 21 mm and a 5 μm

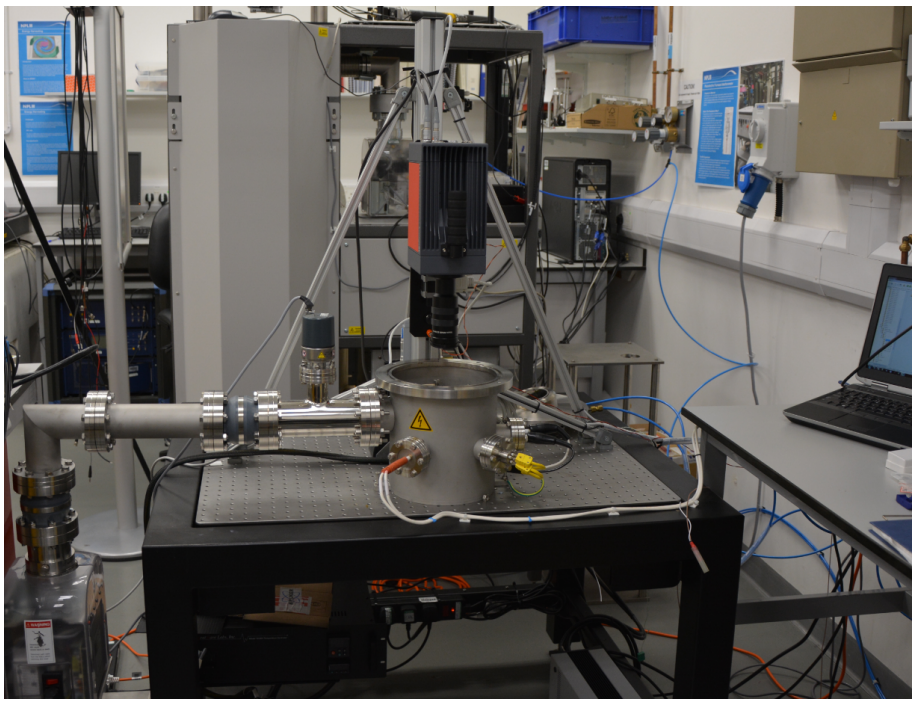

Figure 4.2: Photograph of the electrocaloric test rig at NPL.

spatial resolution per pixel. The camera was bought with the calibrations provided by manufacturer to cope with the temperature range from 20 °C to 250 °C.

Alignment

The instrument is installed vertically on the aluminium frame, with a one axis motorised precision translation stage, the PI M-403.22s. The position of the camera, apart from fine positioning of 0.2 μm step and precision of 0.16 μm over the length of 50 mm of motorised stage, can be adjusted manually in a coarse fashion of approximately 5 cm in a span of around 30 cm along the length of the vertical aluminium frame.

Chamber

Beneath the camera is located a test chamber, fitted with four standard inlets. The three of chamber inlets are the CF-35 flange fixed with ports, where one is 2×high voltage feedthroughs (up to 20 kV DC), the second port is 2×T-type thermocouple feedthroughs, and the third one is a port containing the high current electrical feedthroughs supplying

the embedded heater. Lastly the biggest vacuum inlet, the CF-63 is connected to a vacuum pump. Vacuum is produced by the Agilent mini-task AG-81 vacuum pump installed on an additional shelf, mounted to the table with special passive anti-vibrational rubber-metal feet. In order to reduce the excessive vibration of the pump, the whole assembly of the vacuum supply is fixed with two additional passive vibration decoupling bellows (flange standard CF-63) installed between pump and chamber with the 90° elbow.
The chamber's closing is built with specially designed 2 mm thick, water cooled tilted at 15° sapphire viewport. This vacuum window is embossed inside with respect to the lid surface, on the depth of around 20 mm, in order to: one, reduce the distance of the relative distance between camera and specimen (due to the short focal distance of 22 mm) and two, to reduce the reflections on the surface of the sapphire window[1]. Additionally, the embossed surface was coated with the high emissivity paint ($\varepsilon \approx 0.9$) to suppress external infrared radiation (e.g. ambient radiation or radiation of human body).

Active workbench

All the components described above are located on the top of an active anti-vibration stage (Accurion Vario 900 Workstation), providing the reduction of the low-frequency vibrations ($< 250\ Hz$), both the ambient and that arising from the IR camera operation. In the bottom of the anti-vibration stage are located two controllers, which do not require stabilisation: one is the controller steering the active vibration damping, and second is the HeatWave labs temperature controller with built-in power supply for the vacuum heater.

Temperature stage

The height adjustable (adjustment of $\approx 40\ mm$) furnace heater embedded inside the test chamber is a part of the HeatWave labs 101303-23C temperature controller-heater set. The top of a heating element is made of boron nitride and is embedded in a metal flat top made of Mo-Ni alloy. Two thermocouple controller + limiter action allows the

[1] Transmittance above 80 % has been found in a spectrum $1 - 5\ \mu m$.

temperature on the top of the heated plate to be set in a range of $25 - 250$ °C ± 1 °C. The settings of constant power, on/off or PID control are permitted.

Sample holder

Figure 4.3 shows the sample holder schematic. For the purpose of electrocaloric measurement, a sample holder was designed and manufactured out of high-temperature non-conductive polymer, PEEK[2]. It comprises the probes feedthroughs with screw adjustable fixing, allowing to accommodate samples from sub-millimetre to around 15 mm thick samples.

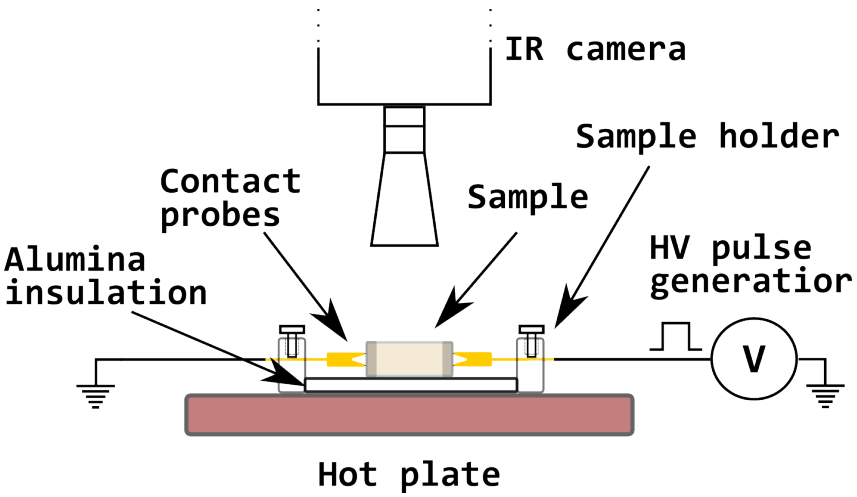

Figure 4.3: Schematic diagram of electrocaloric sample holder. Schematic not to scale.

Initially, serrated type, gold plated, spring loaded brass probes (RS components 542-4962) have been used, in order to reduce the thermal contact with a specimen. However, due to the thin coating of samples and damage to electrodes surfaces, was exchanged for rounded shape with a radius of 0.9 mm (RS components 261-5092). In both cases a factory contact resistance is specified around 50 $m\Omega$ and each of them provides a deflection based on embedded spring delivering a force of ≈ 1.5 N.

The sample is placed with a thermally conductive (electrically insulative) paste (RS components 217-3835) on the top of 1 mm thick alumina plate 25×25 mm in size. The plate contains a machined groove in which is placed K-type thin thermocouple, for controlling the temperature of the top-plate. This assembly is made with Aremco

[2]Stands for Polyether ether ketone; a semicrystalline polymer with high melting point around 340 °C.

Heat-Away 641-EV high temperature thermally conductive vacuum paste and covered with a Kapton tape. The whole plate assembly is attached to the hot plate with the same thermally conductive paste to ensure the good thermal contact.

Measurement uncertainty budget

The electrocaloric effect does not possess a clear and single definition, nor the strictly defined measurement technique, standardised method as presented in Chapter 2. Thus the identification of uncertainties in ECE measurements will depend on the preferred sample and measurement method. Here it is based on the infrared imaging and is described below.

4.3 Introduction to metrology, uncertainties

In metrology, the exact definitions (e.g. precision, error etc.) and tools (e.g. methods, protocols etc.) have been developed for successful assessment and description of the uncertainties. It is necessary here to clarify essential concepts in order to understand this chapter. These definitions have been adopted from the formal vocabulary of the International Bureau of Weights and Measures (BIPM), the 3rd edition JCGM 200:2012 [141], compatible with International Organization for Standardization (ISO) and IEC (International Electrotechnical Commission) standards ISO 80000 or IEC 80000 and are described subsequently in Table 4.1.

Table 4.1: Basic vocabulary of metrology definitions.

Name	Definition
Calibration	operation that, under specified conditions, in a first step, establishes a relation between the quantity values with measurement uncertainties provided by measurement standards and corresponding indications with associated measurement uncertainties and, in a second step, uses this information to establish a relation for obtaining a measurement result from an indication
Measurand	quantity intended to be measured
Measurement	process of experimentally obtaining one or more quantity values that can reasonably be attributed to a quantity
Measurement Accuracy	accuracy of measurement, accuracy; closeness of agreement between a measured quantity value and a true quantity value of a measurand
Measurement Error	error, error of measurement; a measured quantity value minus a reference quantity value
Measurement Precision	precision; closeness of agreement between indications or measured quantity values obtained by replicate measurements on the same or similar objects under specified conditions
Measurement Standard	etalon; realization of the definition of a given quantity, with stated quantity value and associated measurement uncertainty, used as a reference
Measurement Uncertainty	uncertainty of measurement, uncertainty; non-negative parameter characterizing the dispersion of the quantity values being attributed to a measurand, based on the information used
Random Measurement Error	random error of measurement, random error; component of measurement error that in replicate measurements varies in an unpredictable manner
Systematic Measurement Error	systematic error of measurement, systematic error; component of measurement error that in replicate measurements remains constant or varies in a predictable manner
Uncertainty type A	evaluation of a component of measurement uncertainty by a statistical analysis of measured quantity values obtained under defined measurement conditions
Uncertainty type B	valuation of a component of measurement uncertainty determined by means other than a Type A evaluation of measurement uncertainty e.g. via certified reference material, obtained from a calibration certificate etc.

4.4 Calibration

4.4.1 Uncertainties of reference black body cavities and artefacts

Calibrations of the infrared (IR) imager (according to the International Temperature Scale of 1990 (ITS-90)) namely the drift, the sensitivity size-of-source effect (SSE) were quantified against NPL's high accuracy reference black body (BB) reference source. The black body reference source provided a stable source with uncertainty around ± 0.2 °C ($k = 2$) fully traceable back to temperature standard ITS-90. To cover the required temperature span of 20 °C–200 °C, two references sources were used. For 30 °C–60 °C range a NH_3 heat pipe and for the 60 °C–200 °C H_2O heat pipe reference source were used. For more details on the source performance and its uncertainties please see Appendix I.

Additionally, another artefact utilised during an assessment of the uncertainty (following section 4.5) is a forest of vertically aligned multiwall carbon nanotubes grown on the silicon wafer. The artefact was utilised due to its extraordinary high emissivity equal to 9.955% making it the 'darkest man-made material ever' [142]. The emissivity of the artefact was assumed to be equal to 1. This type of flat artefact is utilised and analysed in Chapter 5.

4.4.2 Calibration of infrared imager

The calibration was accomplished by comparison with the infrared imager radiance temperature to the temperature of a high stability black body (BB) reference source, within the temperature range from room temperature to 200 °C (see Figure 4.5). This allowed the assessment of the absolute temperature reading of the infrared camera by comparing it with ITS-90 standard.

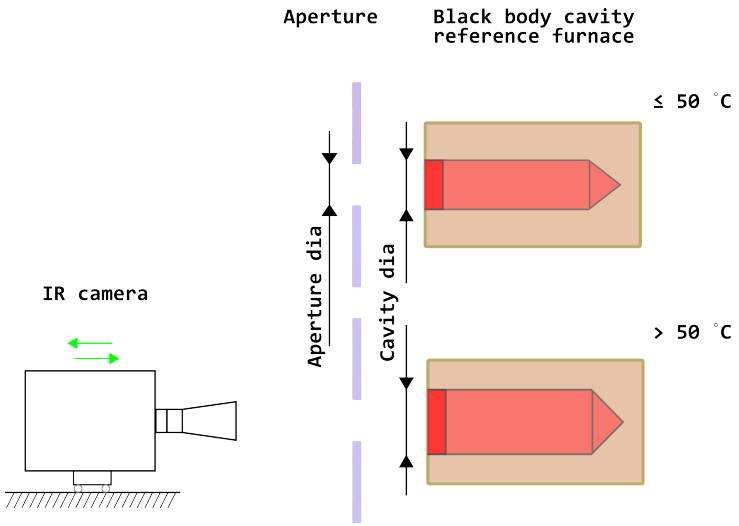

Figure 4.4: Conceptual schematic digram of calibration process. Diagram not to scale.

Setup

The infrared imager (IR camera) calibration is usually placed on a steadily mounted translation stage in front of a calibrated reference source, as shown in Figure 4.4. The position of the imager can be adjusted so it can be aligned centrally to reference source (normal to the defined aperture of the black body) and also to achieve the desired focal length. For both furnaces (30 °C–50 °C and 60 °C–200 °C) a defined aperture of 20 mm in diameter was used. Figure 4.4 shows both black body (BB) references, where the furnaces diameters were equal 20 mm and 40 mm, for a lower and a higher temperature spans, respectively.

Manufacturer settings

The IR camera operates on the calibration provided by the manufacturer and three different calibrations can be selected by the user in the IRBIS3 Professional software. Each calibration uses a different integration time and operates over a different temperature span, as shown in Table 4.2. In-house calibration measurements were taken for a range of set temperatures on the black body reference source, in a sequence for all of shown manufacturer provided imager settings i.e. integration times.

The manufacturer calibration ranges provides the temperature readings by conversion of

Table 4.2: Camera calibration ranges predefined by manufacturer.

Calibration Range	Recommended temperature span	Integration time
Calibration 1	20–100 °C	490 μs
Calibration 2	60–200 °C	60 μs
Calibration 3	100–250 °C	45 μs

an electrical signal[3] acquired by the sensor into temperature scale; temperature readings are based on the confidence in a calibration provided by the Infratec GmbH.

Results

To ensure that the reference source temperature was stable, the setting time was forced to be >1 hour and its temperature monitored. Each calibration data point in the following section was extracted from a rectangular defined region of pixels at the centre of the image with an area of 154 px.

For clarity reasons the normalised results of the actual ITS-90 temperature $T_{Reference}$ and the apparent temperature measured with the instrument ($T_{apparent}$) can be seen in two separate Figures 4.5 (a) and (b) corresponding to two black body radiation reference sources. In the lower temperature span, the Calibration 1 range has a small overestimation of absolute values 3.3% to 1.7% for 30 °C and 50 °C respectively. For the rest of factory Calibration ranges no. 2 and 3 (Table 4.2), both underestimated temperature values. These calibration region were not expected to perform well in absolute temperature measurement outside of the recommended operating temperature ranges. However, calibration range 3 reduced measured magnitude in compare to absolute temperature (of ITS-90 scale) to on average by $\approx$ 7.3% and calibration range 2 significantly dropped expected value ($\approx$ 25%).

For the higher temperature region, around the 60 °C point, 9.5%, 11.6% and 17.7% differences, between actual and camera value were obtained for Calibrations 1, 2 and 3 respectively. At higher temperatures up to 100 °C the all Calibration underestimations

[3]Signal as a digital unit corresponding to sensor output can be acquired instead of a temperature readings. However, these units are impractical since each of Infratecs' calibration ranges readjust the internal settings of camera to provide temperature value.

decreases to a level of around ≈ 7% of the reference magnitude. Above the 100 °C, the underestimation saturates to the level of 5%. As an exception the Calibration 1 is well beyond the recommended span, is losing magnitude after 120 °C, where presumably the sensor became saturated with the longer integration time.

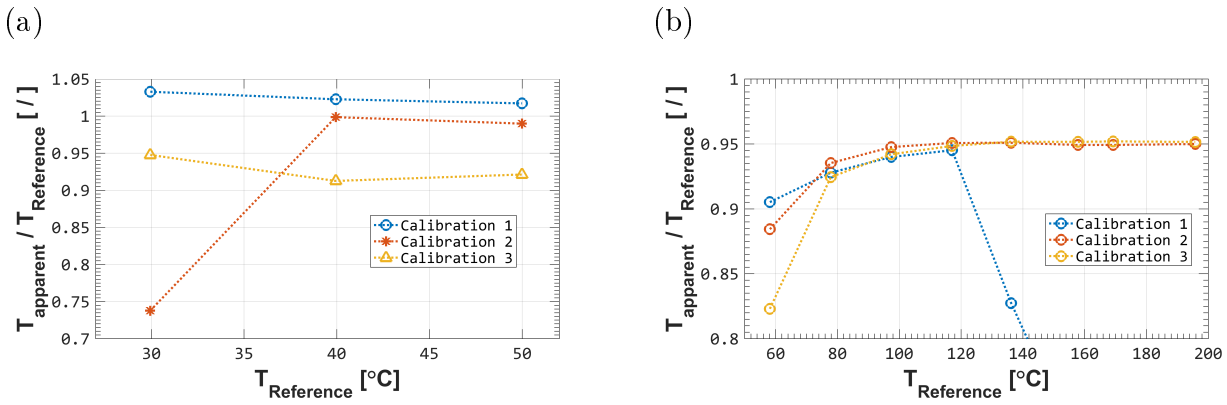

Figure 4.5: Calibration measurements using black body: apparent temperature of infrared imager $T_{apparent}$ vs. reference temperature $T_{Reference}$ (ITS-90), where (a) corresponds measurements to the 30 °C–60 °C range reference source and (b) to the 60 °C–200 °C one.

To investigate the repeatability of the instrument, the process of calibration against NPLs black body radiation references was repeated for selected temperatures the day after, and one month after again. Thus repeatability of instrument based on the relative difference in the absolute values were found to be less than 0.1 °C for the repeated measurements.

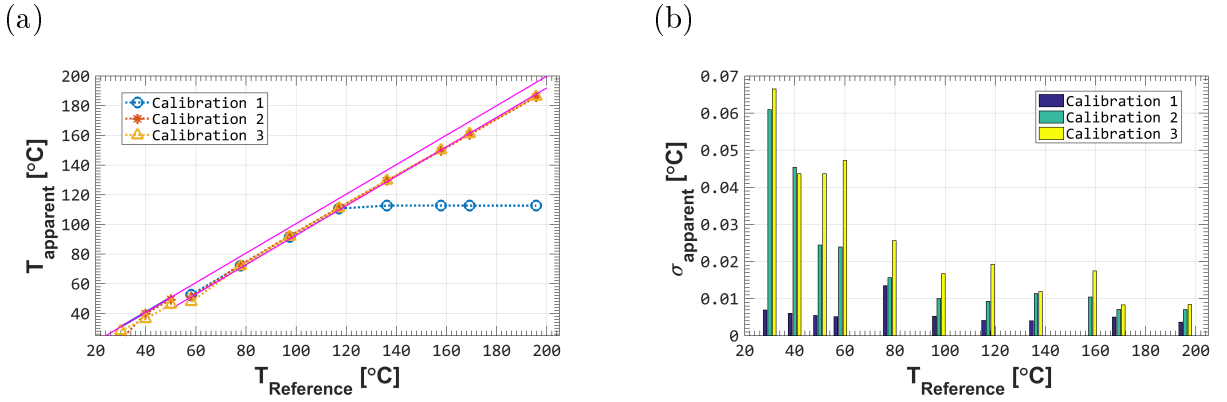

Figure 4.6: Calibration of infrared imager for all factory calibration ranges (a) complied for both black body temperature ranges and (b) standard deviation for each temperatures. Magenta lines in graph (a) represents fitted lines to data from two reference sources.

The data gathered during calibration imply that the factory calibrations are linear. To pinpoint the calibration the absolute values for both ranges are replotted with line fits

in Figure 4.6 (a). At this scale, the difference between calibration magnitudes is barely noticeable, but the fitted lines are shifted (b-parameter) by roughly 8 °C. To assess the quality of the calibration data for each Calibration range the standard deviations are shown on Figure 4.6 (b). The recommended ranges for each of temperature span gives the lowest spreads of values e.g. Calibration 1 range displays the spread below < 0.01 °C at the temperature interval of 20–60 °C.

Figure 4.6 (b) shows the standard deviation obtained for each area per calibration point. Thus to obtain the best performance an appropriate Calibration range has to be selected e.g. Calibration 3 range measured around room temperature gives a spread of $\sim 70\ mK$ whereas the appropriate choice for this operation range is Calibration 1 range which gives a spread of only 8 mK. This contributed to the adjustable integration times and sensitivity integrated to factory settings of the instrument, allowing an optimal performance at low and high temperatures. When the linear fitting was performed in Matlab, by the means of least square covariance matrix, the estimated uncertainty is greater than the uncertainty obtained from the in-house calibration; in other words the fitted points were not included within the calibration's uncertainty bounds. Hence, this would suggest either the estimate of the uncertainty of the instrument versus reference source was calculated improperly, the uncertainty of an accredited calibration reference was underestimated or due to the non-linearity of the instrument. To the author's knowledge the instrument's InSb sensor is mostly likely to be not perfectly linear [143]. Therefore it can be assumed that the IR camera calibration performed according to manufacturer reference source and response was hardware/software (gains, offsets, etc.) adjusted [143]. To exclude some of the possibilities further investigations were carried out detailed below.

4.4.3 Non–uniformity

During the calibration process and investigation of uncertainty budget (in section 4.5), a superior performance of the instrument was established, i.e. reproducibility, stability, sensitivity etc. Still, due to the nature of the infrared cameras, there are a large array

of temperature sensors with individual gains and offsets, which collect infrared radiation through an optical path. Thus it is vital to calibrate the uniformity of the temperature maps obtained with cameras.

The camera was set in front of a reference source in an appropriate position. To change between the calibration settings a laptop with IRBIS 3 professional software was used. To visualise the data without the noise, a double 3rd order polynomial was used to fit the surfaces. Higher order polynomials did not improve the goodness of the fit.

Low temperature range

Figure 4.7 (a) and (b), together with (c) and (d) presents two sets of calibration ranges measured in a sequence one after the other at the same black blody reference sources. In the first pair, the acquired magnitudes and standard deviations across the image, which corresponds to the magnitude of non-uniformity, and are equal to 30.88 $\pm$ 0.09 °C and 28.11 $\pm$0.61 °C, for the calibration 1 and 3 respectively. In the case of higher temperatures these values are 50.15 $\pm$ 0.84 °C and 45.08 $\pm$ 1.12 °C.

All the figures shows non-uniformities with the highest value around the middle and decay at each corner of the image. The 50 °C images, Figure 4.7 (c) and (d), shows clearer correlation in shapes and positions. The fit for calibration range 3 Figure 4.7 (d) is steeper with a smaller area of the maximum values located in the middle, showing that the standard deviation of the magnitude for non-uniformity is greater in (d) than in others.

High temperature range

Figure 4.8 shows the fitted non-uniformities obtained from at the higher temperature source. Analogous to the previous example two black body set point temperatures were selected, namely 60 °C and 100 °C. These were chosen in order to compare the shapes for the same calibrations for different source and for the same preselected calibrations. The magnitudes at 60 °C for calibration 1 and 3 were 52.80 $\pm$ 0.23 °C and 47.79 $\pm$ 0.48 °C,

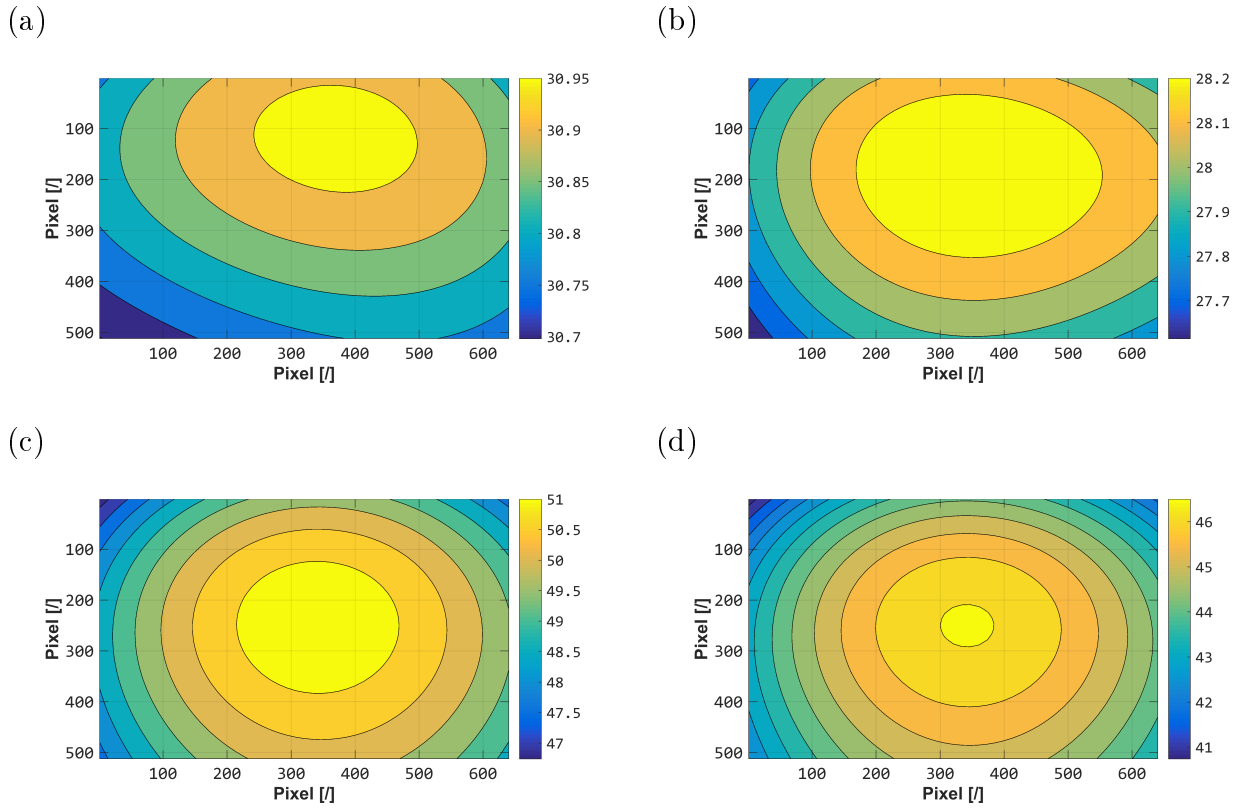

Figure 4.7: Double 3rd order polynomial surface fit presenting uniformity of the lower temperature span reference at 30 °C, for: (a) Calibration 1 (b) Calibration 3, and at 50 °C, for: (c) Calibration 1 (d) and Calibration 3.

respectively and for 100 °C 91.96 ± 0.40 °C and 92.00 ± 0.48 °C, respectively.

Here the shapes are different and not as centred as in the case shown on Figure 4.7. For both calibration 1 at lower and higher temperature, the lower temperature is shown on the bottom of an image Figure 4.8 (a) and (c). Where in case of calibration 3, Figure 4.8 (b) and (d) the shape of the contours are more elliptical. Also in this example the cold zones are in the bottom left hand side and hot one are in the top right hand side.

Non-uniformity – Conclusions

Based on the gathered data it is difficult to conclude the source of acquired non-uniformities. Typically, this would be related to various sources such as optical path issues (e.g. hot air convection, lens aberrations, etc.), calibration facility or instrument pre-set calibration, which would carry a non-uniformity of reference against which it was acquired.

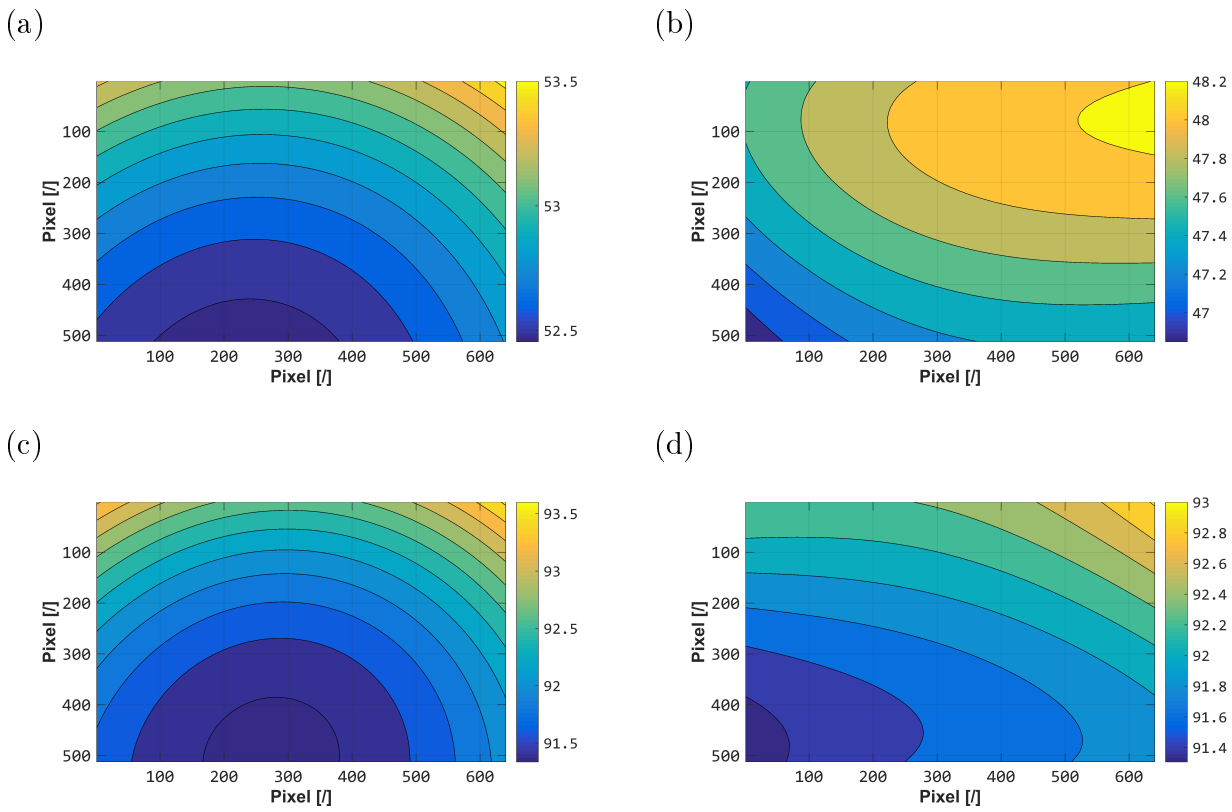

Figure 4.8: Double 3rd order polynomial surface fit presenting the uniformity of the lower temperature span reference at 60 °C, for: (a) Calibration 1 (b) Calibration 3, and at 100 °C , for: (c) Calibration 1 (d) Calibration 3.

One must note, these non-uniformities will contain the curvature of an image and the noise (mostly shot noise[4]), which may introduce an error in the IR images. For example, when compared the 30 °C values the magnitude was equal to 0.09 °C for Calibration 1 versus 0.61 °C for Calibration 3 which due to shorten intergration times is more sensitive than Calibration 1.

The non-uniformity was found to scale with temperature. This was evidenced at temperatures of 50 °C and 60 °C, where for Calibration 1 range the magnitude of non-uniformity was 0.84 °C and 0.23 °C, respectively to temperatures and for Calibration 3 range 1.12 °C and 0.53 °C for the same temperatures. This shows that the sources are not adequate and non-uniformity cannot be concluded unanimously nor compensated for.

Here, one of the best state-of-the-art calibration facility for infrared temperature meters was used. And yet these inconclusive findings lead us to further analyse the facility itself.

[4]Electronic noise associated with discrete nature of light and electric charge.

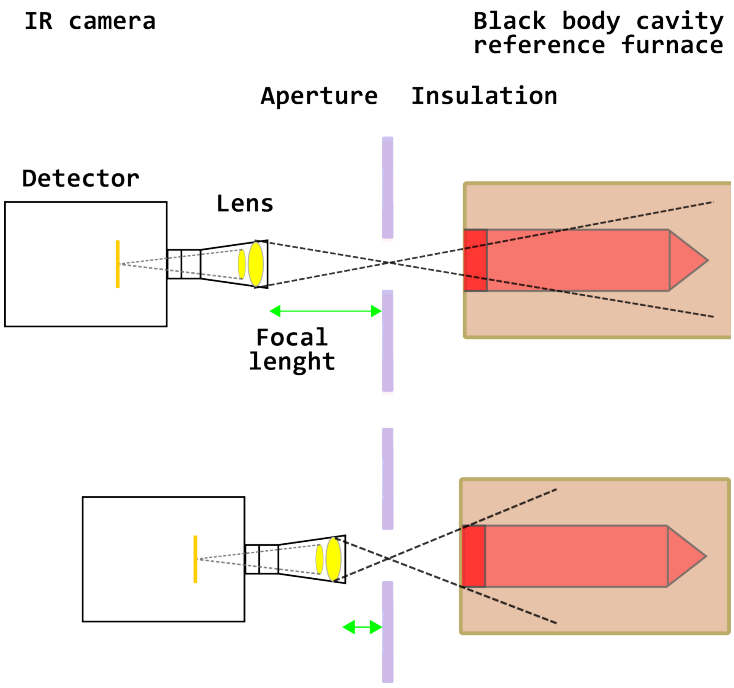

Figure 4.9: Schematic of thermal path between camera and black body source representing calibration issue of μ-scale systems. The macro-size instrument with a long focal length focusing on the blac kbody cavity (top) and μ-scale observing radiation from non-uniform sides insulation (protects against temperature gradients on the open end of black body cavity) or external walls of the cavity.

The calibration sources were optimised for the non-contact thermometers dedicated for measuring macro-size objects. Thus, this would agree with the appearance of the shift in the calibration curve's linear fits for each of the two sources which has different diameters of aperture. Figure 4.9 depicts a comparison schematic of a macro and micro size with various focal length cameras pointing inside or outside of a reference cavity, respectively. A instrument under calibration intended to measure temperature from within the source, what in case of instrument with microscopic lens can not be achieved; micro thermographic instrument will image the insulation region rather the expected interior. Therefore the apparent temperature non-uniformity to the infrared camera depending on the settings can vary up to more than 1.1 °C across the image close to room temperature. Because of the limitation with a current facility, which does not compromise the micro-scale uniform reference, the uniformity cannot be confidently verified.

Lastly, to avoid unnecessary increase of uncertainty due to the non-uniformity, it is recommended to chose the sufficiently small regions of the imaged surface temperature.

4.4.4 Calibration – Summary

The NPL black body radiation reference was designed for the calibration of the typical macro object rather than the micro size objects, hence a 40 mm wide bore of black body cavity with length in at least 1:10 aspect ratio was used. The non-uniformity of the source was then addressed. The linear response was acquired, as was the calibration curve. Additionally, a high reproducibility below 0.1 °C over a time of a month has been found.

The uncertainty of the instrument was calibrated against the NPL state-of-the-art accredited calibration facility providing a traceability to ITS-90 scale, showing the reproducible offset from the absolute temperature scale.

In recent years the scientific community has worked upon flat black body sources, which would be a suitable alternative for the μ-scale calibration. However, there is no existing traceable standard, which would be suitable for this purpose, due to the issues with uniformity of small black body cavities. Preliminary work on the development of such a reference was established and is described in Chapter 5.

4.5 Uncertainty budget

4.5.1 Measurands

The direct measurement of the electrocaloric effect (ECE) refers to the measurement as a transient function of the temperature change ΔT (entropy change ΔS) with the application of a DC step electric field pulse (see example on Figure 4.10).

Therefore the temperature change is measured under isothermal conditions and with application of electric field.

Thus the only measurands are the temperature as true value (T_{true}) and electric field E.

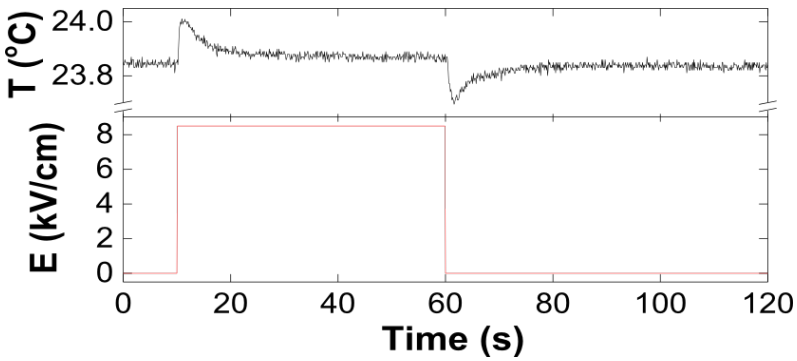

Figure 4.10: Example of electrocaloric ΔT measurement with corresponding electric field as function of time; $Pb(Mg_{1/3}Nb_{2/3})O_3 - PbTiO_3$ specimen measured at room temperature.

4.5.2 Uncertainty analysis

Due to the lack of detailed knowledge about the infrared camera or the possibility to study the internal design, electronics circuits, built-in calibrations etc., a mix of uncertainty type A and B methods have been developed for this system.

The goal of the measurement facility used to quantify the ECE, is to measure the temperature change within the sample under the applied electric field $\Delta T(E)$. Therefore due to the nature of time elapsed measurement the temperature change $\Delta T(E,t)$ the offset (the true temperature value) is not required, thus can be reduced and determined by:

$$\Delta T_{i+1} = T_i - T_1 \tag{4.1}$$

Where T_i is i-th element of the time sequenced measurement and T_1 is the initial temperature (note that as a result the first element of ΔT will always be a 0 value).

Therefore the measured value of temperature with its uncertainties, T_i of i-th element of the time sequence measurement, can be simplified to the term:

$$T_i = T_{i,true} + R_i + S_i \tag{4.2}$$

Where the R_i and S_i are: the random error (this includes 'small' contribution of semi-systematic errors) and systematic error, respectively. Subsequently by substituting equation 4.2 into

equation A.1 and by knowing that the systematic errors are the same for the time sequence we get the following:

$$\Delta T_i = T_{i,true} + (R_i - R_1) \tag{4.3}$$

Due to the subtractive nature of the measurand in this equation, the uncertainty for the ECE measurement facility, will be equal to the random effects added in quadrature according to Law of Propagation of Uncertainty, as follows:

$$u(\Delta T_i) = \sqrt{u^2(R_i) + u^2(R_1)} \tag{4.4}$$

Through the calibration process and analysis of the ECE measurement facility, the most important effects were distinguished and classified as making an important contribution towards the uncertainty, and listed in Table 4.3. These contributions are discussed and characterised in the following subsections.

Table 4.3: List of uncertainty contributions.

Type of effect	Contributions
Random effects	Noise/sensitivity Discretisation noise/precision Stability of the source Stability of the instrument (drift) Slight changes in alignment
Systematic effects	Alignment (focus) Size of Source Effect
Semi-systematic effects (systematic, but sensitive to temperature)	Emissivity Calibration of the instrument Environment

4.5.3 Sensitivity/Noise

Sensitivity is an intrinsic property of the IR thermography system and is associated with the camera's sensor performance and its electronic circuitry. The measurement variation

may occur due to change of parameters such as integration time or temperature of the detector. According to the manufacturer the InSb detector is cooled by a Stirling cooler to $\approx$ 80 K increasing the sensitivity (noise equivalent temperature difference (NETD)) below values of 25 mK for the calibrated temperatures range (20–250 °C).

The following investigation concentrates on the effect of the integration time on the measurand ($T_{apparent}$). It was expected that the higher the integration time, the measured values should be smoother; less noisy. This relation was proven on the 200 samples per measurement and represented as normalised temperature $T_{normalised}$ over the stable temperature readings of the black body radiation reference, see Figure 4.11. Furthermore the manufacturer's claim with regards to the low instrument sensitivity of $< 25\ mK$, was assessed and replicated as presented in Figure 4.11 (where the default integration time for this calibration, Calibration 1, is 490 μs). The reported measurement shows the 2.3% offset from ITS-90 values and the relative sensitivity span of $\approx 0.1\%$, when compared to a temperature black body reference source. The values of measured noise for each of the integration times are listed in Figure 4.11 and can go down to $\pm$ 8 mK for the longest integration time of 1000 μs.

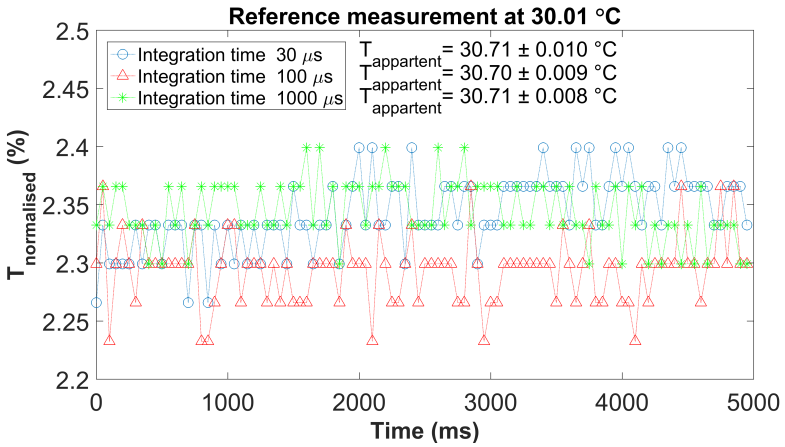

Figure 4.11: Sensitivity measurement presented as relative temperature reading as function of integration time at black body reference source of 30.01 °C.

Therefore the sensitivity of the Infratec ImagerIR for the worst case scenario has a normal distribution and is equal to $\pm 20\ mK$ with coverage factor $k = 2$.

4.5.4 Short term drift

This is an intrinsic property of all electronic devices and is related to the internal fluctuations in performance of passive electronic components and integrated circuits as a function of time; typically due to an internal rise of temperature to 'steady' operating level.

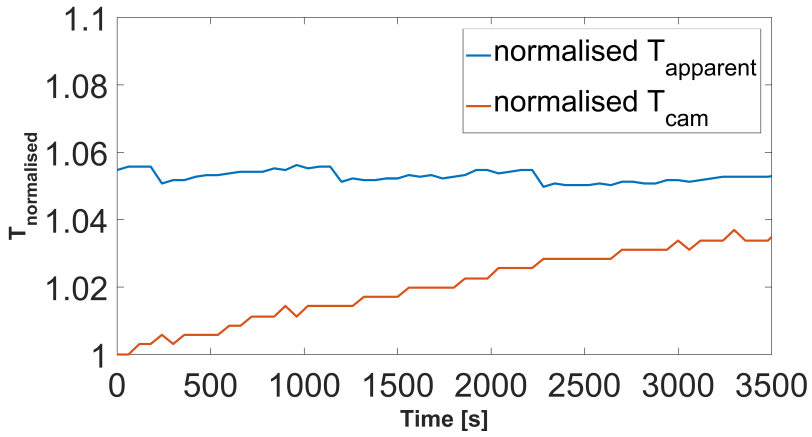

Figure 4.12: Normalized measured and instrument temperature short term drift of the infrared camera over 1 hour period, measured at 20.09 °C.

The imager was set up against NPL's black body source at a known stable temperature straight after switching it on and recorded for 1 hour, 1 Hz rated sequence of thermal images. The results are presented in Figure 4.12 , where the normalised internal temperature of the camera (T_{cam}) is green line and the BB measured temperature ($T_{apparent}$) is blue line. Drift for the periods of around 20 minutes shows the temperature fluctuation of 0.5% of the initial value (the absolute temperature drift is 0.1 °C). The IR system shows a dependency between the camera's temperature increase and the subsequent drift of the read value and the characteristic compensation formed in the shape of sawtooth wave. This suggests that the IR system has built-in drift/gain compensation, which leads to small, finite jumps in the measured temperature of temperature stable samples.

4.5.5 Stability of the measurement artefact

The stability of the measurement artefact, in the analysis of the uncertainty budget, contains the following assumptions related to a measured artefact:

- emissivity is constant for the measured ΔT,
- the sample surface is flat and uniform throughout the measurement,
- the artefact is static, it does not change its position,
- the dimensions are static (the piezoelectric effect and thermal, expansion are negligible, when estimated to be around 10 μm).

Specimens exhibiting the electrocaloric effect are typically ceramic specimens, which 'are stable' materials, in relation to the terms listed above. However these assumptions are not always true and may vary depending on material. Therefore precautions with respect to changes in emissivity and dimensions of characterised specimen should be taken to avoid additional unquantified uncertainties.

4.5.6 Alignment (focus)

The infrared imaging camera is an optical system, which measures the infrared radiation of the surface and converts detected light into a digital signal corresponding to the surface temperature of the body. Therefore a similarity to optical microscopy can be seen, when the image is out of focus the measured dimensions may vary, here instead the acquired thermal image will contain an 'unfocused temperature' region on a thermograph. Figure 4.13 illustrates the setup of the camera's field of view (FOV), and the focused view is present with the green dashed line. The unfocused area might be illustrated as radiation which is partially in focus and the remaining radiation which is no longer detected. This leads to an error for the measurement with respect to alignment between artefact and the instrument.

In order to assess the effect of focus on the absolute temperature measurement, the absolute temperature of a high emissivity reference artefact with combination of typical specimen at different distances between the camera and two type of artefacts were measured. Namely the carbon nanotubes (CNT) artefact and a commercial X7R ferroelectric multilayer capacitor (more details Chapter 7) were employed. Due to the fine displacement tuning

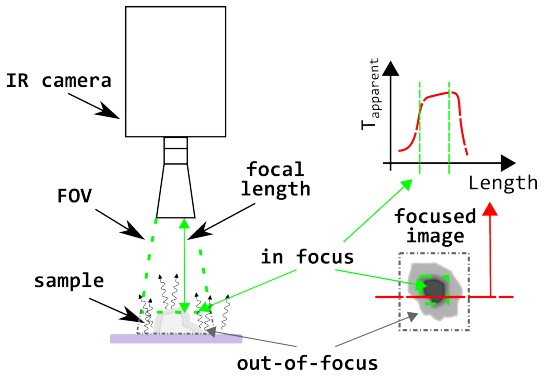

Figure 4.13: Schematic illustrating IR thermography focus error issue. The red line on a inset graph represents a hypothetical temperature profile $T_{apparent}$ apparent for a infrared camera of a non-flat artefact with features out of the focal plane.

of the camera position with respect to observed bodies two types of measurements were carried out; continuous and finite position change. Both were measured at room temperature ($RT \approx 24$ °C). The focal distance of IR camera with 3x microscopic lens is 22 mm. In order to achieve a focused image on the carbon nanotubes (CNT) artefact, it was placed on the top of the greybody artefact.

Figure 4.14 (a) shows the apparent temperature as a function of the IR camera's relative position over a distance of 14 mm, during continuous position change. The apparent temperature reading corresponding to the X7R capacitor surface is located at around 44 mm; the focused image. Once the IR camera is moved either towards or away from artefact, the apparent temperature rises and by the operator it is seen as out of focus image. Such images are blurring out with detected radiation of surroundings and black background, what is observed as a temperature rise. Further in Figure 4.14 (b) the measured steady state absolute temperature of both: the CNT and on X7R capacitor as a discretised function of position, every 0.5 mm, is presented within a distance of ± 1.5 mm from the focus point on each of the artefacts.

The focal points are observed as peaks in Figure 4.14 (b), where for the black body artefact as the maximum point at 39.5 mm and for the grey body as a minimum at 39 mm of relative distance. This agree with the thickness of the CNT artefact was roughly 0.6 mm thick. The difference in temperature absolute value is an outcome of the surface emissivity in artefacts. The emissivity also manifests in the shape of the curves convex, when the

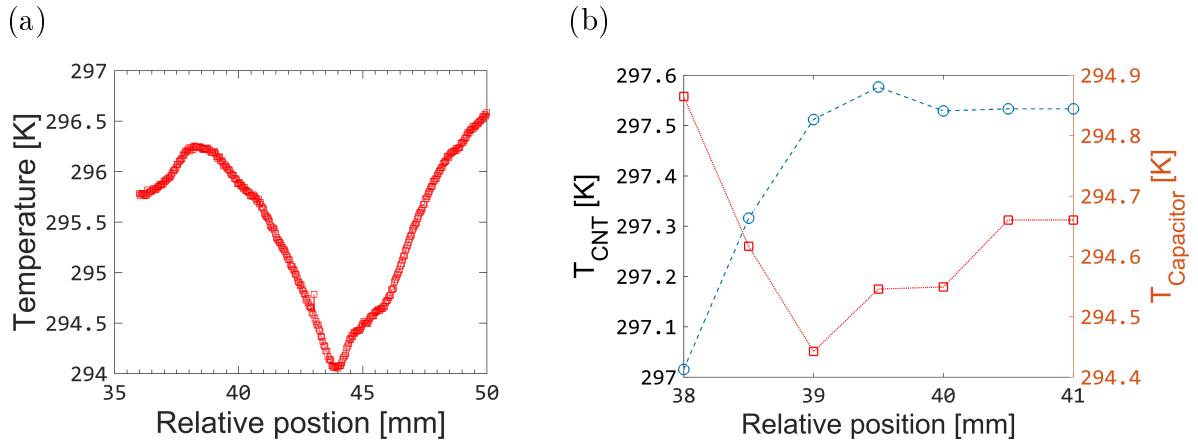

Figure 4.14: Influence of focusing on the temperature reading for the carbon nanotubes (blue circles) and X7R capacitor (red squares) surfaces as a continuous function of camera position for the (a) short (3 mm) and (b) long (12 mm) focal span.

IR camera is far/close the blurriness of the image averages the signal over larger areas of the image which are not related to surface temperature any longer.

Based on measurements of these 6 discretised positions, a difference of 1.5 mm with respect to the specimen results in the difference of around ≈ 0.6 K for CNT (see blue line with circle markers). This difference in height is distinguishable by the operator as blurry image. Similarly the focus influence on temperature reading for the grey body surface (the capacitor, which has a lower emissivity ≈ 0.75) results in a temperature change of around 0.5 K for 1 mm. The standard deviation on each of the measurement point is around ≈ 10 mK (for CNT < 10 mK) with confidence factor $k = 1$ based on sample of 50 measurements.

Due to the nature of the focusing, this is an assessment of the image sharpness based on human factor, the value of 0.1 mm in terms of alignment, is appropriate and safely overestimation of the actual value. From the operator's perspective this value varies in the range of tens of micrometers. Therefore this could be lowered by implementation of a computer algorithm. This alignment of 0.1 mm corresponds to the 0.05 K difference based on X7R results. On the other hand based on the CNT, the difference in measured temperature is 0.04 K (for 0.1 mm of alignment). From the operator's point of view the focus is not strongly related to the emissivity of the sample, however it affects the reading. Emissivity will be assessed in the further subsection. Furthermore the correction of lower

emissivity can be made after the measurement and remove the effect in the error from the applied alignment of the camera.

Therefore the alignment contribution to the uncertainty is estimated as 0.04 °C ± 0.01 °C per 0.1 *mm* in alignment change, for normal operation conditions.

4.5.7 Size-of-source effect

The size-of-source effect (SSE) is an imperfection of all optical systems and originates from the scattering and diffraction of the measured radiation. In practice for IR thermography it appears as an error in temperature reading and it depends on the distance from objects, and size of the object plus surrounding of the area [144].
This effect is typically related to fixed angular field of view (FOV) Φ_{FOV} described as relation of distance to spot size ratio given by equation:

$$\Phi_{FOV} = 2\tan^{-1}(\frac{S}{2D}) \tag{4.5}$$

The optical performance, the SSE, of the imager was assessed with the NPL's infrared calibration facility. For different aperture sizes placed in front of the black body cavity stable at its defined set point temperature the infrared imager temperature was measured while the aperture size was changed. The following set of SSE apertures size were 0.75, 1, 2, 3, 4, 5, 7, 12, 20 and 30 *mm*. The results show that apparent temperature differs with sample size. This is denoted in the Figure 4.15 for two black bodies set point temperatures of 60 °C and 200 °C. The value measured by the IR camera is an average of around 91% and 95% of the real value with 20*mm* aperture, for low and high temperatures respectively. The significant drop for the apparent values is noticeable size of 1 *mm* and below. Furthermore this suggests a drop in the apparent temperature of around 9% and 10% for around 60 °C and 200 °C, respectively. The field of view of the imager is around 3.20 × 2.56 *mm* which suggests that only 3 apertures reduced the size of imaged BB source. In this instance the change in the diameter of source was too coarse and it is

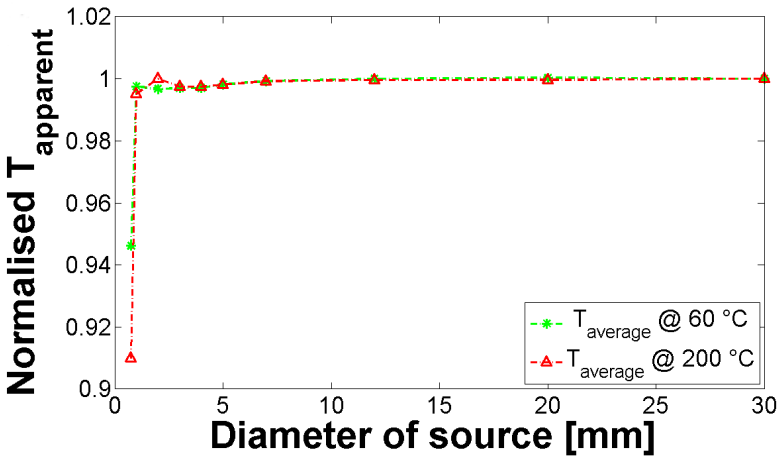

Figure 4.15: Normalised size of source effect represented as a function of normalised apparent temperature to the IR camera $T_{apparent}$ to the source aperture diameter.

difficult to assess the SSE. However it is safe to assume that measurements of the objects not smaller than 1 mm maybe considered as appropriate without any significant error. Otherwise the finer SSE evaluation should be done to evaluate errors.
However to the author's best knowledge there is no standardised reference source which could be used for such purpose and therefore to quantify this effect in micro-scale a new artefact was developed (see Section 5.1).

4.5.8 Emissivity

Emissivity (ε) is the measure of a specimens ability to emit and absorb infrared radiation, herein infrared light (spectra of $2-5.6\ \mu m$). The concept of a perfect object exhibiting an ideal emissivity equal to 1, is a black body. Such a body, when exposed to perpendicular incident electromagnetic radiation, absorbs all of the radiation; in other words, none of the incident radiation is reflected. Therefore, in the case of a black body the apparent radiance of the investigated surface area at the given temperature will directly correspond to the temperature of the body and will obey the Stefan-Boltzmann law (see below eq. 4.6):

$$\frac{E_{thermal}}{A} = \varepsilon \sigma T^4 \tag{4.6}$$

where σ is the Stefan-Boltzmann constant ($\approx 5.6793 \times 10^{-8} W m^{-2} K^{-4}$) and $E_{thermal}$ is the radiated thermal energy per unit area A of the body with known emissivity ε (for black body $= 1$) at the temperature T. However typically, investigated bodies are not black bodies, and more commonly are grey bodies ($\varepsilon < 1$). Thus while measuring the grey an error in the measured absolute value of temperature corresponds to the value of emissivity and others parameters (see below subsection 4.5.9).

The measurements of the true value of surface temperature are affected by the emissivity of the device under test (DUT), since the instrument by default assumes that examined objects are black bodies. Therefore it is good practise to compensate this error by knowing the properties of the object. By knowing the actual temperature and effective wavelength corresponding to the utilised instrument, compensation can be made by application of a correction based on Wien's law [145].

$$\frac{1}{T} - \frac{1}{T_{apparent}} = -\frac{\lambda}{c_2} ln\varepsilon(\lambda) \tag{4.7}$$

Where the T, $T_{apparent}$, λ, $\varepsilon(\lambda)$ and c_2 are the true temperature, apparent temperature measured at the body, mean effective wavelength, the emissivity at the specific value of mean wavelength and second radiation constant, respectively.

To the author's knowledge the infrared camera InSb sensor operates at the spectra wavelength between 2 μm to 5.7 μm, which corresponds to a mean effective wavelength of 3.85 μm. Numerically solved equation 4.7 for above values of wavelength is represented in Figure 4.16 as a function of the error in estimation of emissivity with the imager (arrow indicates higher temperatures). One may see that for the close to room temperature measurements the low emissivity results in significant relative error in estimation of the emissivity, e.g. error $\approx 13\%$ for $\varepsilon = 0.8$ at 20 °C. Furthermore by taking the derivative of equation 4.7 with respect to true temperature T the estimation in small ΔT the following may be obtained:

$$\Delta T = \Big(\frac{\lambda}{c_2} ln\varepsilon(\lambda) \cdot T - 1\Big)^2 \cdot T_{apparent} \tag{4.8}$$

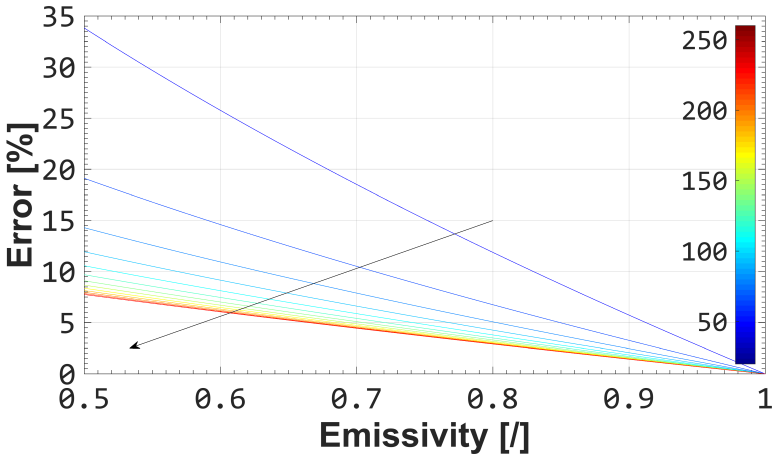

Figure 4.16: Plot of error in emissivity estimation as a function emissivity for temperature range from 20 °C to 260 °C, numerically solved based on Wien's law. Arrow indicates temperature in ascending order.

Where $\Delta T_{apparent}$ is a temperature difference measured with instrument and T is the true temperature at which the $\Delta T_{apparent}$ was measured. This simplified version of Wien's law can be used to estimate the effect of the greybody emissivity on the true value of ΔT both for known temperature T acquired from the embedded thermocouple or by comparison specimen temperature $\Delta T_{apparent}$ versus true temperature T measured on the CNT reference artefact. Note that the expanded uncertainty for standard thermocouple K type used in the setup is 1.5 °C (from -40 °C to 333 °C).

In order to reduce the uncertainty emerging from the lower emissivity of DUT, high emissivity paint can be used on relatively big bulk samples (relative field of view is around $3.2 \times 2.5\ mm$). The paint PyroMark 2500 and Armeco 840M were used. Both of these paints exhibit emissivity more than 0.9 from room temperature to above 1000 °C. Advantageously, such a solution of using black paint allows the use of known emissivities without the necessity of estimation, which further lowers the uncertainty. Conversely, a known emissivity artefact placed in field of view can be used to estimate more precisely the surface emissivity of the body.

4.5.9 Environment (external radiation, sapphire window)

The temperature measured by the thermal imager corresponds to the spectral radiance of the examined body. Most common specimens are not black bodies measured in non-perfect conditions therefore the emitted thermal radiation $E_{thermal}$ as a function of wavelength λ and temperature T needs to include other factors:

$$E_{thermal}(\lambda) = \alpha(\lambda) + \rho(\lambda) + \tau(\lambda) = 1 \tag{4.9}$$

where $\alpha(\lambda)$,$\rho(\lambda)$ and $\tau(\lambda)$ are the absorption, reflection and transmission at the time of measurement at the given λ [145]. For an opaque body transmittance is equal to 0. According to Kirchhoff's thermal radiation law the absorption α_λ is equal to ε_λ at the given wavelength.

Reduced equation 4.9 for solid non-opaque bodies to $\varepsilon(\lambda)+\rho(\lambda) = 1$, shows that the lower the emissivity ε of the sample, the higher the reflectivity ρ. Hence the higher reflectivity leads to extra errors arising from external radiation. This reflection can come from the surrounding/background, any warm objects, sources of light, human body etc.

The environment at which the measurement is carried out may lead to additional errors. The transmittance of the optical medium in between the target and the infrared imager can attenuate the signal observed at the instrument. Typically the optical medium, in which the measurements are carried out, is air, and its transmittance may vary on density of dust particles and relative humidity. Another incidence on the optical path is the semi-transparent window. The attenuation of the signal with and without the window evaluated on carbon nanotubes indicated 4% drop through the window.

Temperature and humidity

The setup is kept in an air-conditioned laboratory with constant temperature set to 24 °C. However to cross check this setting additional measurements were done with a temperature and humidity logger, the Gemini TV-4500. The mean value of the temperature of 23.67 °C

and standard deviation of ± 0.32 °C and with relative humidity 48.3% ± 5.41%, both acquired with the logger located close to the test chamber for a span of 11 days. The logger was not calibrated and according to the manufacturer the resolution and accuracy of instrument are 0.02 °C, $< 0.3\%$ RH and ± 0.4 °C $\pm 3.0\%$, for temperature and relative humidity respectively.

External radiation

Due to the structure of the setup, mainly the size of the lens and its' low 22 mm focal length the external radiation is blocked and can be neglected. This was tested with a gold coated mirror with an effective mean reflectivity $\rho \approx 98\%$ (for the wavelength of interest; $2.0 - 5.7$ μm) placed at the setup. The experiment, where the source of radiation, namely a hand of operator and a gas lighter, were placed close to the camera objective. No effect on the temperature reading from the reflective surface has been observed, what proved sufficient shielding against external radiation. When the setup is modified and the investigated body is placed out of the chamber the additional shielding covered with high emissivity paint ($\varepsilon \approx 0.9$) is utilised. Similar experiment has been used to verify the quality of such arrangement.

This allows us to assume that the optical path between the instrument and device under test, and due to the controlled laboratory environment is not affected by atmospheric effects, thus the transmittance is $\tau = 1$; infrared radiation of interest is not attenuated at these conditions. In the current case, the air absorption of a short focal distance was neglected.

4.5.10 Electric field

Electric field is expressed as the applied voltage V divided by the thickness d of the specimen:

$$E = \frac{V}{d} \tag{4.10}$$

Sample thickness

This depends on the nature of the sample. The bulk specimens' thicknesses are measured with an electronic micrometre. Typically the thickness is measured with a calibrated instrument twice and the mean value is used.

The specimen's thickness is measured with calibrated electronic micrometer with an accuracy of $\pm 0.001\ mm$. The lowest division on the instrument scale is $0.001\ mm$. It can be roughly estimated that due to the operator the additional error in the thickness measurements can be equal up to $0.004\ mm$. Using the law of uncertainty propagations, one can obtain the standard uncertainty of $\pm 0.004\ mm$ [5] and expanded one equal $\pm 0.008\ mm$ (with confidence $k = 2$).

Sample flatness and parallelism

The specimen flatness and parallelism may affect the uniformity of electric field within the sample. Therefore as an example let us consider the homogeneous ceramic cuboid $4\ mm \times 4\ mm$ and $1\ mm$ thick, coated with typical metallic electrodes on the larger faces (the $4\ mm \times 4\ mm$), and that the parallelism of it is affected by $+20\ \mu m$ to -20 μm from the assumed ideal $1\ mm$ thickness on the each far end of the edge (see the Figure 4.17). This corresponds to 2% parallelism with respect to the bottom wall. Thus once considering the thickness of $1\ mm$ with applied voltage of $1\ kV$ will result in $10\ kV\,cm^{-1}$ ($1 \times 10^5\,V\,m^{-1}$) and at the 2% perfectly tilted surface will result in $10.2\ kV\,cm^{-1}$ and $9.8\ kV\,cm^{-1}$ (as well $\pm 2\%$ relative difference in electric field). Based on the review [19] the maximum reported value of the electrocaloric temperature change to applied field $\Delta T \cdot \Delta E^{-1}$ was around $\approx 2.3 \times 10^{-6} m\,K\,V^{-1}$ at the maximal applied electric field of $12\ kV\,cm^{-1}$ for the single crystal PMN-PT 72/28. Therefore the considered tilt of the top electrode surface and its variation of electric field could result in a change of $\approx \pm 0.09$ °C for the EC ΔT measured on each of the sides (assuming that the specimen does not breakdown under

[5] Note that the combined uncertainties of $0.001\ mm$ and $0.004\ mm$ results in $0.0041\ mm$ and this value is rounded down due to overestimated previously error arising from the human factor.

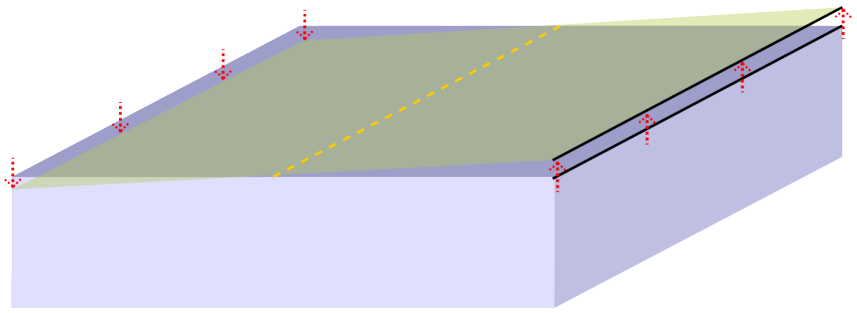

Figure 4.17: Schematic diagram of the tilted surface with relation to the ideally parallel specimen

the higher localised field).

Conversely polymer materials typically achieve the $\Delta T \cdot \Delta E^{-1}$ is in range $< 0.2 \times 10^{-6} m\,K\,V^{-1}$ and undergo very high fields above $1000 kV cm^{-1}$ ($100 MV m^{-1}$). Therefore, when considering such tilt of $\pm 2\%$ would result in $\approx \pm 0.42$ °C (relatively $\pm 2\%$) on each of the sides (for the example of the Terpolymer P(VDF-TrFE-CFE) (56.2/36.3/7.6) [64], where the $\Delta T = 21.6$ °C for applied field of $\Delta E = 350\ MV\,m^{-1}$, $\Delta T \cdot \Delta E^{-1} = 0.06\ \times 10^{-6} m\,K\,V^{-1}$).

One may note that in such a simplified example, the greater the error in the parallelism, the greater the error in the applied electric field. Hence a non uniform distribution will lead to error in measurement of EC temperature change. The assumption of the parallelism may lead to under- or over- estimation of ECE temperature change. However, this will not apply to caloric measurement methods since the measured value is normalised to the whole volume of a body.

A similar approach can applied for the roughness/flatness of the specimen. The higher the roughness, the higher the difference between the maximum valley depth and maximum peak height, which will create the localised electric fields leading to localised variations in the readings of EC temperature change across the surface. However these localised temperature variations, depend on the specimens: thermal mass, thickness, thermal properties and the time scale of such event.

Excitation voltage

The voltage to the sample is applied via a commercially available ferroelectric tester. The voltage is set by operator by inputting the desired value in the software. The applied voltage was measured with the Tektronix multimeter TX3 with the calibrated HV probe for the Trek 610E HV amplifier in the 1 kV (100× amplification) range and the same instrument in the 10 kV (1000× amplification) range. Together, the voltmeter with probe was calibrated for HV reading in the external laboratory with the uncertainty of $\pm 0.2\%$ in DC measurements.

Each voltage level was measured out at constant DC voltage set in Aixacct software. This was repeated 5 times for each set voltage.

Trek amplifier 1 kV

The standard deviation of the measured voltage typically was lower than $< 0.02\%$. The relative value of the set voltage to the measured value is shown in Figure 4.18. On average the relative voltage (set value to the true value) is around $< 1.2\%$.

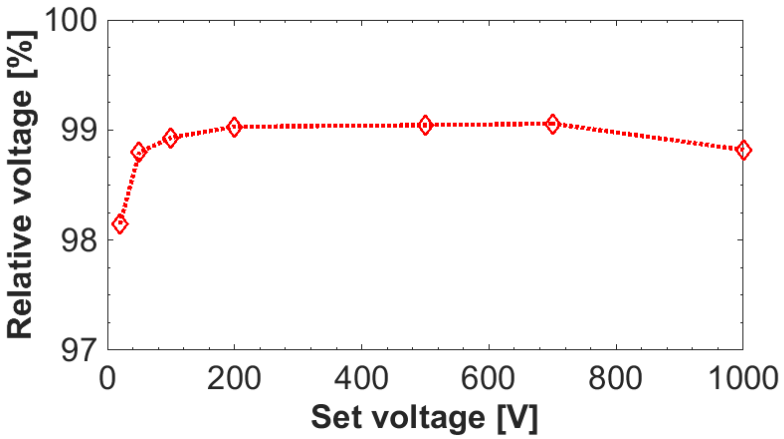

Figure 4.18: Applied voltage verification; the plot of relative voltage to set voltage for 1 kV range.

Trek amplifier 10 kV

The standard deviation of the measured voltage typically was lower than $< 0.5\%$. It is most noticeable that the relative difference in the applied voltage to set parameter at the end of amplifier range can reach almost 5% for 10 kV (see Figure 4.19). However across

the operating voltages' span, which typically do not exceed 7 kV, the relative voltage on average is no more than $< 1\%$ difference between set and applied voltage.

To sum up once using the uncertainty propagation law, for the operating conditions the

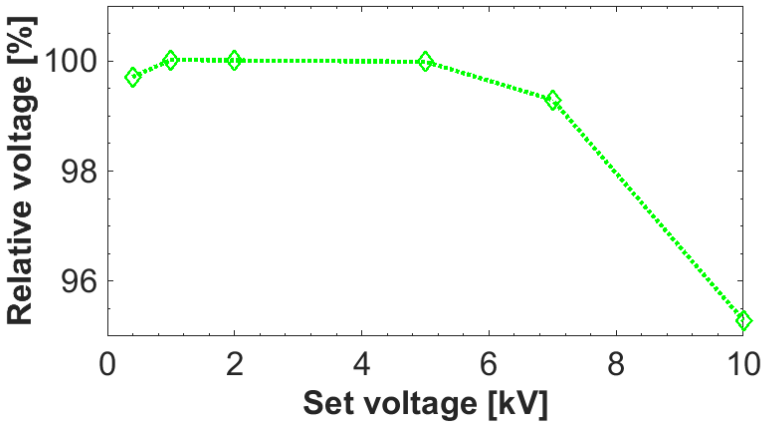

Figure 4.19: Applied voltage verification; the plot of relative voltage to set voltage for 10 kV range.

applied voltage to the specimens against set value, the relative uncertainty are equal to 1.22% and 1.02% with the confidence factor $k = 1$ for the 1 kV and 10 kV high voltage range.

Overall for calculating the uncertainty for electric field by taking the partial derivative one obtain the following equation:

$$u(E) = \frac{1}{d} \cdot u(V) + \frac{V}{d^2} \cdot u(d) \tag{4.11}$$

where the $u(E)$, $u(V)$ and $u(d)$ are the uncertainties of the electric field, voltage and thickness respectively. So by considering the specimen $d = 1 \pm 0.004\ mm$ and the applied voltage of $1000 \pm 10.2\ V$ with Trek 10 kV source with their standard uncertainties, results in the $10 \pm 0.142\ kV\,cm^{-1}$ with the coverage factor $k = 1$.

Note that the lower the thickness of the specimen the higher uncertainties. The relative standard uncertainty for the following example is equal to 0.4%, and since the combined uncertainty of thickness measurement has always same value of $\pm 0.004mm$, consequently the decrease in thickness increases it proportionally. Thus by taking the most extreme example, while measuring manually the thickness of 100 μm will result in relative uncertainty

of $\pm 4\%$. Consequently by applying 1000 V, this results in the 100 $\pm$ 5.02 $kV\,cm^{-1}$ with coverage factor $k = 1$ (relatively $\pm 5.02\%$).

4.5.11 Conclusions

It is important to acknowledge that the general model of the measurement requires and assumes that while the measurement is performed the;

- artefact is measured close to the adiabatic conditions;
- emissivity of artefact sample is constant for measured ΔT;
- artefact is static, does not change position;
- artefact surface is uniform, hence the surface temperature;
- artefact is not reflective sample, $\varepsilon_{sample} \geq 0.4$;
- Electric field is uniform and perpendicular to electrode surface.

Based on the above uncertainty analysis and on the above assumptions including that the object size is not smaller than 1 mm and measured for no longer than 10 minutes, the electrocaloric effect on two hypothetical samples (sample A and sample B) was investigated.

The two samples have the same thickness of 1 mm and are tested under application of 3 kV of potential across the sample. Table 4.4 shows the short version of the uncertainty budget for sample A and B. The expanded uncertainty budget table is shown in Appendix B.

Hence the thickness of 1 $\pm$ 0.004 mm thick ceramic puck subjected to voltage of 3000 V $\pm$ 2% resulted in ΔT = 1 °C for sample A and ΔT = 10 °C for sample B indicated on the instrument. Therefore the applied electric field will be corresponding to 30 $\pm$ 0.426 $kV\,cm^{-1}$ for sample A ΔT = (1.05 $\pm$ 0.11) °C of a standard uncertainty ($k = 1$) covering 65% of confidence.

Table 4.4: Uncertainty budget for electrocaloric ΔT acquired at 20 °C for sample A and B with surface emissivity $\varepsilon = 0.8$.

	A: $\Delta T = 1$°C	B: $\Delta T = 10$°C
Source of uncertainty	Value of uncertainty °C	
Alignment	0.02	0.02
Calibration	0.09	0.09
Drift	0.06	0.06
Emissivity compensation	0.02	0.12
Sensitivity	0.01	0.01
Parallelism	-	0.21
Combined uncertainty	0.11	0.26

In the case of sample B, the 2% tilt of sample parallelism will be included. Hence the thickness obtained for sample B is equal to $d = (1 \pm 0.021)\ mm$. By assuming a linear relation of E-field to ΔT_{EC}, the acquired value at the temperature of 20 °C is $\Delta T = (10.46 \pm 0.26)$ °C of standard uncertainty ($k = 1$) as a result of an electric field of $(30 \pm 0.612)\ kV\,cm^{-1}$ ($k = 1$). In a case if sample B would be parallel, the obtained result measured at exactly same conditions would be $\Delta T = (10.46 \pm 0.53)$ °C, where $\pm$ symbol is a numerical value of an expanded uncertainty of $U = k \cdot u_c$, $u_c = 0.26$ °C and $k = 2.04$ based on the normal distribution for $\nu = 68$ degrees of freedom defining an interval of 95% confidence, under electric field of $E = (30 \pm 0.426)\ kV\,cm^{-1}$ with confidence factor of $k = 1$.

Therefore the uncertainty magnitude for the current setup is mostly originating due to the lower surface emissivity of specimen, calibration and drift. The emissivity compensation, as shown in eq. 4.7, it is scaling with the magnitude of the ΔT and also is affected by the temperature of measurement. The calibration and drift are secondary and much lower components that improvement would not reduced considerably the combined uncertainty. However, at the lower magnitudes of ΔT emissivity contribution can reduce to the level where these two parameters may become significant. Specimens parallelism has a great effect on the combined uncertainty of the EC measurement, what is shown in the example of $\Delta T = 10$ °C where it magnitude become higher than uncertainty arising from the emissivity compensation. This aspect is usually not concerned in electrocaloric

publications and as shown here can contribute to under/over estimation of a local electric field leading to misinterpretation of acquire results. This especially may affect EC measurements at high electric fields where small difference in thickness would manifest much higher electric field values than expected by the operator.

Chapter 5

Characterisation of measurement setup

In this chapter, further investigation of the infrared camera and about determining its limits: 1) to resolve the small temperature changes, 2) to determine the size-of-source effect up to μ-size and 3) to characterise the ability to measure the temperature changes in the designed environment are covered.

Each of the three sections are constructed in the following way, first the aim of each study will be specified followed by the description of an artefact, changes around the setup and finally with results and discussions.

5.1 Non-uniformity and micro-scale size-of-source effect based on carbon nanotubes

The goal was to develop a novel flat artefact for the assessment of the micro-sized size-of-source (SSE).

Based on the measurement of the macro-sized SSE it was concluded that objects $> 1\ mm$ in size do not affect the temperature measurement ($\approx 1\%$, see Section 4.5.7). However the electrocaloric samples are often thinner than $1\ mm$ due to their beneficial scaling between the thickness and temperature changes.

5.1.1 The artefact

Typically the standard and reliable source of the black reference are an black body (BB) cavities. The proportion of at least 1:10 in the diameter to the depth of the hole allows light absorption close to 100% (emissivity $\approx$ 1) [142]. Nonetheless, micro-size black body cavities are difficult to achieve and to stabilise. Therefore, in this work we solely concentrated on flat black sources.

The recent invention of the high emissivity carbon nanotubes enables sufficient blackness on a flat surface. Their unique structure, a forest-like alignment of multiple tubes spaced at nano-mirco level, makes them the material with $\epsilon \approx 0.9986$ [146]. Here, vertically aligned multiwall carbon nano-tubes (VAMCNT) will be used.

Design

The specimen is based on a silicon wafer on which the vertically aligned carbon nanotubes (CNTs) are grown [147]. A continuous pattern of eight circles are depicted on a schematic diagram, see Figure 5.1. Sizes (diameter) and distribution (gap in between) have been chosen in ascending order and are presented with numerical values in the Table 5.1.

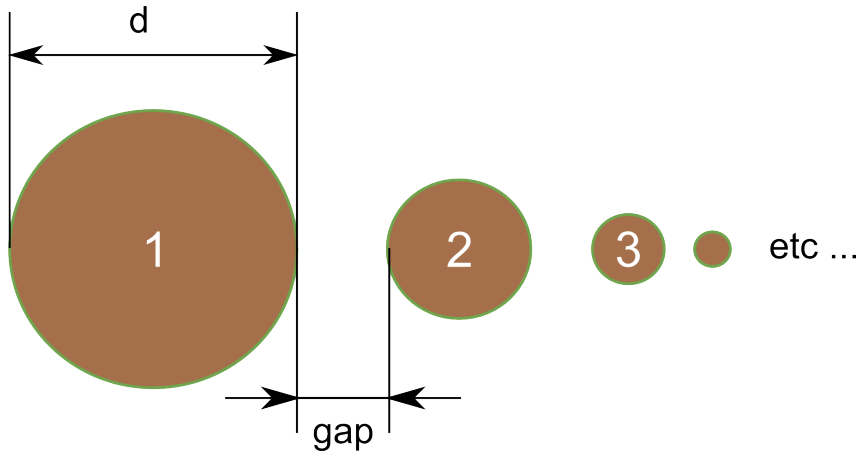

Figure 5.1: A configuration schematic of silicon-CNT artefact. For the dimensions (d) and gap between circles CNT islands, see Table 5.1.

Table 5.1: Designed dimensions of the size-of-source artefact islands diameter d and the gap in between each CNT island.

	Number							
	1	2	3	4	5	6	7	8
d [μm]	3200	1600	800	400	200	100	50	25
gap [μm]	800	400	200	100	50	25	12.5	

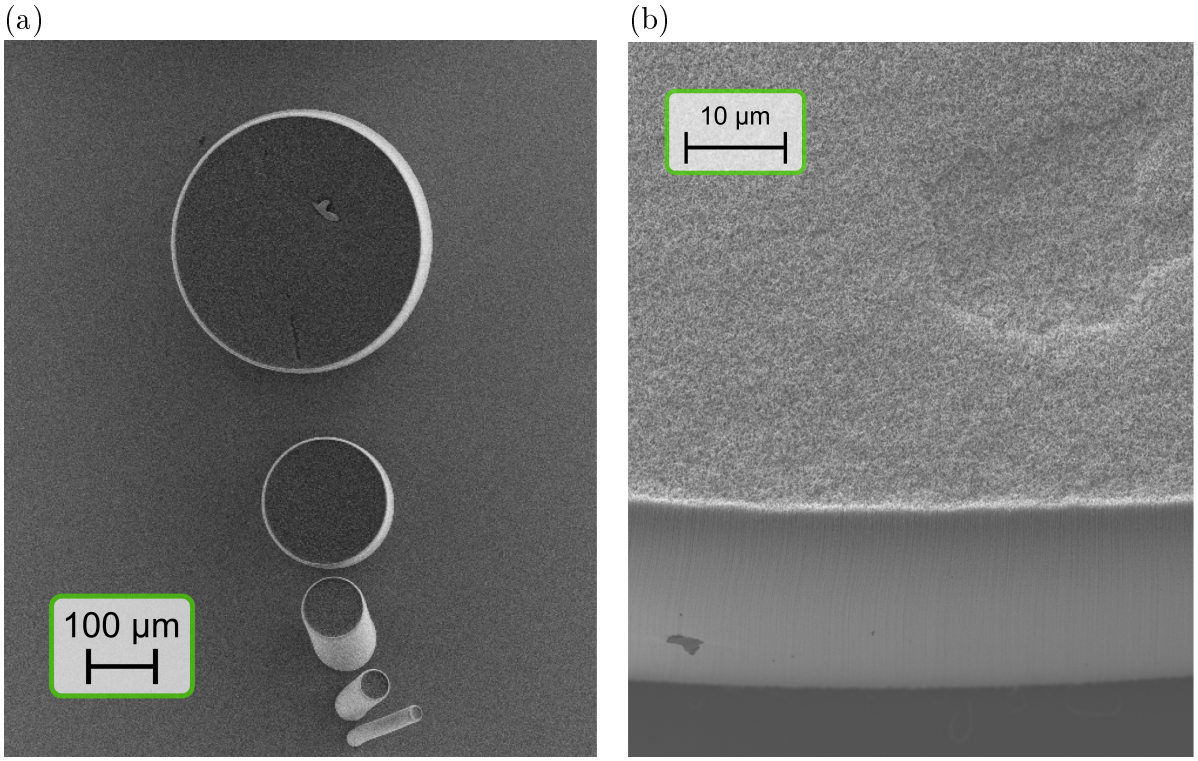

Figure 5.2: A scanning electron microscope image of (a) the smallest carbon nanotubes islands, from no 4 to 8 (top to bottom) and (b) the tilted sample showing cone and top defect in the carbon nano-tubes forest structure.

Quality check

The artefact was investigated under a confocal microscope. However, the high contrast nature of a specimen, reflective surface of wafer vs. perfectly black absorbent islands of VAMCNT, makes the specimen difficult to resolve under conventional routes. Therefore, a scanning electron microscope (SEM), the Zeiss Supra 40, has been used to investigate features.

In Figure 5.2 (a), one may observe features of directionality issue, where islands with numbers 6, 7 and 8 are leaning towards certain directions. The samples are manufactured

in a lithography process, thus the set of structures are made at once. The CNT forest is grown into a supportive photoresist layer negative to the desired pattern, which later after growing the CNT within the created moulds is removed. Due to the high aspect ratio in height:width of more than 2:1, the structure is not able to self support its vertically aligned structure. This observation suggests that these structures should be disregarded in later considerations.

The biggest CNT island structure, no. 4, in the Figure 5.2 (a), has on top some flake-like structure, which is believed to be a dirt or remaining photoresist. Similar can be found on structure no. 3, at the circle edge, as seen in Figure 5.2 (b). Also a small feature, a scratch, on bottom of the circle structure no. 4 can be found. This is probably a manufacturing defect, which and could be due to the uneven growth of the CNT forest (also seen ub circle structure no. 3, close to the edge in Figure 5.2 (b)). These defects when imaged with an IR camera and rotated 90° have not been found to be reproduced as temperature variation in the thermal images. Hence, it can be resolve that the emissivity at these points is not affected and a depth of such defects is to small in order to be measured by the camera.

The observed brighter ring around each of the circles suggests side walls seen from the top. It is assumed that the sample is fully perpendicular to the surface, even though the left side of each ring is thinner than right-hand side for both number 4 and 5; the small slight tilt of features is suggested. Nonetheless, the fact is that the measured top diameter of a circle is $95\% \pm 1\%$ in size of the designed diameter[1]. Hence, a tapered cone shape is predicted, rather than expected perfect cylindrical shaped, which seems to be reasonable loss of aspect ratio for such a high features ($200\,\mu m$) created in lithographic process. This is evident in Figure 5.2 (b) taken perpendicular to the surface of specimen. The characteristic lines of the vertically growing CNT forest also can be seen in Figure 5.2 (b).

[1]This measurements were taken with SEM, which was not calibrated to measure distance and also due to the large size for such type of an instrument the lowest magnification was used at which the fish-eye like distortion is present.

5.1.2 Setup

The artefact structure was placed underneath the infrared camera on a metal, thick, steel, black coated plate without a temperature control. Additionally, the optical paths between specimen and camera lens were shielded against external radiation. The specimen was placed flat on the much bigger metal plate allowing the good thermal conductor, such as silicon, to remain at constant temperature during measurements.
The room temperature measurement was carried out in the five separate acquisition steps in order to capture the whole sample set, since its size was larger than the field of view (FOV $3.2 \times 2.6\ mm$). The metal plate with artefact structure on top was moved along manually. During thermal characterisation the artefact structure was shielded against external radiation with black painted cardboard. Temperature was recorded at the each spot for the duration of 2 seconds and with the sampling rate of 100 Hz.

5.1.3 Results

Non-uniformities

To verify the non-uniformities of the artefact structure based on the silicon wafer with CNTs were measured based on the Calibration 1 range. The artefact was measured in three distinct positions; firstly in the middle, next 90 ° rotated and lastly displaced manually by a few millimetres. Prior to the measurement, the focus was adjusted to be in plane with the CNT surface. Figure 5.3 (a) is a thermograph showing the temperature distribution apparent at the instrument with respect to the middle of CNT artefact. Figure 5.3 (b), (c) and (d) shows the double-$4th$ [2] order polynomial surface fitting to improve representation of the data. The R-square for the fitting was nearly 40% and same as the adjusted R-square, so the fit was not over-fitted.

Because of the complexity of the route to acquire data, it is important to define this

[2]Surface composed of $4th$ order polynomial in x and y directions.

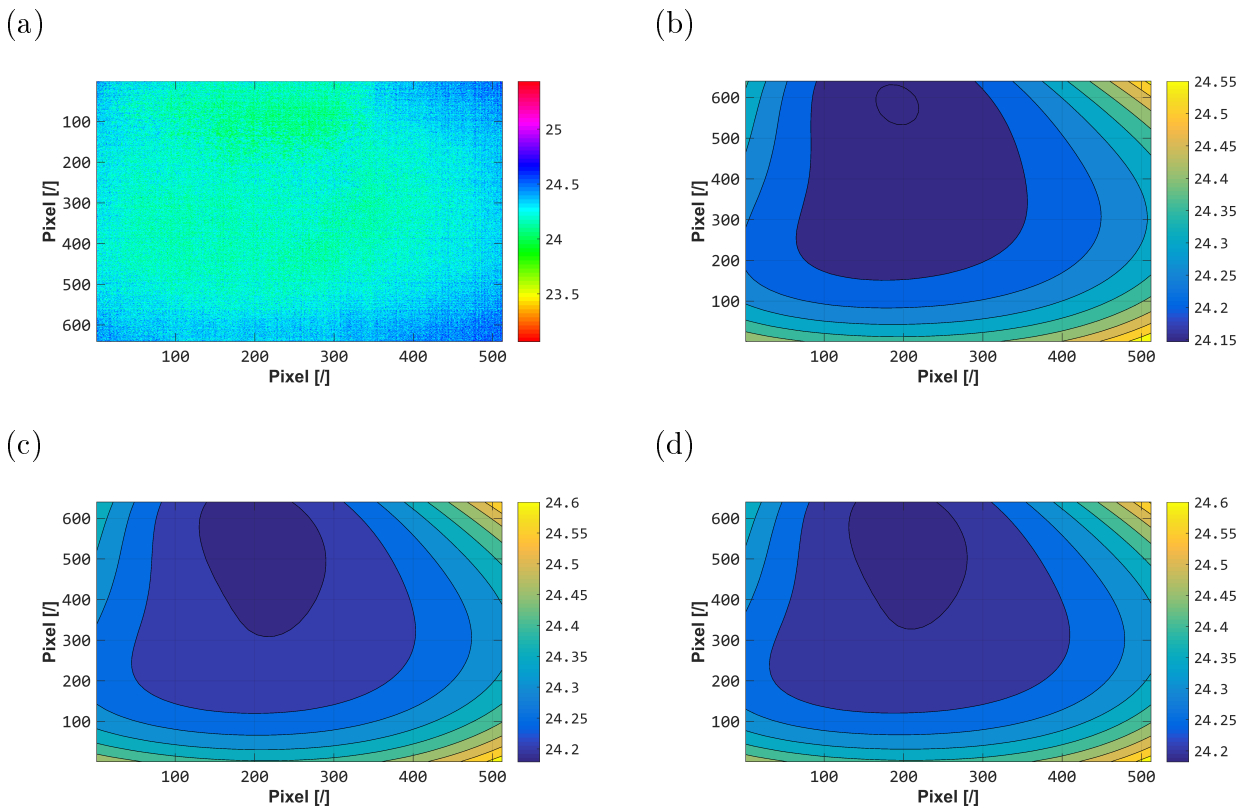

Figure 5.3: Presenting non-uniformity acquired at room temperature in the middle of carbon nanotubes artefact, where: (a) corresponding to the thermograph and double 4rd order polynomial surface fitted to these temperature data (b) for the middle position (c) 90° rotated from middle position and (d) when the artefact was displaced away from previous (rotated) location.

path. Hence starting from object under investigation, radiation is emitted form the surface →atmosphere →set of lenses and filters →sensor →electronic circuits →analogue to digital converter →built-in calibration →lastly to appear as final reading on the instrument. Therefore the action of rotation and displacement of the artefact in respect to initial positions would indicate the defects of the artefact surface, but, based on the result shown in Figure 5.3 (b), (c) and (d), such cannot be seen. This agrees with the findings of minor defects on the size-of-source effect CNT artefact structure shown in Figure 5.2, which clearly remained undetectable with the infrared camera. This confirms the excellent emissivity properties of the CNT artefact structure. The shapes of these three positions do not vary significantly. The values of each mean and standard deviation values were 24.24 ± 0.12 °C, 24.27 ± 0.12 °C and 24.27 ± 0.12 °C performed in order from normal to rotated and then to the displaced position, respectively.

The value of 0.12 °C for the acquired non-uniformity and shape, roughly matches with the value measured using NPL's calibration reference which was 0.09 °C at 30 °C. Hence two findings can be drawn; Firstly the acquired CNT non-uniformity was slightly high when comparing measurements and a drift of 0.03 °C was observed between the initial measurement and the other two, since it took slightly longer time in-between these steps. Neither the CNTs temperature was controlled nor stabilised, as it was considered to be a proof of concept rather than developed traceable artefact. Secondly this suggests that the non-uniformity indicated by the instrument is either due to the built-in calibration containing gains and offsets based on an imperfectly flat reference, and/or the optical path distortions e.g. spherical or coma aberration[3] (since the standard deviations per pixel for a time sequence shows the higher values closer to the edges of image in compare to middle). However further investigations are required to clearly confirm the origins of such distortions.

Size-of-source effect

Figure 5.4 shows the normalised temperature of individual VAMCNT islands, to the maximal temperature T_{max} of 25.38 °C. This was measured on the artefact structure no. 1, which covers the whole field of view of the IR camera. At the skewed artefact specimen, islands from 6 to 8, the temperature value drops to a level of around 2.5%, in relation to T_{max}. The tilt of these artefacts will introduce an out-of-focus image which brings in an extra error for these points (this is not included in the error bars). For the fit, a simple power function is used and extrapolated to a radius of 5 μm. Hence, the estimated drop for a reading from the feature corresponding to pixel size is around $\approx 4 \pm 2\%$ with coverage factor of k=1. The error bars of the measured values lay mostly within the boundaries of 1 σ of the prediction. In comparison with typical performance of IR imagers these boundaries are roughly within a range of 10–30% loss on temperature magnitude [149], therefore making the quantified performance of the infrared camera outstanding

[3]Coma or comatic aberration refers to some imperfections in optical system resulting in off-axis distortions [148].

low. Moreover, size-of-source effect on VAMCNT islands array has been performed at room temperature, despite the fact of size-of-source is temperature dependent [149], based on previously found similarity of low and high temperature for the Infratec camera (see Section 4.5.7). Hence on these findings the similar performance could be assumed at the temperatures around 200 °C, as it was found for room temperature measurement on VAMCNT specimen.

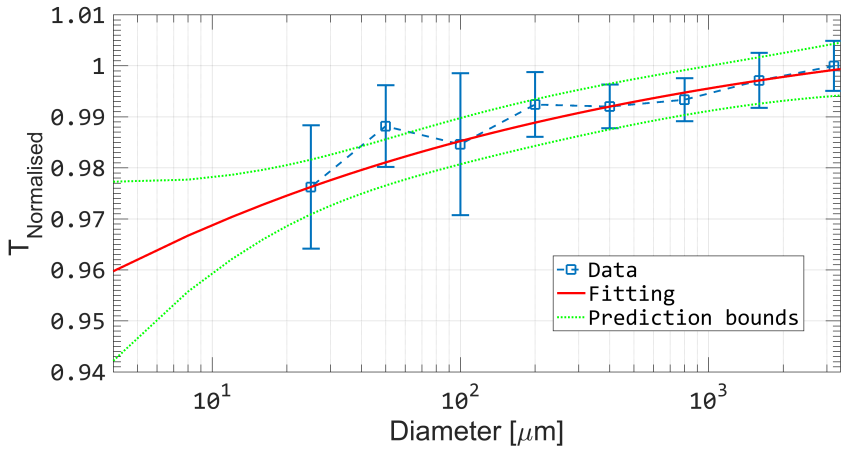

Figure 5.4: SSE represented as a function of source diameter and temperature (blue squares) normalised to the highest temperature (specimen artefact no. 1 $d = 3200\ \mu m$) and its fit (red solid line) with 1 σ (65%) bounds (dashed green lines). All results acquired at the room temperature.

5.2 The lowest observable ΔT based on Ohmic heating in thin film resistors

An infrared temperature change is assessed based on dissipated Ohmic heat measurements at steady state conditions. This section aims to find the lowest detectable temperature change on a thin film silicon resistor.

5.2.1 Motivation

In Section 4.5 sensitivity was characterised versus calibration standards. This allowed us to evaluate the performance of the instrument with negligible errors. Nevertheless, such an ideal case is not realistic, thus a resistive specimen was used to verify how low these temperature change can be observed. The aim of this section is to determine this lowest possible temperature change on a thin film silicone sample.

5.2.2 Artefact

The state-of-the-art calibration artefact; NT16-3K thermo test chip (NanoTest GmbH, Berlin) was used. It is a modular thermal characterisation test artefact, which dissipates power and measures temperature via a reference resistive temperature detector (RTD) integrated in plane with a heater. The test chip is composed of 9 cells in dimension of $3.2\,mm \times 3.2\,mm$ on the plane of 3×3 matrix, consisting of 10 heating rectangular resistors per cell. Each of the cells is separated with 100 μm scribe line allowing cut-out of individual cells. All the features, such as resistive heaters and resistor temperature detectors are deposited on the 675 μm silicon wafer. Heating of more than 60% of the chip area, see Figure 5.5 (a), is delivered by 30 resistors lines, each 480 Ω (each line resistor per cell is equal 160 $\Omega \times 3$ in series), connected in parallel configuration. This give an inverse cell resistance of $1/R = 10 \times 1/160\,\Omega \pm 5\%$ allowing an output power of more than 12 W per chip cell. The cell in the same row are configured in series ($R = 48\ \Omega$), but the three row are in parallel configuration, giving an overall R=16 Ω => $1/R = 3/48$ The embedded four-terminal sensing resistor temperature detectors are located in the middle of each cell see Figure 5.5 (b) with resistance of 3 $k\Omega \pm 1\%$ and sensitivity of 8 $\Omega\,K^{-1}$ (or 8 $mV\,K^{-1}$ at $1\,mA$ of constant current).

This artefact structure was packaged on a PCB chip and the electrical connections were made to the external terminals allowing an easy access for the soldering.

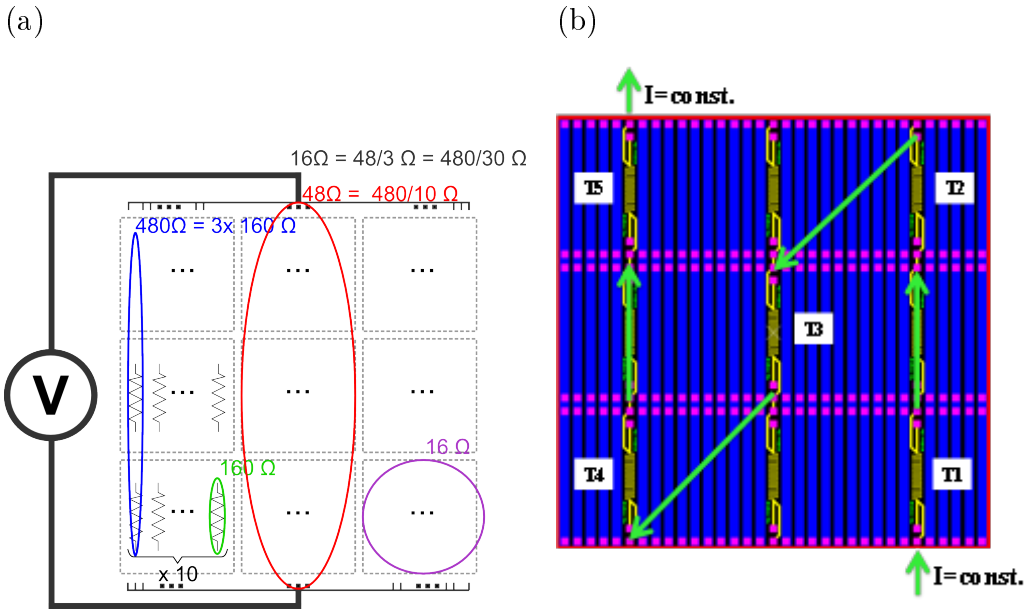

Figure 5.5: Nanotest artefact layout (a) Resistive heaters on the 3×3 cell matrix with denoted individual resistance and (b) Resistive temperature detectors marked on the chip and the connection of a sensing current.

5.2.3 Procedure and setup

The sample artefact chip was placed underneath the IR camera on a black painted metal plate and shielded against external radiation. The infrared surface temperature was manually initialised with the IRBIS3 professional®, after which the automated Matlab® script initialised measurement. A DC voltage step of 100 mV each is applied to the specimen via Agilent E3644a power supply in series with a Fluke 8842a Digital Multimeter (DMM) measured current supplied to the heater. Simultaneously a calibrated Keithly 2010 DMM was acquiring the resistance of a middle RTD (T3 in Figure 5.5) in a four-probe configuration. Prior to application of 60 second length of the DC voltage steps of 100 mV and 200 mV, a time of 5 second with zero-voltage was retained before the measurement has start.

5.2.4 Results and discussions

In the case of the infrared thermography, not only is the instrument performance a limiting factor in the lowest detectable temperature, but also the specimen is a vital part of the

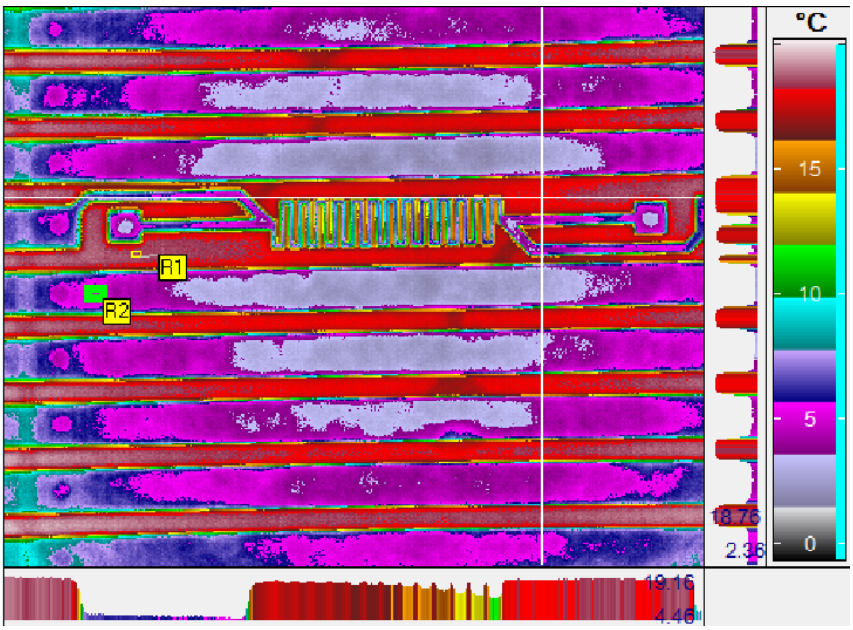

Figure 5.6: Infrared image of the NanoTest artefact (at room temperature) with highlighted high and low emissivity areas, depicted as $R1$ and $R2$ respectively. No current was applied to the specimen.

measurement. This can be clearly seen in Figure 5.6, where the thermograph corresponds to the measurement of the same specimen at a constant steady state temperature of ≈ 24.3 °C. Various temperatures can be read depending on the location of analysis. Thus when looking at the selected areas, one can see peaks for higher emissivity of area $R1$, corresponding to average $\approx 18.8\ °C$, and as low as ≈ 2.4 °C for lower emissivity area $R2$, corresponding to estimated emissivity of ≈ 0.78 and ≈ 0.36 respectively.

Due to the high reflectivity of platinum strips, the convex-like shape of decreasing temperature with a minimum in the middle can be observed. This pattern is a reflection of a cooled down to 78 K sensor chamber located inside the IR camera. This is a disadvantage when measuring a temperature on a reflective specimen, where additional contribution would need to be considered. Furthermore, the difference in emissivity affects the magnitude of detected ΔT and the ramp slopes of acquired apparent temperatures. The magnitudes of high and low emissivity areas were 26 mK and 14 mK respectively, can be seen in Figure 5.7. The power dissipated through the heaters due to its design is expected to be distributed uniformly across the surface. Especially at such a short length between the measurement areas. Moreover in the lower emissivity area the increased noise of the

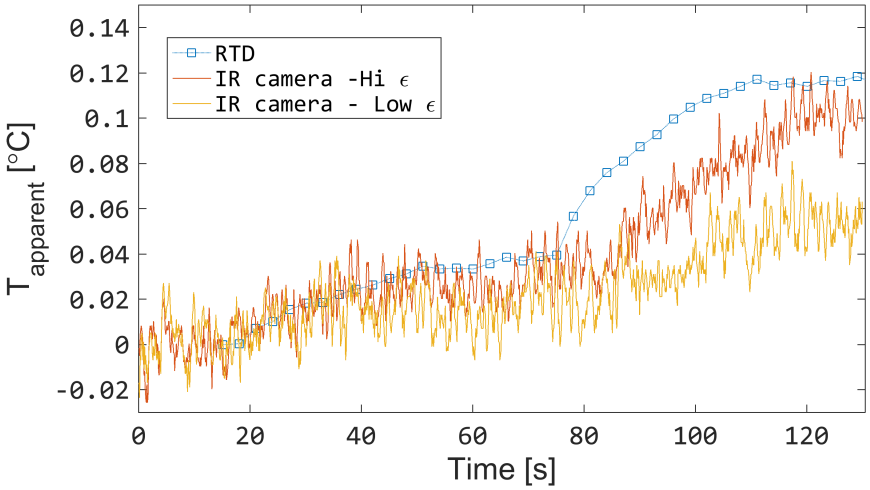

Figure 5.7: Effect of the emissivity on the sensitivity of the measurement shown as apparent temperature as a function of time. The blue line (with square markers) represents temperature on resistive temperature detector (RTD) $T3$ on the NanoTest chip and red and orange lines shows surface temperature acquired at the areas $R1$ and $R2$ corresponding to high and low emissivity areas, respectively.

measurement (equal to 22 mK), can be seen in comparison with higher emissivity area (equal to 19 mK).

In Figure 5.8 a power of 1 mW dissipated at one out of nine cells in an area of $\approx 10\ mm^2$ with more than 20 mK difference and with a significant standard deviation close to the detected absolute value. This presents the limits of a minimum detectable power dissipation of a mW region in a micro-scale artefact. This closely agrees with the independently detected resistance change measured at RTD with ΔT of 33 mK and 26 mK for the infrared camera. Once the surface emissivity of specimen is known, the apparent temperature to the infrared camera can be compensated to a true value, however this increase the errors as well. To emphasise, it is more convenient to use the temperature difference as in this way the systematic errors cancel themselves out, but a slightly higher noise will remain. When the dynamic response of the power application is compared with respect to measured temperatures the difference can be noticed, see Figure 5.8. It has to be acknowledged that the electric measurements of applied power and temperature change on RTD, was not synchronised with the IR acquisition. Nonetheless, with such a low power, heat will take longer to propagate through the specimen. Thus, the measured

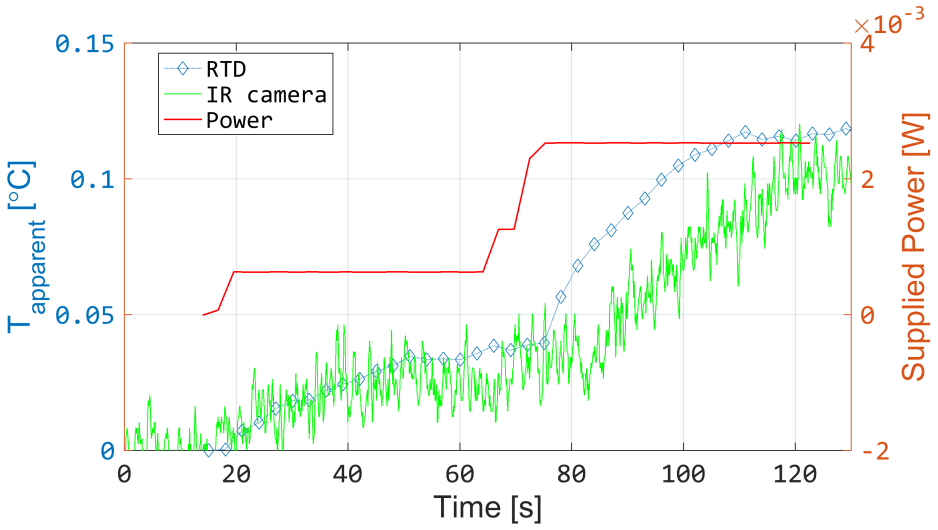

Figure 5.8: The room temperature independently measured (left axis) temperature $T_{apparent}$ via infrared camera (on the high emissivity area) and embedded resistive temperature detector (RTD) T3, and (right axis) measured power supplied to the heater as a function of time.

temperature with the RTD shows a time lag compared to applied power. The specimen is deposited on a silicon wafer based integrated circuits and later cut and packaged on the PCB board. This would further explain an additional delay in IR measurement, which potentially is faster than any contact sensor (no thermal mass). Hence it suggests that the non-contact temperature is acquired through the silicon wafer, which is transparent for the operating range of wavelengths and from the surface of the PCB board, rather than the wafer surface as for the RTD.

To extract exact values of the true temperature and account for the transient processes more detailed information about sample packaging on PCB e.g. spacing and materials characteristics, would be required to be integrated in a final thermal model.

5.3 Assessment of ΔT in the setup

A bulk resistor was employed to verify the infrared temperature change reading at normal conditions, at which an EC material would be assessed for temperature change ΔT.

5.3.1 Motivation

In section 4.4, the calibration was performed using current infrared ITS-90 standard, which allows us to address the accuracy of absolute temperatures. However, evidence of temperature change correctness in the specimen environment is required. Due to the lack of standardised methods, the Ohmic heat in commercial resistors has been adopted for a verification procedure.

5.3.2 Artefact

For the artefact, a resistive specimen has been chosen, so that it can mimic the approximate scenario of a typical EC sample with side electrodes, comparable sizes and made of ceramic, so the materials' thermal properties like heat capacity, thermal conductivity, thermal mass could be comparable. A standard surface mount resistor Bourns CHF2010xNP series (RS 692-7677) with the resistance of $100\,\Omega$ was used as a reference sample. The sample comes in a surface mount packaging technology (case 2010, size of $5.3 \times 2.7 \times 1.2\ mm$). The thick film resistor is built on an AlN substrate and terminated on both ends with NiAu electrodes. An additional third separated ground electrode is placed on the bottom of the resistor. This bottom metallic surface was used for mounting a reference thermocouple; no electrical connection has been made.

Characterisation

The surface emissivity of the sample was estimated to be $\epsilon \approx 0.8$, based on a measurement of surface temperature measured via a T-type TC room temperature (the specimen is not expected to change its emissivity during investigation).
For the temperature ΔT change of the artefact, two additional parameters have to be characterised. Firstly, the resistance-temperature coefficient, which is $\alpha = 0.0308\ \Omega\,°C^{-1}$ (measured inside a furnace with a digital multimeter using a 4 probe technique; see Appendix C for more details).

Secondly, the heat capacity (acquired with the Netzsch DSC 200 F3 Maia, in the temperature range 25–200 °C). A simple power fit was used to utilise this heat capacity value at required temperatures for further considerations.

5.3.3 Setup and procedure

Figure 5.9 shows the schematic diagram of a setup arrangement. The sample was placed in between the spring-loaded electrodes of the electrocaloric sample holder. The additional thin 0.075 mm K-type thermocouple (RS 397-1589) was soldered underneath the specimen to the third bottom electrode located on the side facing the hot stage. The sample was secured with the thermally conductive paste (RS components 217-3835) and isolated with the thermally isolating silicone foam to prevent excessive heating of the IR camera lens. To produce the temperature change on the resistive sample a current was applied in a

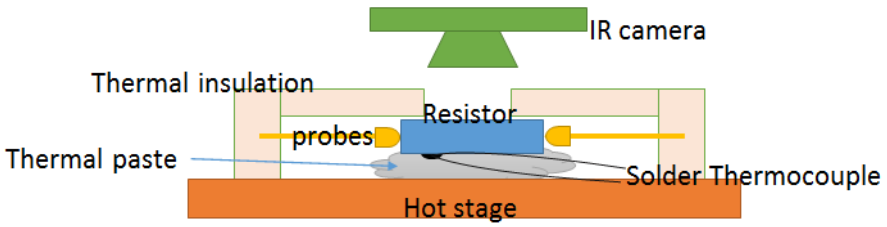

Figure 5.9: Setup diagram for bulk resistor temperature change verification (graph not in scale).

step with the Agilent E3646A DC power source. Several voltage steps from 0 V to 4 V in 0.4 V steps were maintained for duration of 90 s each, see diagram in Figure 5.10. This procedure aimed to achieve the necessary DC conditions, so that the final temperature and resistance have reached the requested saturated steady state value before the final quantities are extracted.

Two precision digital multimeters (Keithly 2010 and a Fluke 8846A) were used to measure the current and voltage across the sample respectively. The voltage measurement was carried out with standard banana cables attached to a thin $\phi = 150$ μm tinned copper wires which were soldered to the end of the test probes. The cables resistance was measured to be around 4 Ω which contributes to a $< 5\%$ drop in the voltage measurement

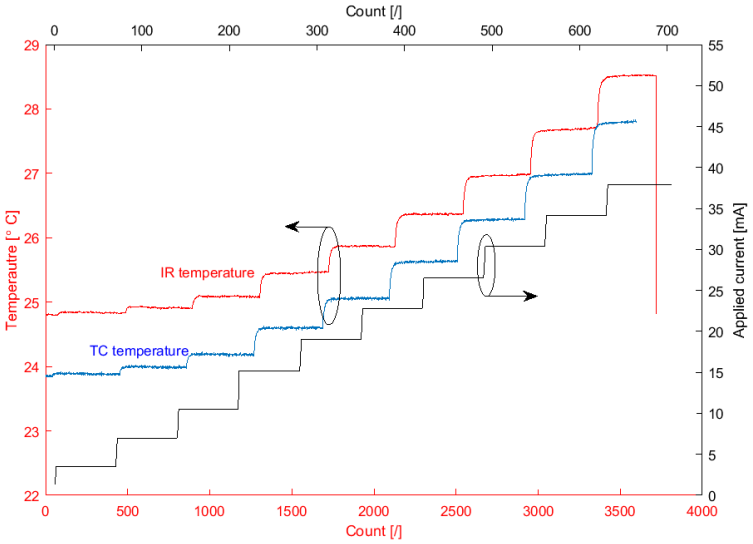

Figure 5.10: Example of temperature readings based on measurement procedure acquired at 25 °C, steps of detected temperature (blue and red lines from thermocouple and IR camera, respectively, left and bottom axis) and current steps (black line, right and top axis).

across the 100 Ω specimen.

The experimental procedure was repeated for different temperatures delivered by the hot stage. The hot stage in these experiments was set to the constant power, operating mode in order to reduce the unnecessary PID controller contribution to compensate the external temperature changes, during the long measurement periods.

5.3.4 Results and discussions

Measurements have been performed on selected temperatures from around room temperature up to 160 °C. Additionally graphs are presented in Appendix C.

Error bars

The error bars in following Figures 5.11 and 5.12 denotes the standard error of ± 1.5 °C for a K-type thermocouple and the standard deviation for IR measurement, where the uncertainty for this sample would be ± 0.14 °C ($k = 1$). Error bars for temperature estimated from resistance are based on a combination of standard deviations from voltage,

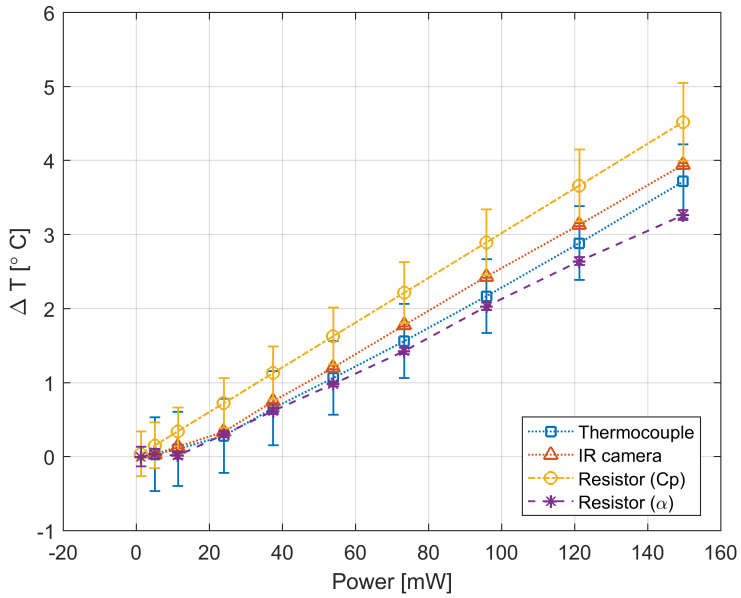

Figure 5.11: Measurement of ΔT at room temperature by means of; thermocouple (blue squares), infrared camera (red triangles), resistance via heat capacity (orange circles) and resistance-temperature coefficient α (violet stars).

current and alpha coefficient (partial derivative method was used [118]). The other type of temperature is evaluated based on the heat capacity and the power added to the resistor.

Measurements performed close to room temperature

Close to room temperature, as seen in Figure 5.11, all the measured values merge together with fairly good agreement. Especially close agreement has been found at the low power dissipation levels. The temperature acquired by the IR camera seems to be slightly higher than the temperature measured by thermocouple, particularly after passing the level of $40\,mW$. This can be explained by the different positions at the specimen surface investigated by the TC and the IR camera.

The thermocouple measured the average temperature of the surface under test and the interface semi-liquid (thermal paste) around the sensor.
In the case of using the infrared camera, the temperature is investigated at the non-disturbed temperature field, that would comply with the contact temperature measurement theory (see section 3.2). However in this case the surface is in contact with the atmosphere

in a solid-gas (air) interface. For clarification see Figure 5.9 presenting theexperimental setup. The temperature of specimen recorded with a resistance via heat capacity indicates slightly lower ΔT values, which still fits in the error bars of the TC measurement.

Higher temperatures

When moving into to the higher temperatures of the surroundings, these trends remain. At around 100 °C the difference of temperature reading between the TC and IR camera is less apparent even at higher power rates where the current was $> 100\ mA$. When investigating temperatures above 120 °C the trend inverts and the TC is now showing higher values in the same comparison. Based on that observation one may conclude that above 100 °C the convective losses become more dominant. Such loss would first introduce a temperature gradient across a sample and secondly differentiate the surface/atmosphere interfaces for each type of measurements, especially at higher levels of temperature. A drop of $\approx 2 \times 10^3\ K\,m^{-1}$ has been detected between the hot stage (measured with embedded thermocouple) and the sample at 160 °C. Similarly, the drop of temperature between the sample and the infrared camera lens [4] was equal to $\approx 5 \times 10^3\ K\,m^{-1}$.

Assuming that the temperature gradient at these distances is uniform and linear at each location, this will imply an existence of thermal resistance at each interface and a temperature gradient across the sample itself as a result.

To cross check, an additional argument could be suggested with a simple resistor. The resistance vs. temperature calibration was performed by two different means: on top of a hot plate and inside an oven. The slope differ depending on the heating method. The measurement in the oven will reduce the effect of the heat leakage to the electrical connection, since a significant part of the thin wires were close to isothermal conditions. Therefore, such a difference between the acquired temperature values suggests two different origins for error. Firstly, the surface temperature measurement and secondly existence of thermal gradient across the sample placed on the hotplate, including the convective cooling.

[4] An additional K-type thermocouple was attached to the cameras lens.

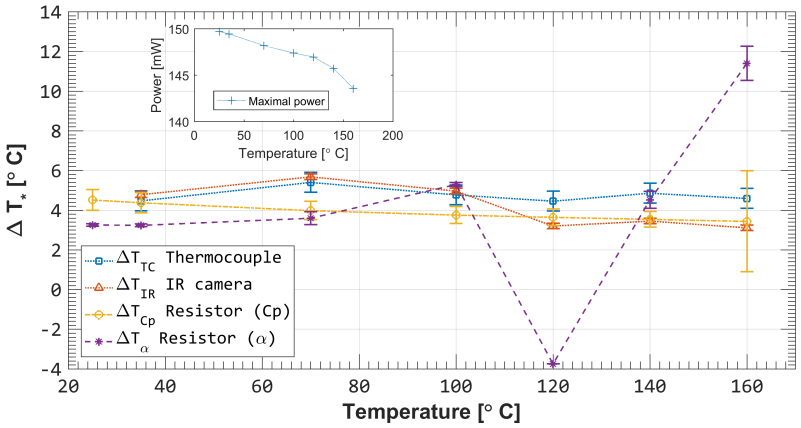

Figure 5.12: 'Thermodynamic' and surface temperature changes ΔT_* (where '*' corresponds to relevant measurement technique see legend) measured for a resistor as a function of temperature acquired for the maximal power of 150 mW. The inset presents the maximal power applied to the resistor under the test as a function of temperature.

Resistor 'thermodynamic' temperature changes

A commercial resistor was calibrated so a 'thermodynamic' temperature[5] change can be obtained using the α temperature coefficient and the Cp heat capacity. Such ΔT corresponds to the thermodynamic temperature change; averaged value over the specimen's volume, not the temperature of its surface. The specimens were chosen, due to similarities to a EC samples and chosen as a source of a controlled heat and also because RTDs are a robust solution for the temperature measurements.

Typically RTDs are active sensors made of a metal resistors with a resistance of 100 Ω. THe precision resistance measurements were made under small current of 1 mA, so the errors can be reduced e.g. reduced errors due to self heating. However, the steps of current were applied to the resistor in order to create temperature changes, and most likely this current will affect the accuracy of the sensitive resistance measurements.

The 'thermodynamic' temperature change based on the Cp dependences on the applied power ($P = V \cdot I$) and this ΔT is less sensitive to errors in comparison with resistance

[5]The thermodynamic temperature term is used in order to differentiate temperature measurement of the specimen's surface temperature and the average temperature value of a body established via theoretical calculations based on the whole volume of a specimen, rather than a specific location on a specimen.

measurements ($R = V \cdot I^{-1}$), where small changes of measured current resulted in significant variation of resistance. In Figure 5.12 the ΔT_{α} displays anomalous results for two temperatures of 120 °C and 160 °C, which are related to errors in resistance measurements. The ΔT_{Cp} at 25 °C is equal to ≈ 4.5 °C and it is consistently reduced by 1 °C towards ≈ 160 °C. The ΔT_{Cp} follows the same trend of the measured power, shown in the inset of Figure 5.12. This is a consequence of the measurement procedure, where the constant voltage steps have been applied to the resistor which resistance decreased with the temperature, hence the reduction of dissipated power with an increase of temperature. The 'thermodynamic' values based on Cp, the ΔT_{Cp} in comparison follow the same trend as the surface temperatures ΔT_{TC} and ΔT_{IR}. Most of the values are closely located and either close or within the error bars. The trends of the ΔT_{IR} and ΔT_{TC}, up to 100 °C displays close values of each other and then further when the convective loss becomes more dominant, the magnitudes differs.

5.4 Conclusions

5.4.1 Optical performance – the non-uniformity and size-of-source effect

The measurement of thermal uniformity on the high emissivity artefact was performed. A non-uniformity of around 0.12 °C was detected on the CNT specimen flat surface artefact. The origins of the non-uniformity may be of various sources, from built-in calibration to dark pixels, non-uniform distribution of the sensor temperature or uncompensated lens aberrations. In order to make a valid compensation, the further knowledge of the IR imager, its construction and individual components would be necessary.

The preliminary micro-scale size-of-source effect was then investigated. When investigating a test object of size around 20 μm, the loss in temperature reading down to approximately $3 \pm 1\%$ can be encountered. Moreover, based on the fit of results, extrapolated size close to size of pixel ($5\ \mu m \times 5\ \mu m$) value of such temperature reading can go down

to $\approx 4 \pm 2\%$. This result improves resolution of size-of-source effect in compared with the standard measurement achieved previously at NPL, which has shown drop of 5% in relative temperature value at the smallest aperture size of 0.75 mm in contrast with the largest aperture (see section 4.5.7). In the same time proves the feasibility of flat CNT artefact to gain higher resolution (lower sizes of the black body reference artefact) for this kind of measurements at the micro-scale.

5.4.2 Lowest temperature change

The qualitative measurements of the minimum temperature difference was performed. The current setup allows to detect small dissipated power of 1 mW on a given artefact resulting in detection of as small as $\approx$ 25 mK with noise of around 20 mK ($k = 1$) corresponding to approximately value of 30 mK temperature change measured independently of a resistive temperature detector on the grey body. Similarly, the temperature change as small as ≈ 14 mK was possible to be detected based on a reading from the low emissivity region on the artefact, however with slightly higher noise of > 20 mK.

5.4.3 Assessment of the setup

The temperature change measured by the thermocouple method ΔT_{TC} and the ΔT_R resistor verifies correctness of temperature change readings with ΔT_{IR} infrared camera. It was noted that the surface temperature is not the same as the true temperature inside a solid body.

Because of that, the atmosphere around a specimen affects the temperature measurement, especially at higher temperatures $> 100\,^{\circ}\mathrm{C}$. Extra precaution has to be taken at these higher temperature regions with the current setup, as both convective and radiative loss are more apparent there. As the nature of instantaneousness of ECE the entropy change causing a change in temperature is present only during the change of the electric field. A pulse delivery of power, rather than continuous supply of dissipative power, should be

applied during this type of characterisation. The time length and the heat fluxes were examined in this calibration and are most likely not being a problem for EC materials since their levels of power are below continuous power of 100 mW over 100 s periods. This makes this technique more favourable than the case of steady-state characterisation. The electrocaloric measurements are intended to be performed at adiabatic conditions, which are difficult to achieve in reality. Hence, the ECE measurements performed by IR camera and with a hot plate-like stage will experience the thermal gradient on a sample under test and this shall be considered. The steady state calibration discussed above is difficult to directly compare with electrocaloric measurements. Once more, the thermal gradient might bring unfavourable effects such as more pronounced underestimation of ECE and additional uncertainty to the real temperature of the sample which is important to when determine a peak performance in the case of high temperature ($>$ 100 °C) ferroelectric phase transition materials.

Chapter 6

Inter-lab comparison

Currently more than 80% of the electrocaloric (EC) research are based on indirect estimation method, rather than direct EC measurements [22]. Few comparisons between various measurement techniques have been made [67, 110], however a lack of standardised measurement methods has been an inspiration to perform a more detailed study seen in this thesis.
An ceramic sample ($Ba_{0.65}Sr_{0.35}TiO_3$) was measured by the means of the infrared camera and two kinds of heat flux differential scanning calorimeters (DSCs). One at Imperial College London (ICL) is a pan heat flux calorimeter and one which is a tube flux calorimeter at Laboratoire national d'essais (LNE) France.

6.1 Motivation

The aim is to perform the preliminary comparison study of electrocaloric effect, based on different techniques and various approaches in measurements. This should allow us to identify possible errors encountered during the measurement process.

6.2 Calorimetric equipment

ICL

To carry on the experimental work, a standard E-type thermocouple based heat flux pan differential scanning calorimeter (Netzsch DSC 200 F3) was adapted for the electrocaloric measurements. To allow high voltage connection, thin platinum wires are attached from the top by electrical probe and grounded by the bottom silver electrode in a pan. For more details please see schematic diagram in Figure 3.4, section 3.3.2 and in Ref. [120].

LNE

In French National Measurement Institute laboratory, a tube flux differential scanning calorimeter was employed (Setaram DSC111). Figure 6.1 shows schematic diagram of a calvet (tube three dimensional) calorimeter comprised of a temperature controlled furnace and digital multimeter measuring differential signal with supporting equipment, such as computer controlled signal generator, high voltage amplifier allowing the electrocaloric measurements. For this setup, a high voltage leads were placed through the sides of a tube furnace. This equipment is usually adopted, when either a low uncertainty on the specific heat measurement or a low specific heat variation of energy in substance has to be detected. The performance of such a sensitive calorimeter was achieved by the two thermopiles, constituted of 120 thermocouples around each cylindrical measurement chamber, see Figure 6.1. Isothermal conditions were possible due to the double alumina tube furnace built in a silver block.

Differences between calorimeters – ICL vs. LNE

The ICL and the LNE setups differs in construction, hence a different mechanism of acquisition. The DSC at ICL used 2-dimensional pan sensor measuring most of the heat via thermal conduction, where rest of it is dissipated to walls and covers. The LNE

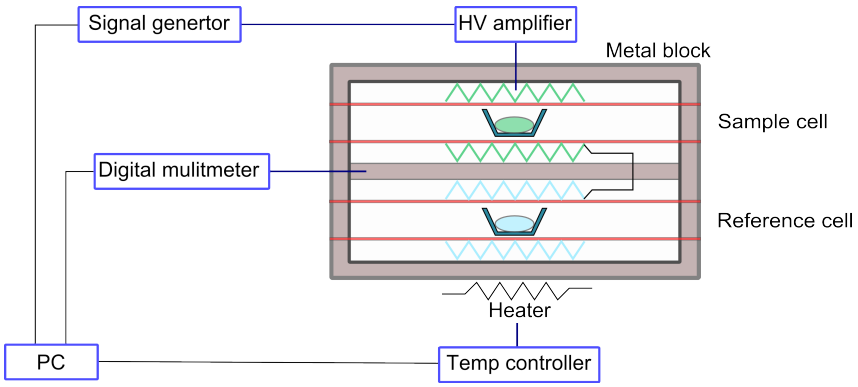

Figure 6.1: Schematic diagram of a calvet differential scanning calorimeter adapted for electrocaloric measturement. Schematic not to scale.

setup employs the 3-dimensional cylindrical thermopile sensor (see Figure 6.1) measuring not only conducted heat via the crucible but also that dissipated. Thus the estimated efficiency of a heat measurement in the 2D sensor can reach between 50–70% of total released heat. The 3D Calvet type sensor can provide detection of more than 90% of heat transferred to the sensor, allowing low calibration uncertainties, hence better measurement precision [150] is expected.

6.3 Polycrystalline BST ceramic

The specimen of $Ba_{0.65}Sr_{0.35}TiO_3$ was produced solid state method by a means of calcining and sintering process and is described elsewhere [151]. The sample had a cylindrical shape of 5 mm in diameter and 1.1 mm in thickness. The density of a sample was 5.37 $g\,cm^{-3}$ and measured by Archimedes technique (94% of theoretical density). For electrodes, flat faces of the sample were painted with silver paint (SCP, Electrolube).

6.3.1 Dielectric properties

Figure 6.2 shows relative permittivity acquired inside the ICL calorimeter with HP LCR meter 4263B, for the span of approximately -190–180 °C. Data were acquired upon heating with a ramp rate of 1 $K\,min^{-1}$ and with an AC signal of 100 kHz with amplitude

of 500 mV. Furthermore, three peaks of relative permittivity correspond to atomic movement displacive (crystal phase transition) in nature, from rombohedral to orthorhombic around 174 K, to tetragonal structure at 222.2 K and lastly is the Curie temperature of 292.3 K corresponding to tetragonal to cubic phase transition. This allows us to find the T_c where the ECE is expected to be the largest.

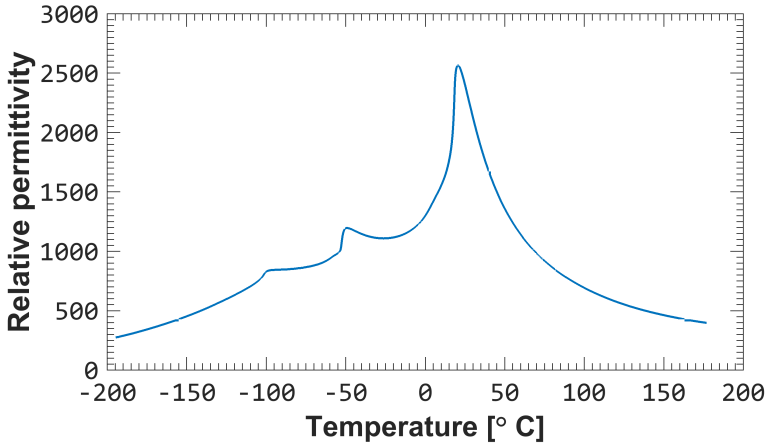

Figure 6.2: Relative permittivity as a function of temperature for BST.

6.3.2 Polarisation Electric field loops

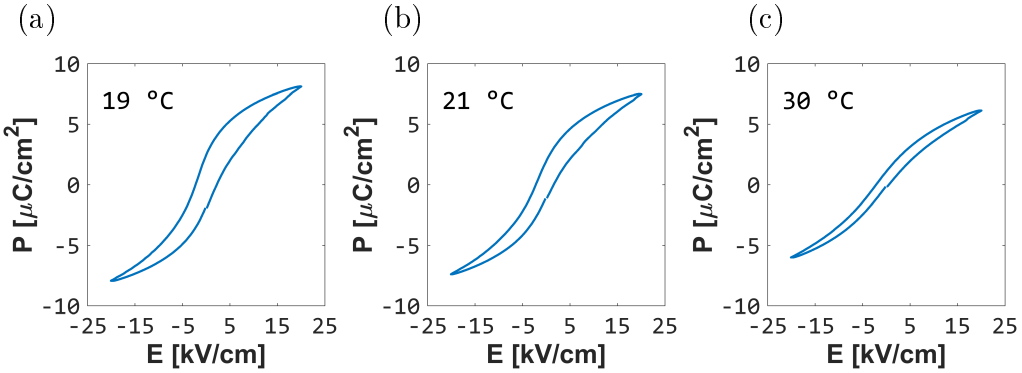

Figure 6.3: Selected representative P–E loops of the BST specimen, (a) before T_C (b) at the vicinity of T_C and (c) after T_C (acquired at AC frequency of 20 Hz).

Selected P–E loops of BST sample are presented at Figure 6.3. The ferroelectric tester employed for these measurements was a Precision LC/High Volatge interface with integrated

external amplifier (Trek 609B) in combination with the DSC located at ICL. The hysteresis of polarsiation proves the ferroelectric nature of the specimen.

6.3.3 Leakage current

This property defines resistive loss during an electrocaloric cycle and has been acquired at two laboratories, namely ICL and NPL. All values are in reasonable agreement with a very low leakage current of usually $< 10\ nA$. Figure 6.4 (a) shows leakage current as a function of electric field acquired at the room temperature. These quite scattered points do not present any clear trend, however the subtle rise of leakage current would be expected with an increase of electric field. Figure 6.4 (b) shows leakage current as a function of temperature. The independently measured leakage currents at ICL and NPL display a comparable low magnitude in a range of nA. Based on the knowledge of testing samples with similar composition, but slightly higher phase transition temperature, the substantial increase of field above 35 $kV\,cm^{-1}$ introduces a loss significant enough to reduce the measured heat. However, such point of imbalance was achieved for a leakage current 2 orders of magnitude higher than the one detected at the operating ranges of interest.

(a) (b)

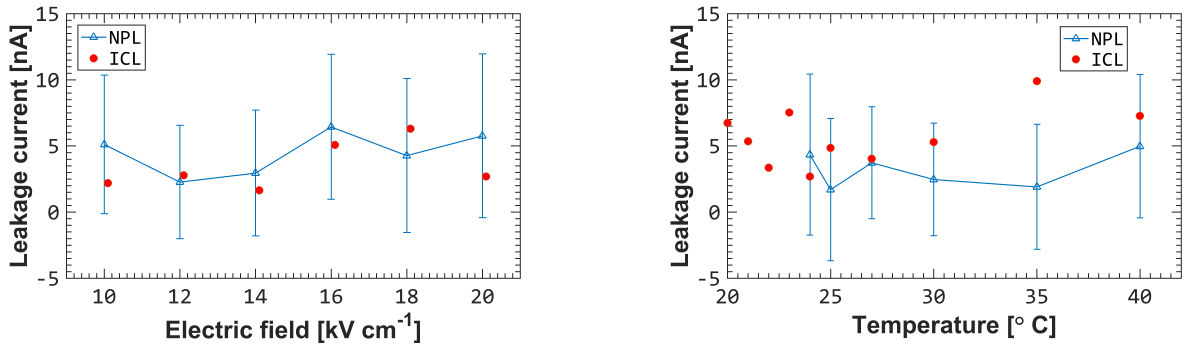

Figure 6.4: Leakage current of BST acquired during direct measurement at NPL (blue triangles) and at ICL (red dots) as a function (a) function of electric field measured at 23 °C and (b) temperature for the highest applied electric field of 20 $kV\,cm^{-1}$.

6.3.4 Heat capacity

The zero electric field heat capacities ($Cp_{E=0}$) are shown in Figure 6.5. This property has been measured independently at the ICL and LNE. Data acquired at ICL (blue circles) show an initial decline of the heat capacity after the sharp first phase order transition. Whereas the LNE measurement (red squares) do not possess this clear peak. The error bars correspond to the overall combined relative uncertainty ($k = 2$), which is around 3.2%, without consideration of temperature effect due to narrow span of interest. The standard deviation of Cp values from 18 °C to 65 °C is equal to 4.8 $J\,kg^{-1}\,K^{-1}$ and mean value is $\approx$ 483.9 $J\,kg^{-1}\,K^{-1}$, where the uncertainty is equal to approximately to $\pm$15.6 $J\,kg^{-1}\,K^{-1}$. Thus, based on a linear fit, the Cp at 0 field was estimated to be 485.6 $J\,kg^{-1}\,K^{-1}$ and is used for further calculations.

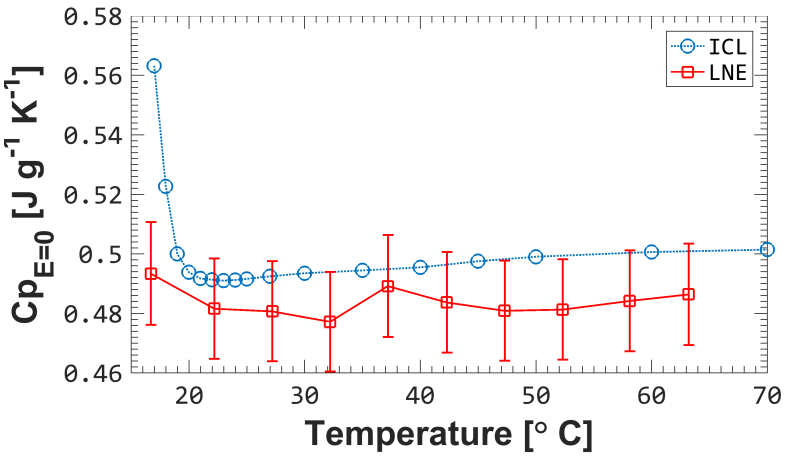

Figure 6.5: Specific heat capacity, Cp, as a function temperature measured at LNE (red squares) and ICL (blue circles).

6.3.5 Indirect estimation of ECEs

Figure 6.6 presents the estimated values of electrocaloric effect based on P–E loops measurements presented in the beginning of this section. The first-order transition is known to be not fully thermodynamically reversible [140], due to the considerable latent heat and therefore a thermal hysteresis, which are excluded when using indirect method

approach (Section 2.3).

Scattered points are a consequence of the coarse and uneven spacing between the temperatures and low number of measurements points for P–E measurement.

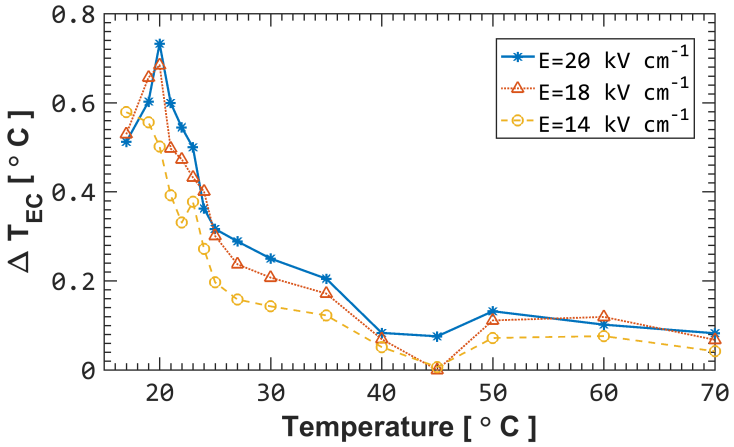

Figure 6.6: Indirect estimation of ECE based on Maxwell relations for selected electric fields.

6.4 Measurement Procedures

For all cases in this experimental work, a DC voltage step is applied to the EC specimen (see Figure 4.10 in section 4.5.1). A sufficiently long DC voltage step is chosen to cover the thermal relaxation of a sample/environment; time of the DC voltage was remained so the initial temperature of the sample (before application of the pulse) and final temperature had the closest value.

6.4.1 Differential scanning calorimeters

At ICL the calorimeter is combined with a ferroelectric tester (Radiant Precision LC/High Voltage Interface) to acquire the ferroelectric qualities e.g. P–E loops, leakage current etc. The sample performance is evaluated in the sequenced manner for each temperature step. Firstly the leakage current, followed by the double bipolar P–E loop at given field

and then finally the three times direct DC step. The ramp rate is not controlled, however based on the small capacitance ($< 10\ nC$), for given fields a full slew rate is achieved and should be faster than 1 ms. Due to the likelihood of breakdown, which is not commonly reported with the electrocaloric samples, the P–E loop and leakage current measurement is repeated afterwards as an experimental cross check. The sample was placed inside of a crucible immersed with silicon oil (47V 350, VWR chemical) to facilitate better heat transfer and to avoid the dielectric breakdown.

However at LNE due to the lack of a ferroelectric tester, a high voltage power supply, the Stanford PS375, is used instead. The on and off step voltage pulse is applied without controlling the pulses ramps. This was solely dependent on the internal circuitry of the power source, the time constant RC in combination with a sample ($RC < 1\ \mu s$) was much faster then slew rate. In this case, based on the slew rate, the rise time can be estimated around 150 ms.

In both cases, a two calibration according to the standard procedure [121, and ref. therein] has been performed preceding the electrocaloric measurements. Firstly the temperature scale calibration, via fusion temperatures of some pure reference metals has been used to calibrate the temperature scale, namely gallium 29.76 °C, indium 156.60 °C, tin 231.41 °C, bismuth 271.41 °C and lead 327.47 °C. In case of the ICL setup only the In and Sb references were used for that purpose.

Secondly the three steps for baseline correction are made by acquisition of empty crucible, reference and finally sample curves. Wires attached to the specimen have to be considered, since substantial errors in heat measurement (heat gains/losses) can be found during electrocaloric cycle. At LNE heat leaks of platinum wires attached to the specimen were measured and such correction of additional baseline was made. However, at ICL an electrically shorted BST sample (linear I–V curve; resistor) was used to calibrate losses based on quantified Joule heating in reference to detected heat with the DSC.

6.4.2 Infrared thermography

Prior to the direct measurement of the EC response at NPL, the triple bipolar P–E loop[1] measurement is carried out. During application of a DC voltage step, a current response is acquired with the Aixacct system, from which a leakage current is extracted.
In the infrared system ΔT_{IR} is acquired via the differential measurement of apparent temperature during controlled action of electric field. However, to establish the absolute value of temperature the specimen, a prior reading was taken from a hot plate's thermocouple located near to the specimen.

6.5 Results and Discussion

The $Ba_{0.65}Sr_{0.35}TiO_3$ sample phase transition is expected to occur around room temperature, as was confirmed through the relative permittivity (see Section 6.3.1). Thus the specimen has been investigated for a temperature span 15–40 °C for DSC and 24–40 °C with IR camera, due to system limitation (heating action only).

6.5.1 Electrocaloric heat energy

Figure 6.7 presents results from two laboratories for a specific electrocaloric heat as $J\,g^{-1}$ taken upon cooling. The values match well within uncertainties in case of LNE and standard errors for ICL. Subtle magnitude difference are noticeable especially for higher electrical fields. The values obtained at LNE the are around 10% greater i.e. at the peak value of EC heat $Q_{EC} = 0.2330\ J\,g^{-1}$ at 23.9 °C in comparison to ICL, where the $Q_{EC} = 0.2098\ J\,g^{-1}$ at 24.00 °C.
The expected peaks of a phase transition, close to which the ECE is the largest, are located around room temperature($T_c \approx 19.15$;°C). In order to evaluate the exact absolute temperature calibration in between calorimeters based on EC peak, more points are

[1] A low frequency of P–E loops was chosen and during direct measurement equivalent slew rate of step pulse is chosen. Allows comparison of indirect and direct results.

required. The peak of ΔQ_{EC} lies within the expanded uncertainty of the LNE calorimeter of 0.8 °C ($k = 2$) and the error of ICL equipment is unknown.

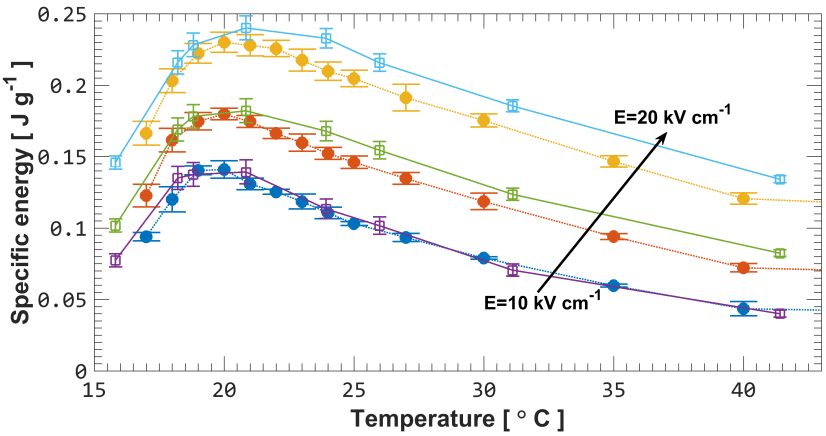

Figure 6.7: Measured value of electrocaloric heat specific energy measured at ICL (dotted lines and circles) and LNE (lines and squares) for selected electric fields.

According to the construction differences of DSCs, the results obtained by the DSC in LNE have slightly higher values of electrocaloric heat, which was expected, due to the superior design based on a 3D sensor.

6.5.2 Electrocaloric temperature change

Based on DSC measurements, to obtain the true value of ΔT_{EC}, measurements of $Cp_{E=0}$ and Q_{EC} during an EC cycle were applied. The heat capacity was evaluated in both labs and was presented previously in Figure 6.4.

All values of ΔT_{EC} taken upon cooling for both labs can be seen in Figure 6.8, where squares representing LNE and circles ICL and the one measured with the IR camera with triangles. For the two highest electric fields of 16 $kV\,cm^{-1}$ (for LNE is 14 $kV\,cm^{-1}$) and 20 $kV\,cm^{-1}$, is where the ECE is the strongest, and was therefore chosen as a representative examples.

Noticeably most of the measured values using different techniques and laboratories agree within their uncertainties. However, one will note an apparent offset between temperature

values acquired with the infrared and calorimetric techniques and are discussed later in this section.

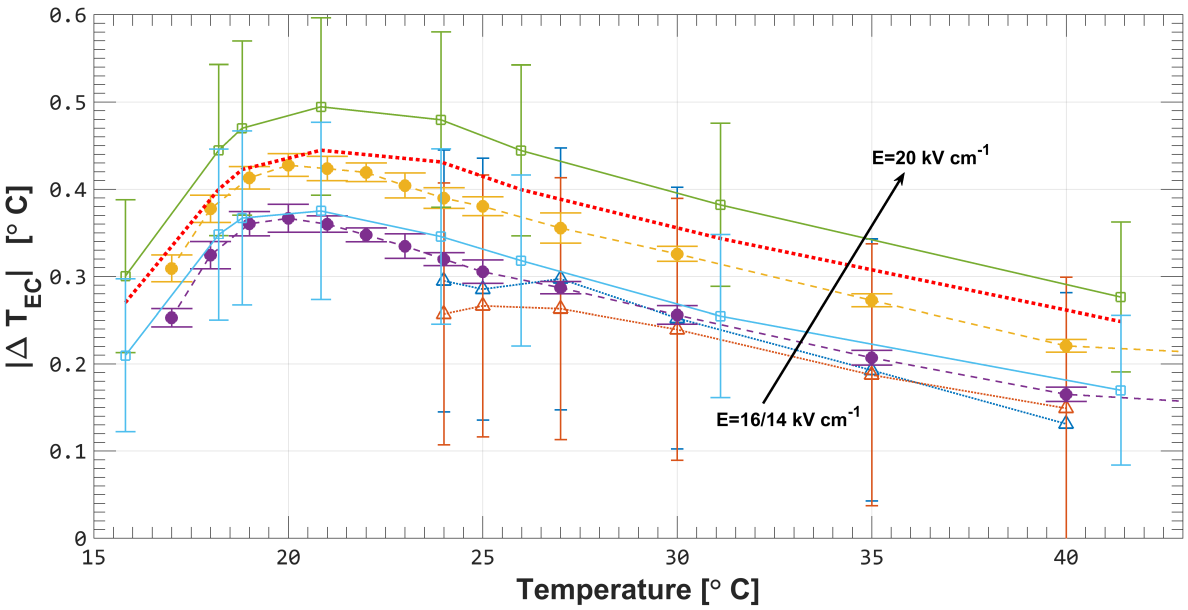

Figure 6.8: Electrocaloric temperature change comparison of values acquired at NPL (triangles with dotted lines), ICL (circles with dashed lines) and LNE (squares with solid lines) for selected electric fields. The additional thick dashed red line represents the ΔQ_{EC} measured at LNE for E-field of 20 $kV\,cm^{-1}$ with calculated $Cp_{E=0}$ from ICL.

Differential scanning calorimeters

Analogous to the acquired Q_{EC}, where the LNE apparatus provided values of measured heat, the trend of ΔT_{EC} follows the same pattern. However, due to the slightly lower heat capacity, Cp, obtained in LNE the discrepancy between Q_{EC} at the highest E-field of 20 $kV\,cm^{-1}$ is higher by approximately 15% in comparison to the ICL value shown in Figure 6.8, but still within the uncertainty. The error bar in Figure 6.8 represents the uncertainty in the case of LNE and NPL results, and for ICL standard error of the mean based on three independent measurements. So it shows that the calculated calorimetric ΔT_{EC} is sensitive to the heat capacity and its error, which is similarly as found during the resistor characterisation (see Section 5.3.4).

The calorimeters' temperature change, ΔT_{EC} is obtained via the heat capacity relation $\Delta T = \frac{\Delta Q}{C_p}$, by prior evaluation of the heat capacity C_p at 0 electric field. Such ΔT is an average temperature integrated by the whole volume of a body. Once the uncertainty and its propagation is considered, the ΔT term includes the error associated with uncertainty considering the heat capacity $u(C_p) = 3.2\%$ and $u(\Delta Q_{EC}) = 3.5\%$ for the LNE measurement. Precisely evaluated errors, including error propagations, for the example measured at 20 $kV\,cm^{-1}$, using equation 6.1, would correspond to the uncertainty range roughly between 20%–30%, rather than uncertainty close to the value associated with ΔQ_{EC} or C_p. The acquired ΔT_{EC} is therefore more sensitive to the Cp and its associated uncertainty. Based on the current case study, shows that if reducing uncertainty by one percent for either the C_p or ΔQ_{EC}, the calculated value of uncertainty would drop by 2% or 5% respectively.

$$u(\Delta T_{EC}) = \frac{1}{Cp} \cdot u(\Delta Q_{EC}) + \frac{\Delta Q_{EC}}{{C_p}^2} \cdot u(C_p) \tag{6.1}$$

For illustrative purposes in Figure 6.8, a predicted electrocaloric response has been plotted with the red dashed line, which is based on the heat measured at LNE and Cp values taken from ICL. This reflects a case when the estimation of EC from heat to temperature (or the other way round) is performed based on parameters found elsewhere e.g. in literature. This is a risky manoeuvre especially once performed on values without uncertainties.

Infrared camera evaluated ΔT_{EC}

In Figure 6.8 the directly acquired infrared ΔT_{EC} is represented by the triangle shaped markers. The NPL apparatus, due to its incapability of cooling a sample environment, cannot fully represent the EC peak values for the BST specimen. ΔT_{IR} was compensated with equation 4.8, because of a lower surface emissivity of BST specimen. The highest magnitude of around 0.30 °C was found as expected at the lowest temperature and when applying a field of 20 $kV\,cm^{-1}$. The standard uncertainty ($k = 1$) of the surface temperature is relatively high $\pm\,0.11$ °C in relation to its magnitude and very reproducible

since the typical standard error is < 0.02 °C (at 24 °C) based on three measurements. Since, the temperature measurement is affected by the environment and possible heat leaks, a moderately fast slew rate allowing delivery of E_{max} in a time of 0.1 s was used. To estimate potential heat loss, the expected heat accumulation in the electrodes was calculated. Based on the assumption that the thickness of painted silver electrodes is roughly equal to 50 μm and that density and specific heat capacity are $\rho_{electrode} \approx 10\ g\,cm^{-3}$, $Cp_{electrode} = 0.24\ J\,g^{-1}\,K^{-1}$ (using the heat values acquired via the DSCs) the electrodes could effectively consume up to 10% of total value of generated electrocaloric heat change. Therefore, to acquire 1 °C change by the infrared camera, up to 10% more heat is required.

The heat leaks through the electrical contact probes are unknown, however a heat flow through good conductors (orders of $10^1 - 10^2\ W\,m^{-m}\,K^{-1}$) such as metals will take place much faster, than in a ceramic material.

Finally, thermal losses were estimated for the NPL setup, on an example of a $BaTiO_3$ multilayer ceramic capacitor [1]. Based on electrocaloric measurements and Finite Element Models (FEM), the estimated convective heat loss to the environment was around 78.8 $W\,m^{-2}\,K^{-1}$ [1] and did not consider the source of the losses. Since it is a rather high value for a natural convection, it may also include the conductive loss through the probes, which were not included in the model. This parameter will depend on multiple factors such as a sample, its volume/mass, surface area, the amount of released heat, thermal properties etc., nonetheless we will use the same value for further consideration. Also, for simplicity of the estimate given the similarity of BST to BTO ($BaTiO_3$) the thermal conductivity $\kappa = 3\ W\,m^{-2}\,K^{-1}$ is used. The acquired Biot number[2] is roughly $Bi \approx 10$. Hence the Bi number indicates a non-uniform temperature inside of the body since the cooling of the body happens faster than heat conduction, through the body. For a Bi number more than 0.1, heat transfer should not be considered as steady state, rather the transient heat transfer should be employed.

[2]Biot number is an dimensionless quantity defining the ratio of heat resistances of inside and at the surface of a body (or as ratio of convective heat transfer of surface to thermal conductivity).

Comparison

When comparing ΔT_{EC} values obtained from the calculated DSC values, the LNE's ΔT values are greater in magnitude than ICL values.The ΔT_{EC} acquired with the infrared camera at NPL is around 30%–35% lower when compared against the ICL or LNE thermodynamic temperature ΔT_{EC}, respectively.

From a theoretical point of view, the heat capacity at $E \neq 0$ is not the same in comparison to $Cp_{E=0}$. This has been predicted in BTO thin films [123, 152] and verified on single crystals of the same material [70, 72], especially, in the case when a first order phase transition is considered, and a substantial latent heat is present [22]. Hence sensitive high-resolution calorimeters should be employed likewise in Ref. [72].

DSC measurement does not include the dynamics of the measurement system (instrument/sample). The zeroth approximation (steady state) gives fairly good values of the heat capacity [119]. However higher order approximation must be included in order to achieve high accuracy and to compensate for the dynamic effects between the DSC setup and the sample.

6.6 Conclusions

The comparison of a bulk BST ceramic pellet has been measured by means of two different methods, at three different laboratories located in two countries. A spread in magnitudes of electrocaloric ΔT_{EC} from 0.49 $\pm$ 0.19 °C ($k = 2$) and 0.43 °C with standard error of around $\pm$ 0.02 °C, close to vicinity of a phase transition (at $\approx$ 20 °C) was found for the DSC techniques. Where for the infrared measurement value of ΔT_{EC} is 0.3 $\pm$ 0.21 °C covering an interval of 95% confidence or standard error of $\pm$0.02 °C acquired at 24 °C. The relative differences of ΔT acquired with the infrared camera was in a range 30% to 35% lesser when compared with the DSC values.

The indirectly estimated electrocaloric ΔT_{EC} value was $\Delta T = 0.8$ °C and due to relatively fast P–E loops is considered to be unsafe for comparison, in agreement with literature [152].

A few important metrology related concerns should be pointed out for measuring ΔT_{EC}:

1. Temperature measurements are affected by environment and specimen. Even though the infrared technique is a non-contact method, hence no partial errors as in a case of contact methods, the type of specimen, mass, thermal properties, thermal losses etc. have to be considered.
2. $\Delta T_{calorimetric} \neq \Delta T_{surface}$. The directly measured values of electrocaloric ΔT taken from surface should not be directly compared to the average 'thermodynamic' values derived from calorimeters, unless an appropriate compensation is made by e.g. finite element thermal model.
3. Errors arise from disturbance of temperature field in specimen. The effect of non-uniform temperature field inside (high Biot number) of the sample, especially for low thermal conductivity body such as ceramic and would be roughly inversely proportional to the thermal conductivity of the body [105].
4. Procedure of the measurements matters. The right procedure ensures the reproducibility of obtained results i.e. measurement of current during direct evaluation (at NPL), or P–E loops not only before direct measurement, but additional verifying loops afterwards for quality reassurance (at ICL). Also such as the pulse rise time, the heat capacity issues, errors propagation and fundamental temperature origins

Chapter 7

Commercial samples: multilayer structures and mechanical coupling

This chapter focuses on the measurement of the electrocaloric effect (ECE) in commercially available samples: a multilayer ceramic capacitor based on a barium titanate ceramics and a piezoelectric ceramic of lead magnesium niobate-lead titanate.

Electrocaloric effect in multilayer ceramic capacitor

Direct measurement of electrocaloric temperature change with calibrated equipment form a good basis for the traceable measurement of the electrocaloric performance of material and device. In this work, direct measurement of the transient temperature of electrocaloric ceramics has been carried out in multilayer structures, using the rig described in Section 4.2. For these measurements, a commercially available specimen, with a phase transition temperature above 100 °C, which also exhibits ECE have been adopted.

7.1 Motivation

The main focus of this study is to investigate the transient temperature change within multilayer structures, a promising candidate for future EC coolers. Additionally, the dynamic behaviour of such structure is investigated with an emphasis on the optimal pulse for a cooling device.

7.2 $BaTiO_3$ Multilayer ceramic capacitor

This section investigates a commercial multilayer ceramic capacitor (MLCC) composed of doped-$BaTiO_3$ ceramic layers. X7R capacitors are used for applications where thermal stability of at least 15% is required within the -55 to 125 °C temperature span [153].

$BaTiO_3$ ceramic is one of the most studied ferroelectric materials, mainly due to high dielectric permittivity and it is one of the lead-free perovskite ceramics with high ECE. It has been considered from the electrocaloric cooling applications, since it exhibits a significant electrocaloric effect ($\sim$ 0.5–1 K close to 100–125 °C, depending on dopants). Moreover, using existing commercial $BaTiO_3$ formulation guarantees reliable samples with longer life time and reproducible results.

7.2.1 Specimen specification

The specifications and dimensions of the MLCC, the based on X7R formulation, capacitance of 1 μF and rated for 400 V from Syfer Technology Ltd., are presented in the Table 7.1. A specimen, were scratched with a diamond razor and fractured (described in following section) was imaged by Scanning Electron Microscopy (SEM) in order to expose the MLCC cross-section, shown in Figure 7.1. The exposed layers shows the straight and uniformly distributed $BaTiO_3$ with thickness of $\approx$ 43 μm sandwiched between a 1 μm thick electrode. In addition to the SEM analysis, the energy dispersive X-ray spectroscopy (EDX) analysis was performed in the SEM. This analysis was performed on the various location of the specimen to verify the average chemical composition. The inner electrodes were made of silver, the body of the capacitor between layers were made of $BaTiO_3$ doped with one or more of the trace elements such as Pd, Nb or Zr, and the connection terminals were made of Ag-based Ni-Ti alloy (for EDX results see Appendix D).

Table 7.1: List of X7R 400V specimen specifications, provided by Syfer Ltd.

Layer Thickness [μm]	No of Layers [/]	Electrodes Thickness [μm]	Rated Voltage [V]	Capacitance [μF]	Effective area [mm^2]	Dimensions (L×W×T) [mm]
42.4	60	1	400	1	2370.4	$8.8 \times 6.3 \times 3$

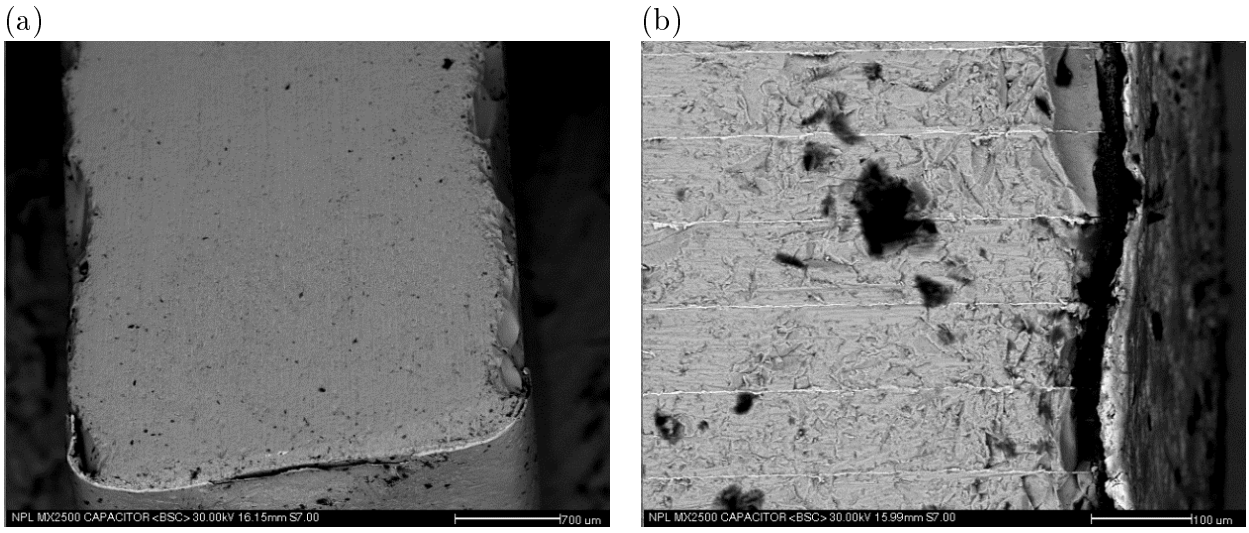

Figure 7.1: Scanning electron microscope image of cross section of the fractured X7R 400V capacitor. (a) Tilted view on cross section (scale bar 700 μm); (b) Close up of capacitor cross-section edge of the electric terminal (scale bar 100 μm).

7.2.2 Cross-section preparation

For direct measurements and SEM imaging, the X7R MLC was cut using a diamond scribe. The sample was coarse polished with a silicon oxide sandpaper and decreasing the abrasive particle size. Then followed by fine polishing with a 1 μm grade diamond paste, to obtain a flat and uniform surface.

7.3 Results

7.3.1 Ferroelectric properties

The electrical performance for ferroelectric materials is normalised to a polarisation-electric field and called the P–E loop. The specimens were tested in the Aixacct TF2000 ferroelectric tester.

Figure 7.2 shows slim and ferroelectric-like P–E loops obtained in X7R capacitors at different temperatures. The saturation polarisation monotonically decreases with an increase of temperature from 12.3 $\mu C\, cm^{-2}$ (at 30 °C) to 5.8 $\mu C\, cm^{-2}$ (at 200 °C). The low remanent polarisation for the temperature span is found to be equal between

1.1 $\mu C\,cm^{-2}$ and 0.1 $\mu C\,cm^{-2}$. Slim P–E loops indicates a low leakage current and exemplifies the hysteretic ferroelectric nature. To avoid dielectric breakdown and to keep high reliability and repeatability, an electric field of $\approx$ 93 $kV\,cm^{-1}$ was applied, which corresponds to 400V across the capacitor. Paraelectric-like P–E loop appears at temperatures $>$ 130 °C indicating phase transition as expected for $BaTiO_3$, as reported in literature [9].

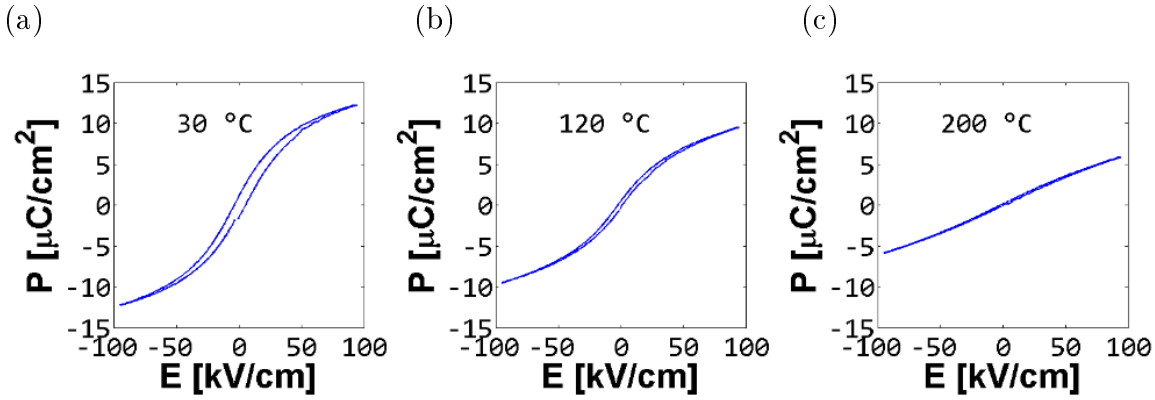

Figure 7.2: Representative polarisation vs. electric field loops obtained for X7R capacitor at selected temperatures: (a) 30 °C, ferroelectric phase (b) 120 °C, close to phase transition and (c) 200 °C, paraelectric phase. Data were obtained upon heating.

7.3.2 Dynamics of the electrocaloric effect

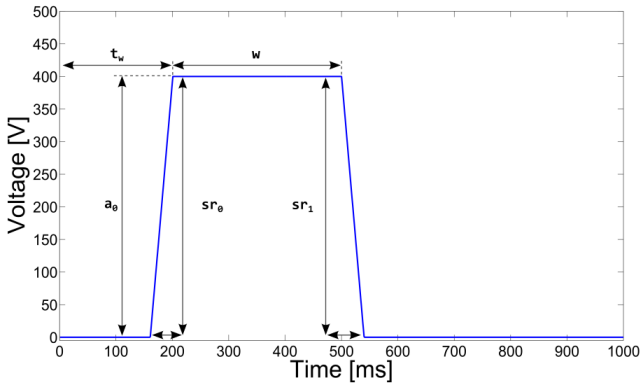

Figure 7.3: Electric field waveform applied to the X7R specimen.

Direct measurements of electrocaloric temperature change were analysed in terms of their dynamics. A square 400 V pulse was applied to the sample after a waiting time (t_w)

varied from 1.9 s to 4.9 s for short and long pulses respectively (see Figure 7.3), with different rise times (slew rates during application sr_0 and withdrawal sr_1 were equal to 4000 $V\,s^{-1}$ for 0.1s duration) and pulse widths w. The effect of pulse width for 11 steps from 0.1 s to 300 s has been investigated. In the first instance, relatively short pulse lengths are presented, 0.1 s, 0.5 s and 1 s, and then followed by longer pulse durations.

Short pulses widths

The results obtained with the high speed infrared imaging allows us to study the instant temperature change, without thermal lag caused by the contact thermal resistance. Figure 7.4 from (a) to (c) shows the progression of the EC response correlated to exothermic temperature measured with sampling rate of 200 Hz. For short pulses the EC response is quicker than the heat transfer to environment, thus the plots do not show net cooling; no presence of $\Delta T_{EC} < 0$ (to compare longer pulse widths, see Figure 7.5).
The heating upon application of electric field and then cooling once field is removed, is discussed for the short duration EC cycle.

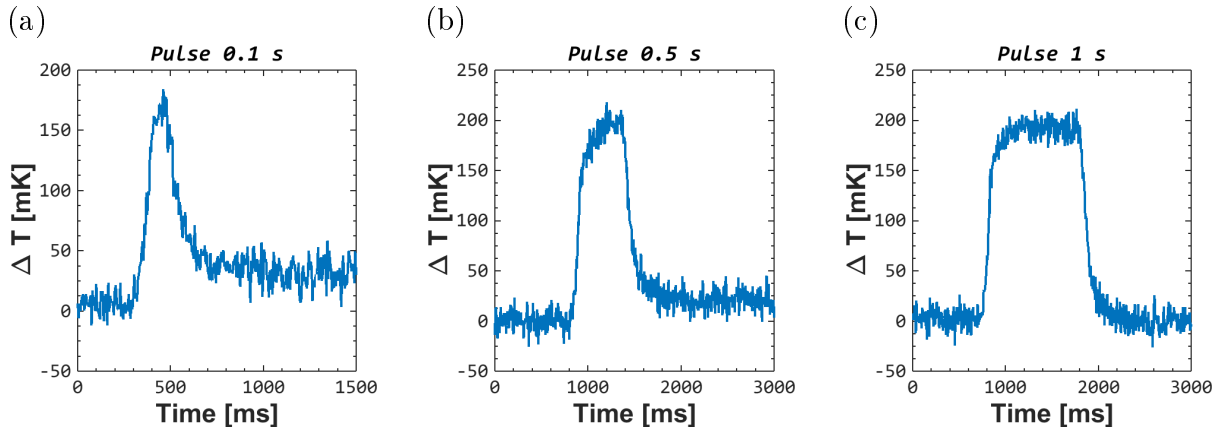

Figure 7.4: Multilayer ceramic capacitor temperature difference ΔT_{IR} measured at the top surface for various pulse lengths (a) 0.1 s (b) 0.5 s and (c) 1 s measured at 25 °C.

The basic temperature change measured with IR camera ΔT_{IR} corresponding to the 0.1 s time of pulse rise from $E_0 \rightarrow E_{max}$ (heating) is 150 mK ($\pm$10 mK of noise/sensitivity), regardless of the duration in the stage of E_{max} constant. In Figure 7.4 (a) a weak rise is seen after the initial 0.1 s ΔE corresponding to $\Delta T = 150\ mK$ followed by an additional

rise of 20 mK. For pulses 0.5 s and 1 s, seen in Figure 7.4 (b) and (c), this additional rise is roughly equal to 40 to 45; mK, so when considering ± 10 mK of noise/sensitivity, in both cases this value can be considered as nearly equal. Typically this additional temperature change is believed to arise from the resistance of the capacitor resulting in Joule heating due to the leakage current formed during E_{max} stage [67].

The exothermic results were compared to endothermic, where the measured ΔT_{IR} during removal of electric field, $E_{max} \rightarrow E_0$ (cooling) leads to the increase of its ΔT magnitude to 80 mK, 120 mK and 140 mK, for the pulses from 0.1 s, 0.5 s to 1 s, respectively. Where for pulses with longer width e.g. pulse 5 or 10s long, this value reaches $\Delta T_{IR} \approx 150$ mK and saturates irrespective of the additional time increase. An interesting observation is that for short pulses of 0.1 s and 0.5 s, ΔT_{IR} does not recover back to zero and remains at the 30 mK and 20 mK levels, respectively. For the pulse duration of 0.5 s, a plateau approaches zero slowly after around 3 seconds.

Longer pulses widths

For pulses 10 second and more the sampling rate was chosen to be less frequent (down to 10 Hz), so the feasible sizes of thermographs sequences could be stored on the hard drive. Figure 7.5 (a) and (b) shows the partially and fully thermally relaxed performance, respectively. A sufficient pulse length slightly above 70 s is adequate to achieve the maximal ΔT_{EC}, in both heating and cooling directions. Once the peak values are extracted for fully relaxed pulses, both directions reach comparable magnitudes at around 200 mK. Based on exponential fittings, the time constant τ_c close to 25 seconds has been found for both cooling and heating slopes and the thermal relaxation of a sample environment system has been acquired.

7.3.3 Electrocaloric effect in MLCC cross-section

Based on the findings of a thermally inactive layer, of which more can be found in further discussions (see section 7.4), the distribution of ΔT is investigated inside the capacitor.

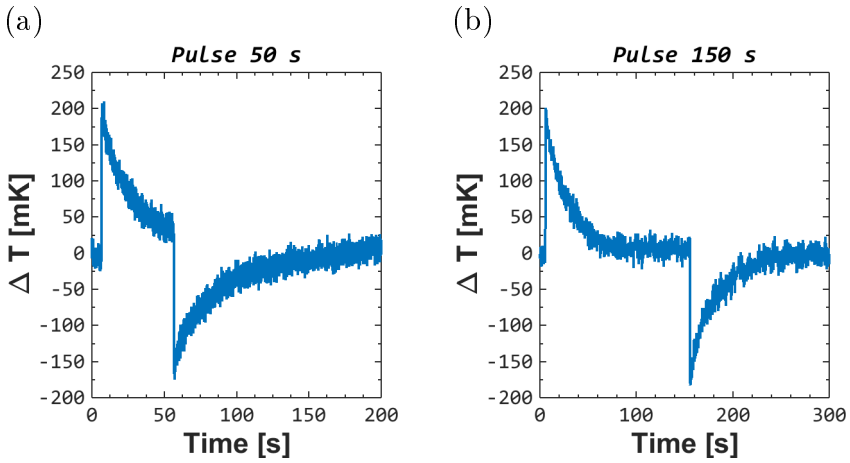

Figure 7.5: Multilayer ceramic capacitors temperature difference ΔT_{IR} measured at the top surface for a various pulse lengths (a) 50 s and (b) 150 s, both measured at 25 °C.

Figure 7.6 shows a thermograph of the uncovered layered features of cross-section and confocal microscopy image for reference. The blurry (unfocused) part of the image is a result of the uneven polishing and tilt with respect to focal plane of the camera. The confocal image shows the horizontal structure of layers. These measurements were

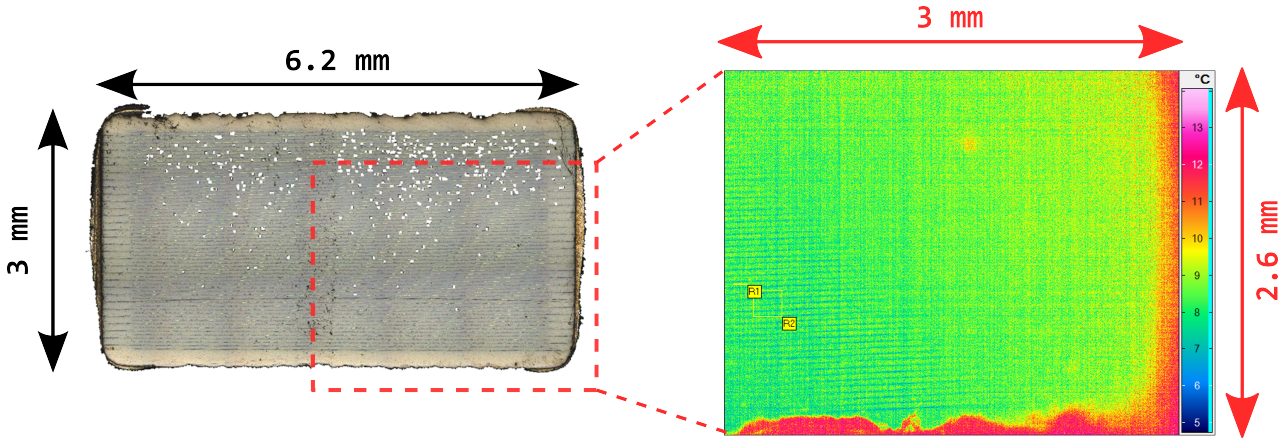

Figure 7.6: Thermograph and confocal microscopy image of the multilayer ceramic capacitor cross-section with dimensions of the specimen and the field of view, at room temperature. The red areas on the bottom and right-hand side of the thermograph corresponds to the edges of the capacitor. The areas without colour on the confocal image corresponds to pixels of which microscope was unable to obtain focus.

acquired without an active anti-vibration stage. The active layer thickness, measured with the SEM microscope, on average is ≈ 43 μm and where the resolution of IR camera is 5 μm per pixel, which approximately corresponds to area 8 pixels in thickness. Therefore, to smooth the data, the high frequency noise was reduced by a moving average filter.

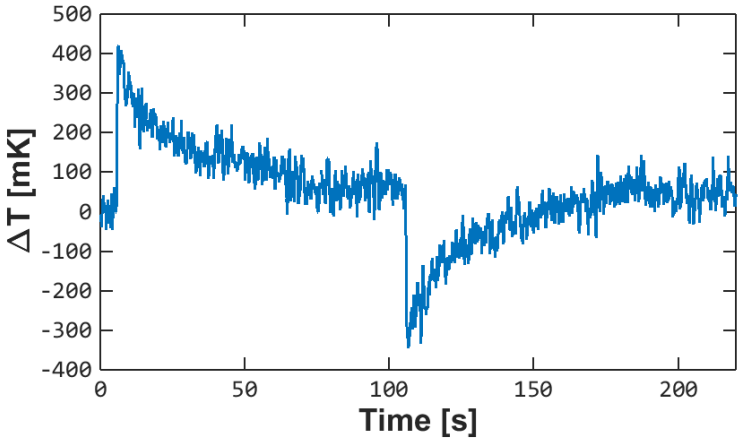

Figure 7.7: The ΔT over time for X7R under application of rectangular 400 V waveform, measured at cross-section on area $R2$ at room temperature.

Based on fittings the ΔT amplitude of 329 mK and -312 mK were determined from data plotted in Figure 7.7.

7.3.4 Electrocaloric effect as a function of temperature

Indirect EC estimation method

Electrocaloric ΔS and ΔT were calculated for the X7R capacitor using the electrocaloric equations 2.13 and 2.15, in Section 2.3. These calculations based on the P(E, T) dataset are presented in Figure 7.2, on selected P–E loops. The EC results are shown in Figure 7.8. Polarisation as a function of E-field data was firstly numerically interpolated to finer equal intervals and then the entropy change was numerically integrated. Further to estimate ΔT the ΔS, the constant density $\rho = 5.46 \times 10^6\ g\,m^{-3}$ and volumetric heat capacity $C = 0.42\ J\,g^{-1}\,K^{-1}$ were applied. In both Figures 7.8 (a) and (b) the clear peak of the phase transition is seen at $T = 140$ °C, corresponding to the maximal magnitudes of $\Delta S \approx 4300\ J\,m^{-3}\,K^{-1}$ and $\Delta T \approx 0.66$ °C, at the highest electric field ($E_{max} = 93\ kV\,cm^{-1}$). At temperature close to room temperature these magnitudes are equal $\Delta S \approx 2300\ J\,m^{-3}\,K^{-1}$ and $\Delta T \approx 0.25$ °C and then rising slightly above 100 °C, to the magnitude of around 0.35 °C. Small two local peaks can be found at the around

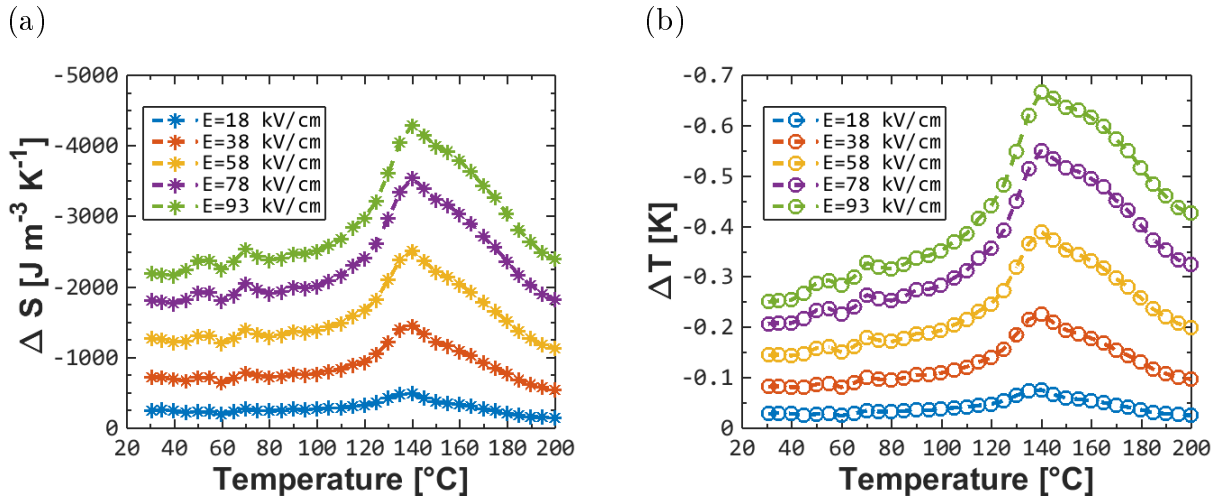

Figure 7.8: Electrocaloric effect estimated with indirect method (a) Entropy change ΔS over T and (b) Electrocaloric temperature change ΔT over T for selected electric fields E, based on P–E loops in temperature range $30 - 200$ °C in ascending order.

50 °C and 70 °C.

Direct EC method

The magnitude of the ΔT_{IR} both upon heating and cooling measured on the cross-section in the temperature span 25–180 °C is shown in Figure 7.9. The slower and faster slew rates at 400 V was applied across the structure for 0.2 s and 0.1 s for heating and cooling, respectively.

The maximum values of directly measured electrocaloric effect was $\Delta T = 0.71$ °C during heating and $\Delta T = 0.69$ °C during cooling with an expanded uncertainty ($k = 2$) of ± 0.23 °C at the temperature of 140 °C and found in between the exposed active layers of electrocaloric material. The standard error at that highest values is equal 0.05 °C based on the three measurements.

7.4 Discussion

This BTO-based X7R MLCC with a phase transition around the 140 °C was confirmed to be ferroelectric exhibiting slim P–E loops. The EDX measurement suggested two possible

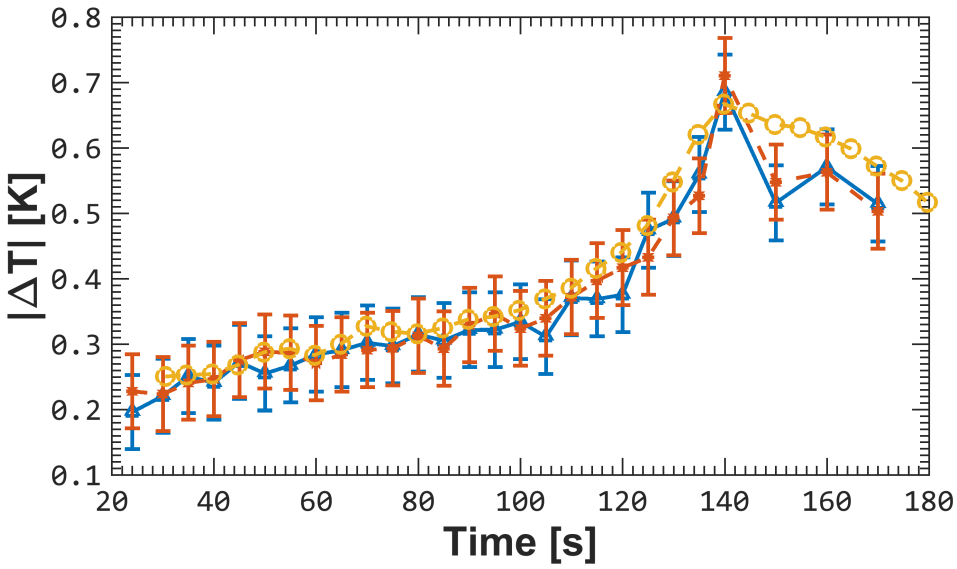

Figure 7.9: Directly measured electrocaloric effect in multilayer ceramic capacitor cross-section X7R measured for the temperature span from 25–180 °C heating (red dashed line) and cooling (blue line) and indirect estimated ΔT values for the highest field (orange circles) measured for a 400 V (corresponding to 93 $kV\,cm^{-1}$), 150 s pulse and 1 Hz P–E loops. Direct method values are compensated for the attenuation of the sapphire window, sample emissivity and size of source effect.

dopants, niobium and zirconium. According to the supplier, the X7R commercial formula aims to achieve the best linear electrical charge storage property (relative permittivity) in the operational temperature region.

7.4.1 Dynamics of electrocaloric effect

Short pulse width

The results show the lack of perfect symmetry between heating and cooling. This is reflected as Joule heating, due to leakage current ($\sim 1\ \mu A$) present in MLCC structures [154]. The net cooling is not delivered in the case of short pulses, which can be a result of insufficient time for heat dissipation. Hence, the two aspects of ECE are considered subsequently, namely the electrical and thermal perspective.

The electrical origin of this discrepancy is treated as Ohmic losses, because of current

flow through the device during the fully charged stage and understood as a static leakage current. In electronics, this is represented by using the simplistic equivalent electrical diagram of EC capacitor. An ideal capacitor and resistor are connected in parallel, corresponding to the real capacitance and leakage resistance (DC resistance) of the specimen. Typically, during the 'hot' cycle, the EC material is under constant electric field which is maintained by the voltage source, hence the additional need of current (e.g. leakage current) will be compensated by the source. Thus, such leakage current is dissipated as heat usually seen as an offset from initial temperature, especially for longer duration (5 x capacitor time constant and more).

Conversely during the cooling stage (of the typical materials[1]) the electric field is equal to zero, therefore no static (DC) loss can be produced. Dynamic processes for current delivery during the electric field change, which is a driving force of the effect, are quite often neglected. In this case, the electrical diagram of a capacitor is usually represented as a series resistance in equivalent circuit. During charging/discharging of the capacitor, heat will be generated in capacitor according to $Q_{ohmic} \sim I^2R$. These are typically small resistances of $< k\Omega$ and are influenced by the transient flow of the charge in relatively small time scale resulting in relatively high peak values of the transient current. For demonstration purposes the current data acquired during directly measured ECE in a cross-section at 30 °C used. Note that for these measurement,s a pulse of 100 s length was used, with non-symmetrical rises of 0.2 s and 0.1 s for rise and fall, respectively. Peak currents of 414 μA and 1407 μA according to manufacturer data would result in very low magnitudes of ΔT, below 0.1 mK. The X7R capacitor was designed to exhibit very low values of equivalent series resistance. Once compiling the same peak currents with resistance of 1 $k\Omega$, a temporal temperature would still be insignificantly small and equal to $< 1\ mK$ and $\approx 1\ mK$. Additionally, one may notice that a noticeable change of almost an order of magnitude difference in peak current can be achieved by decreasing the rise time by half at moderately slow slew rates. Therefore there is an additional risk of reduction the value of ECE under application of pulses with high slew rates.

[1]There are 'reverse materials' e.g. PST, which inversely to the conventional EC materials, during application of ΔE cools down [29].

When the thermal flow was considered at the shortest pulse, the measured ΔT magnitude suggests a pulse of 0.1 s with an offset of 30 mK (static loss) from the 0-level and 'dynamic loss' offset of around 70 mK (150 mK upon rise + 20 mK of additional peak at E_{max} -80 mK off cooling and -30 mK offset). As calculated above, this phenomenon cannot be a result of the electrical 'dynamic' heat loss only and a thermal buffer is suggested.
In terms of the heat transfer duration in the ceramic material such as $BaTiO_3$, measured on a distance of below < 0.1 mm will be in the range of tens of ms. Thus when considering the discussed surface temperature measurements, which were performed on top of the capacitor, the thermally inactive layer above the active material was roughly 100 μm thick (see SEM micrograph, Figure 7.1). Therefore, such a thermal buffer may affect the accuracy of measurement, both the amplitude and time lags/lengths. Moreover, it would allow retention of heat which could explain the remaining offsets after application of driving electric fields for short pulses of 0.1 s and 0.5 s.

Longer pulses width

Longer pulses allows for a net cooling. Therefore, a sufficient duration of applied electric field is particularly useful in direct measurements since this shows full heat exchange with the environment and the peak ΔT_{EC} values, where the sample reaches thermodynamic steady state conditions. For each material the maximum value of ΔT_{EC} was obtained before full relaxation, which may have reduce the measurement time and increased failures due to dielectric breakdown under high field. Nonetheless, it is still advantageous to keep the pulse length longer, since the DC thermal loss can be calculated with respect to initial temperature and a better fit of exponential decay can be obtained. Based on Figure 7.5 (b) the thermal loss offsets the relaxed specimen after 100th second nearly $\approx 10 \pm 10$ mK compare to steady temperature. This low loss is expected as a consequence of static Joule heating, since the slim P–E loops corresponds to high impedance of > 500 $M\Omega$ (estimated with ferroelectric tester) and secondly low leakage current of around 5 μA.

7.4.2 Data extraction method

Due to lack of symmetries in pulses, to understand this case more the data have been extracted and represented on Figure 7.10. Three different methods to extract ΔT were used to characterise the EC performance, namely the exponential fitting, peak values and rise/fall times.

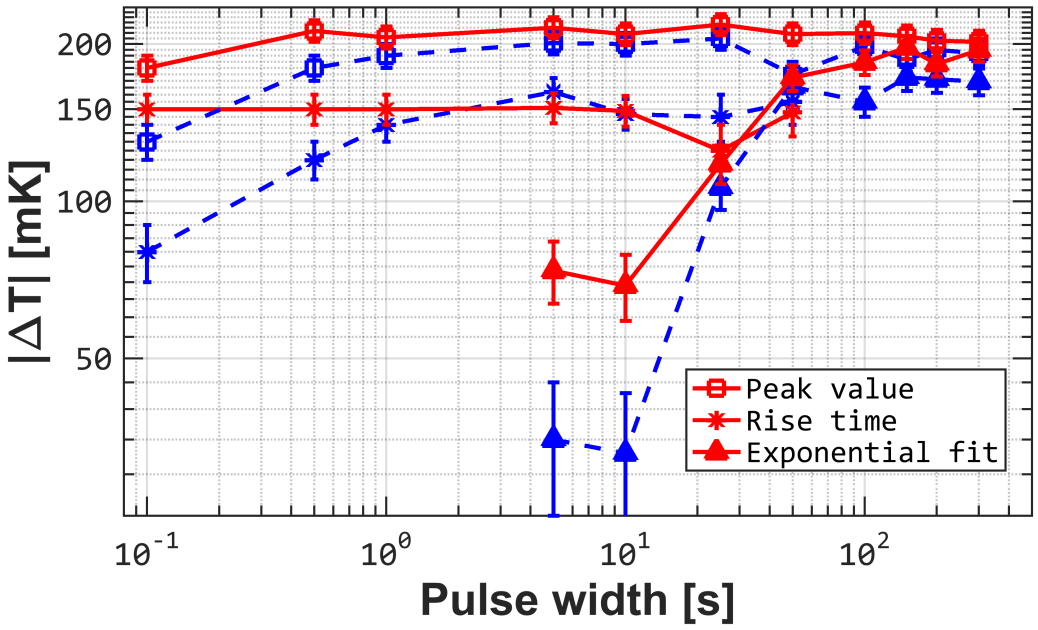

Figure 7.10: The magnitude of electrocaloric temperature change ΔT as a function of the pulse width depending on the type of analysis; peak values (squares markers), rise times of the ΔE (asterisk markers), exponential decay fitting (triangle markers), where the red solid line corresponds to heating and blue dashed line to cooling.

First, conventionally the exponential decay is fitted to the data to extract EC performance [117] as:

$$T(t) = \Delta T e^{\frac{-(t-t_0)}{\tau_c}} \tag{7.1}$$

where the $T(t)$ is a time resolved temperature, ΔT magnitude of EC effect, t_0 initial time and τ_c is the characteristic relaxation time constant (heat dissipation). These data are plotted in Figure 7.10 with triangular markers (red solid line corresponds to heating and blue dashed line to cooling). The disadvantage of such analysis method is that fitting can only be performed for longer duration pulses, which disallows comparison to the shorter

pulses widths.

According to the definition of the electrocaloric effect, $\Delta T/\Delta S$ is a result of ΔE, which happens during the t_{rise} or t_{fall}. Hence, the ΔE rise/fall time – where the EC change is extracted only during rise time corresponding to the transition of $E_0 \rightarrow E_{max}$, and on the fall in the opposite direction. Third, the peak values – where the difference is taken from maximum and minimum peak ΔT from the initial T_0 and final of hot stage temperature, both presented on the Figure 7.10 with asterisk and square markers, respectively.

All three methods show a magnitude difference between 'hot' (red solid lines) and 'cold' (blue dashed lines) stages of EC response, apart from the method of rise times for 'short' durations. Focusing on the temperature difference arising from the driving force: the ΔE, this remains a nearly constant value of around $150mK$. In the initial stage of $0.1\,s$ up to $1\,s$, the inequity is noticeable, which would suggest the relevance of dynamic heating or heat retention.

The extraction of peak values of ΔT corresponds to the highest magnitudes of acquired ΔT and demonstrates that 'full recovery' can be achieved if the pulse width is $> 1\ s$.

A similar fast recovery between heating and cooling was found for the time rise/fall method. This method suggests that to observe any thermal effects within the specimen, a constant value of heating around 150 mK is needed regardless of the pulse duration. At longer lengths, this magnitude does not change, however the points are more scattered, due to the short rise/fall times and lowered sampling rate, hence the bigger errors. For clarity, Figure 7.10 does not includes these further points.

The fitting method shows that thermal recovery can be achieved after $25\ s$. Fitting allows us to extract the average temperature values. At saturated levels of $> 100\ s$ the difference in contrast to peak values extracted upon cooling is lower by $20\ mK$ on average, which is close to noise of the measurements.

7.4.3 Optimal electrocaloric performance

To further explore the pulse length effect on the transient response of a heat exchanging process, a normalisation was employed. In this case the area under the each pulse of temperature, both on exothermic and endothermic action, was normalised to the electric field producing the effect as a function of time. The ratio of the integrated areas with respect to time under the graphs is plotted as a function of pulse width in Figure 7.11. Using the analogy of the capacitor charge/discharge process, the transient region is between established 0 and 4 τ_c, and above that where charge/discharge process exists is treated as steady state period. The fully charged capacitor/discharge state is reflected as a 5 τ_c where the 98% of process completion is achieved.

Analysing the exothermic part, a maximum has been found for the pulse duration of 5 s ($\approx {}^{1}/_{5}\ \tau_c$). From the perspective of a cooling device, the less heat dissipated in the system, an operation at this peak region should be avoided. Surprisingly, the short pulses, where the highest discrepancies between heating and cooling, were found not to be the worse location from the perspective of the transient 'efficiency'. Its lowest value is achieved at the longest width of 300 s. This is due to the long duration of the pulse width which does not corresponding to further improvements. The best temperature exchange upon cooling performance was found at the 2 τ_c. At this time of 50 seconds duration, the heating and cooling 'efficiency rates' are nearly the same. Due to the lack of a net cooling at short periods, it was not possible to take into account the fitting method, shown in the previous section.

The short pulses showed the highest magnitude of rationalised $T_{area}\, E_{area}{}^{-1}$ parameter suggesting proportionally more heating, of unknown origin, outperforming the highest 'efficiency' of cooling point (at the 2 τ_c width) by factor of 2. In other words once the pulse duration is chosen incorrectly, the capacitor can produce twice more temperature rise than cooling at the optimal point. In relation to the capacitor transient model, the 2 τ_c corresponds to 83% of discharge, whereas here was equal to 95%, 95% and 85% for the data extracted by fitting, rise time and peak value methods, respectively.

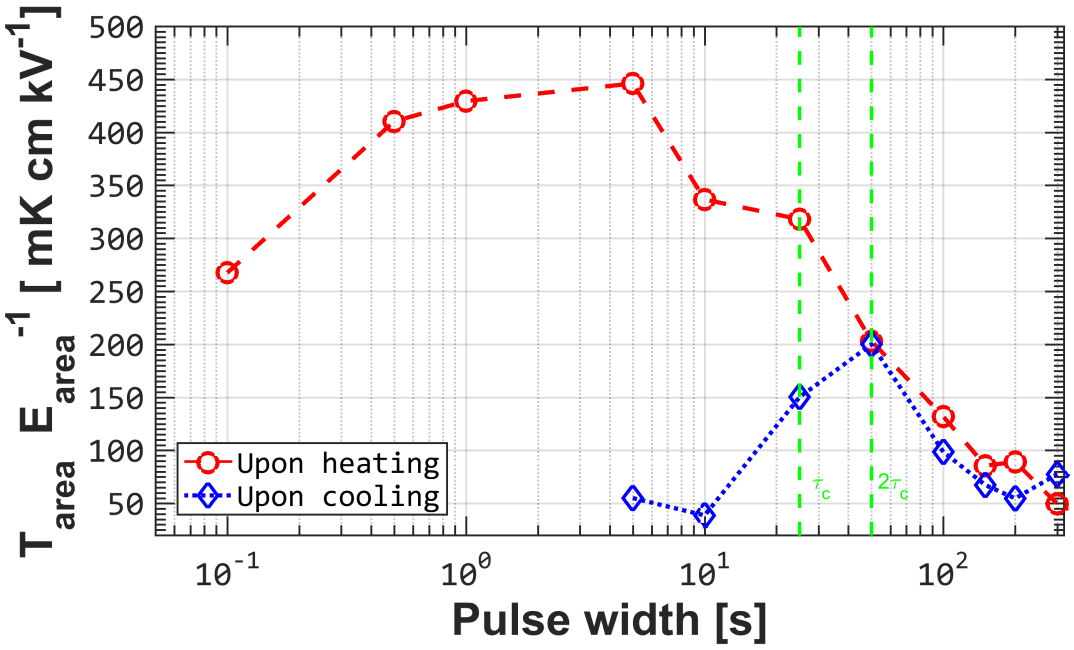

Figure 7.11: Optimum performance of electrocaloric MLCC, represented as a magnitude of transient temperature areas to transient electric field areas under the curves of measured pulses as a function of pulse width; the green dashed line τ_c and 2 τ_c are the thermal time constant and twice value denoting the optimal pulse length for cooling application.

7.4.4 'Temperature losses' in the measurement

All the above findings of transient behaviour, strongly suggest the issues with heat flow, hence a suspicion that an inactive thermal buffer is contributing to the thermal losses.

Any loading of heat into electrodes, metallic connection terminals, or any additional heat leaks can be a source of apparent temperature reduction. Once the specimen structure is closely analysed (see Figure 7.12), several findings can be reached. Based on the

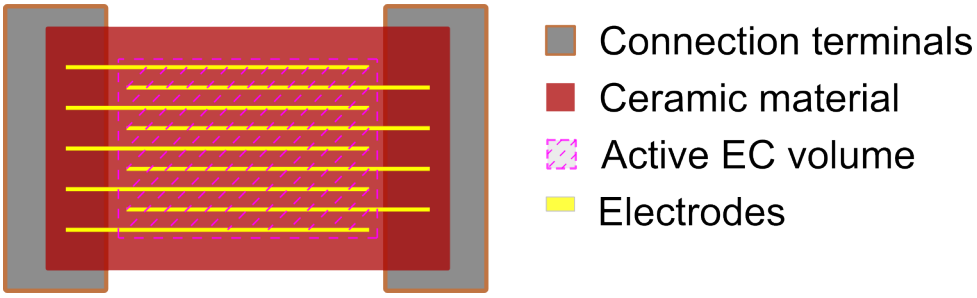

Figure 7.12: Schematic of multilayer capacitor structure, cross-section perpendicular to layers with highlighted active electrocaloric volume (magenta dashed line). Schematic not to scale.

dimensions of a capacitor, data from the manufacturer and dimensions found through the SEM imaging, the active volume of a capacitor responsible for exhibition of ECE is roughly equal to 60% of total volume. This gives a thermal buffer of almost 40% which corresponds to absorption of around 0.156 $J\,K^{-1}$. The silver electrodes' and metallic terminal are estimated to correspond to around of 1.5% of total volume. The specific heat capacity Cp of the silver is 235 $J\,kg^{-1}\,K^{-1}$ and therefore 55% of the Cp for BTO [1]. The terminals are made of silver alloy with a mix of Ni and Ti, however for a simplification can be treated as pure silver, since it is one of best thermal conductors. The thermal conductivity was compared between electrodes showing a value of 2.6 $W\,m^{-1}\,K^{-1}$, meaning that the electrodes are more than 160 times better heat conductor than the BTO. This agrees with simulations on various MLCC compositions where Ag electrodes significantly improved heat removal from inside the capacitor [155] and also enabled a reduction in thickness of electrodes to enable equivalent cooling rates, in comparison with other metallic electrodes [155, 156].

The EC effect measured inside the MLC shows that the magnitude within the thick layers is much greater than in bulk material. Time of heat to flow from the inside to the outside of the capacitor would approximately take around 220 ms and agrees with the findings in the shortest applied pulses. The findings of the thermal buffer was verified for the X7R MLCC by a finite element model, which predicted greater magnitude of the ECE within the capacitor rather than outside of the capacitor [1]. As discussed in the next section.

These arguments, of dynamic losses or thermal buffer layers are not addressed in literature, no practical guidance to assessing MLC structures is present. Even though the non-contact method was utilised, a similar scenario to the concept of principal errors associated with contact method e.g. thermal resistance or deformation of a temperature field (see Section 3.2) is in concordance with these findings.

7.4.5 Electrocaloric effect – cross-section

Once the temperature was measured in the middle of the electrocaloric layers, a higher temperature change was observed. Based on the average value extracted with exponential fitting during an endothermic peak is twice as big, in comparison to the one at the top of the specimen.

The thermal losses have been reduced by the removal of a buffer layer above the active area. Secondly, additional benefit of measuring the temperature inside of a specimen between layers, the closer to adiabatic conditions can be achieved. Another aspect of such temperature measurements using a thermal camera is the spatial resolution. This demonstrated that the temperature gradient can be detected and this results was backed up by the additional finite element model [1].

7.4.6 Direct and indirect electrocaloric effect

When comparing the results of direct measurements to indirectly estimated ones, we observe the same trends. Initial linear growth of the amplitude up to 120 °C and then position of the phase transition can be observed. The direct method goes in hand with the indirect estimation, with slightly higher values for most of values estimated with indirect. Only one detail, peak values around phase transition at 140 °C acquired with the direct method show slightly sharper peaks than with indirect estimation. Most of the compared points lay within the error bars of direct measurements.

7.5 Conclusions

In this chapter electrocaloric behaviour was characterised, with indirect and direct methods. A good agreement between them was found for the whole evaluated temperature span, which is usually the case for a first phase order perovskite material such as BTO at low frequency regime (relatively slow pulses rise/fall times). Based on measurement of the

cross-section, the value of $\Delta T = 0.71$ °C during heating and $\Delta T = 0.69$ °C during cooling with an expanded uncertainty ($k = 2$) of ± 0.23 °C and the standard error of 0.05 °C was obtained when measured at $T = 140$ °C.

ECE is an electro-thermal cross-coupled phenomenon exhibited at the different time scales, from the very fast electrical counterpart and much slower thermal transport. The thermal time constant for heat dissipation has been found to be $\approx 25\ s$. An optimal cooling performance has been found to be equal to the two time constants $2\ \tau_c = 50\ s$ duration of applied electric field. Dynamic Joule heating was found to be negligible in this case.

Different data extraction methods were utilised, as a good practice to cross-check if the structure complexity does not affect the characterisation results. Thus, systematic offsets and random error can be detected during the measurements, and appropriate mitigation can be exploited.

A novel approach of investigating the electrocaloric temperature response of a multilayer structures *'in vivo'*, in between thick film layers of the commercial capacitor, allowed to detect significant difference in acquired magnitudes of ΔT_{EC}. A two-fold electrocaloric temperature change ΔT_{EC} was measured at several exposed micro-size thick-film layers in compare to the value when measured on the surface.

Finally, infrared thermography proved to be a promising technique if the thermal propagations and device characterisation such as optimal performance, are of interest. Moreover, in future EC cooler applications, a transient temperature performance of such device is an essential part of the design and makes a non-contact method more promising for future developments in electrocaloric cooling.

Investigation of mechanical coupling of electrocaloric effect

In this section, a mechanical contribution is investigated in the ferroelectric relaxor composition, the $Pb(Mg_{1/3}Nb_{2/3})O_3 - PbTiO_3$ (PMN-PT). Here the focus is set on the strong couplings with other properties which may affect the EC performance. Hence, the influence of the mechanical (secondary) contribution is investigated. The dielectric, electro-mechanic and electrocaloric properties are characterised.

7.6 Motivation

The aim of this study is to investigate the additional source of errors, during the characterisation of EC specimens and which were not considered in the uncertainty budget.

7.7 Polycrystalline PMN-PT relaxor ceramic

A commercial 2 $mm \times 2$ mm thick and 6 mm long PMN-PT ceramic (ESC-1, Morgan) bar has been investigated. Silver electrodes were placed on the parallel 2 $mm \times 6$ mm faces. Although the exact composition including dopants was not specified, the ceramic was close to the morphotropic[2] phase boundary exhibited relaxor behaviour indicated by the frequency dependence of the permittivity peak (shown in below subsection 7.8.1).

[2]is the phase boundary between tetragonal and rhombohedral regions in a ferroelectric material.

The main interest in PMN-PT composition is due to promising high values of ΔT_{EC} and broad phase transition range.

7.8 Characterisation

7.8.1 Electrical and mechanical properties

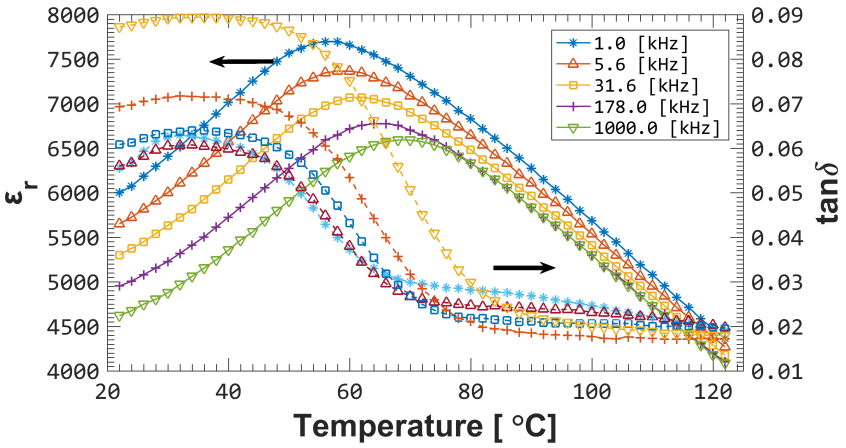

Figure 7.13: PMN-PT bulk ceramic relative permittivity ε_r (lines) and loss tan δ (dashed lines) as a function of temperature, for selected frequencies varied from $1 - 1000$ kHz (corresponding markers shapes are depicted in the plot legend).

Figure 7.13 shows the temperature and frequency response of the relative permittivity ε_r and dielectric loss tan δ measured for the PMN-PT sample. Classical frequency dependent relaxor-paraelectric behaviour is observed as ε_r peak shifting and boarding with frequency. The ε_r peak of nearly 8000 at ≈ 60 °C for 1 kHz shifts to relative permittivity of 6000 at ≈ 70 °C for 100 kHz of frequency. Once considering the broadening of the permittivity peaks on current data the full-width at half-maximum (FWHM) was impossible to apply, since the value of permittivity at room temperature did drop significantly below 20 % of a maximum peak. So instead of FHWM formula (50% drop) the drop of 20 % from maximum was used to interpret the width of peaks. This resulted in the width of $\approx$ 67 °C for 1 kHz reduction down to the $\approx$ 62°C for 100 kHz. The dielectric loss $tan\delta$ maximal value was found 0.09 close to room temperature for 100 kHz and was also

frequency depended. The relaxor nature of the ceramic is corroborated by the observed slim S-shaped P–E loops at temperatures below 60 °C, seen in Figure 7.14 (a). The slim polarization P–E loop and mechanical displacement D–E loops are seen in Figure 7.14 and were simultaneously measured upon application of a triangular-shaped bipolar E field. The D–E loops at 30 °C show the highest displacement of more than 2000 nm at the maximal applied electric field of 21 $kV\,cm^{-1}$ corresponding to strain above 0.10%.

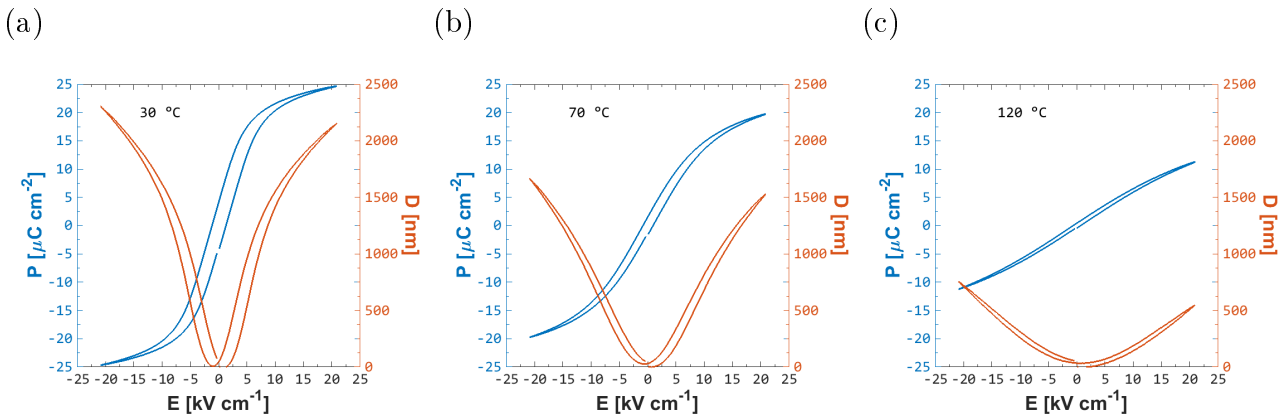

Figure 7.14: Polarisation, P, and displacement, D, loops as a function of E-field at selected temperatures (a) 30 °C, relaxor phase (b) 70 °C, close to phase transition and (c) 120 °C, paraelectric phase. Measurement were taken at 1 Hz cycling frequency.

7.8.2 Direct measurement

The electrocaloric effect in the PMN-PT sample was measured at room temperature with the electric field below 10 $kV\,cm^{-1}$. The electric fields were applied with a ramp rate corresponding to the 1 Hz P–E loop (E_0 to E_{max} in time of 0.25 s). The 50 s long pulse widths with an amplitude up to 10 $kV cm^{-1}$ were applied. Values above that electric field resulted in the breakdown of the samples. Figure 7.15 (a) represent a direct measurement of ECE for the highest applied electric field of 9 $kV\,cm^{-1}$. The extracted values from 0.16 K and -0.16 K of ECE compare favourably with the estimated values by the indirect estimation method for the low field (see Section 7.8.3). Furthermore in Figure 7.15 (b) the growth of the ΔT is fairly linear with the rise in the electric field.

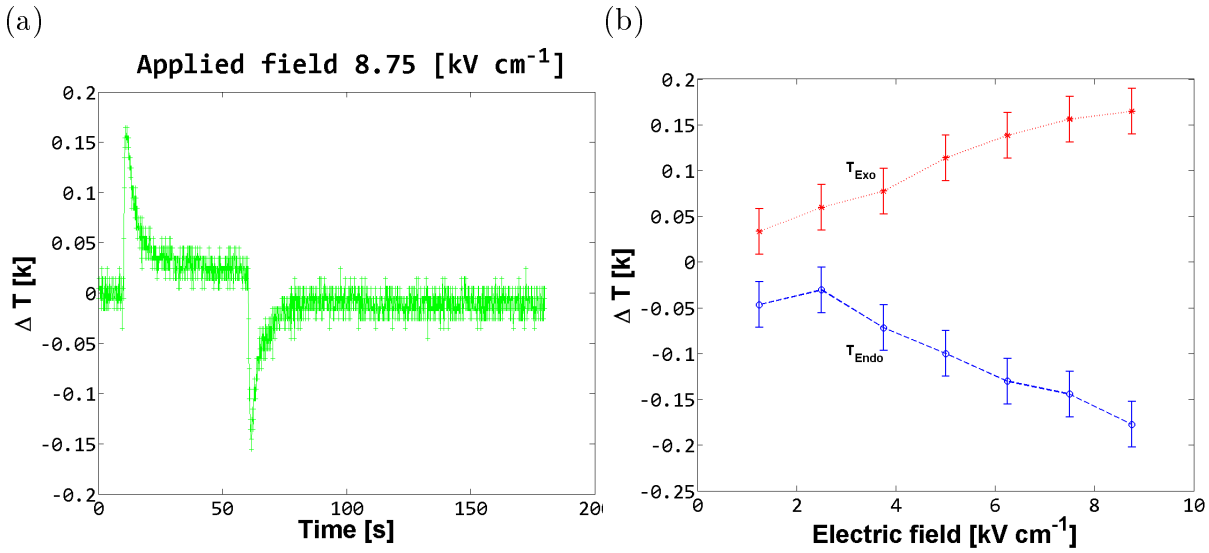

Figure 7.15: Direct method electrocaloric effect ΔT in the PMN-PT sample (a) measured at 8.75 $kV\,cm^{-1}$ and (b) as a function of E-field. Measurement at the room temperature.

7.8.3 Indirect estimation

The indirectly estimated electrocaloric response was calculated via electrocaloric equations 2.13 and 2.15, based on the $P(E,T)$ dataset (representative P–E loops are shown Figure 7.14) measured for the temperature range 30–200 °C at an electric field of 21 $kV\,cm^{-1}$. Figure 7.16 shows the calculated entropy change which reaches its maximum of around 3500 $J\,m^{-3}\,K^{-1}$ at $\approx$ 75 °C.

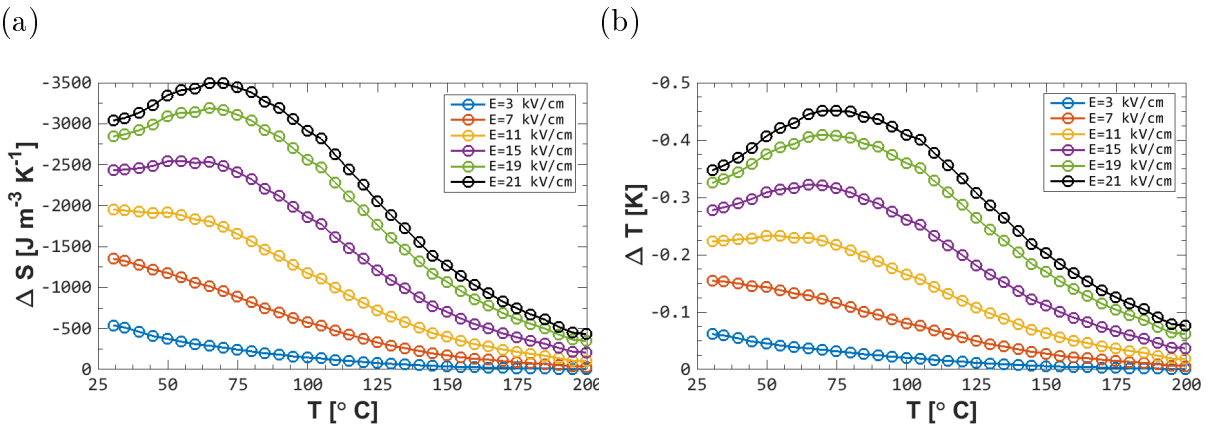

Figure 7.16: PMN-PT values for indirectly estimated electrocaloric (a) entropy change ΔS over T and (b) temperature change ΔT over T.

The electrocaloric temperature change ΔT was determined using on the extracted entropy change ΔS. For calculation the constant heat capacity, $C = 320\ J\,kg^{-1}\,K^{-1}$ and density

$\rho = 8.3\ g\,cm^{-3}$ [23] were used. The maximal value of $\Delta T \approx 0.45\ K$ can be extracted from Figure 7.16 (b). One may observe that ΔT is dependent on the electric field and temperature. In ascending order of the electric field the maximum value of ΔT shifts towards lower temperatures. Such electric field dependence has been reported previously [51] and the broadening is expected to be more pronounced at higher fields. However, here dual-peak can not be clearly seen due to relatively low electric fields, so only the broadening of the predicted ΔT and shift of the peak value for higher fields, which are predicted to be further extended as a consequence of polar nanoregion activated by additional pressure or electric field [84].

Once the ΔT_{EC} is normalised with respect to the applied electric field, the non-linear behaviour can be visualised as seen in Figure 7.17 (a). The 2-dimensional non-linear behaviour is observed, both with respect to electric field and temperature. When analysing the value for the highest applied E-field of 21 $kV\,cm^{-1}$, the $\Delta T\,E^{-1}$ grows non-linearly for around -2.5×10^{-6} at 30 °C to $-2 \times 10^{-6}\ K\,cm\,V^{-1}$ at 70 °C. The additional local peak of almost $-2.5 \times 10^{-6}\ K\,cm\,V^{-1}$ occurs at 55 °C.

The peak value of normalised electrocaloric temperature change with respect to electric field is equal to $\approx -4.2 \times 10^{-6}\ K\,cm\,V^{-1}$ and occurs at the lowest measured temperature the 30 °C under application of the $E \approx 5\ kV\,cm^{-1}$. Once temperature is increased the strength of the ECE with respect to applied electric field will reduce.

Due to the local extreme values of the $\Delta T\,E^{-1}$ the critical electric field of its existence is represented on the Figure 7.17 (b). Strong criticality exists only up to the 'phase transition' temperature of $\approx$ 75 °C and reduces significantly above 85 °C. At this point the value of $\Delta T\,E^{-1}$ plateaus to values $< -5 \times 10^{-7}\ K\,cm\,V^{-1}$. After the sample reaches more than 100 °C the electric field dependence vanishes for the magnitudes applied during these measurements. Therefore the normalised ΔT nearly linearly decreases regardless of the electric field magnitude.

(a)

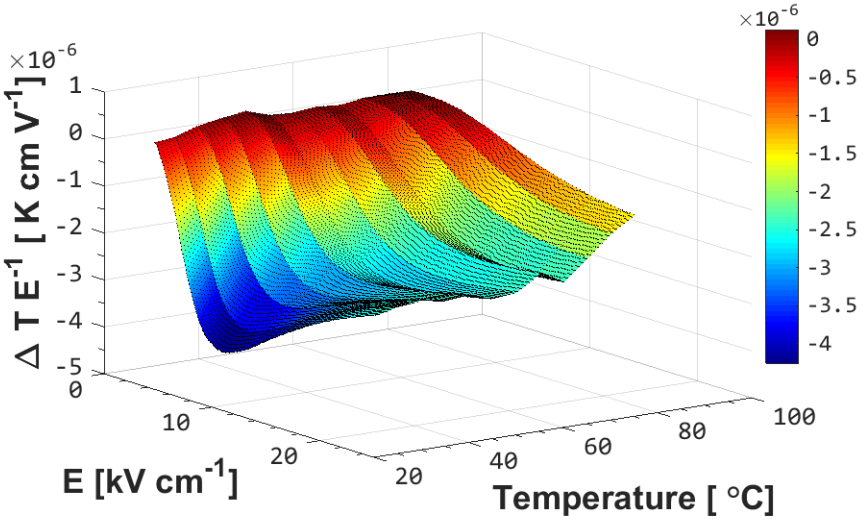

(b)

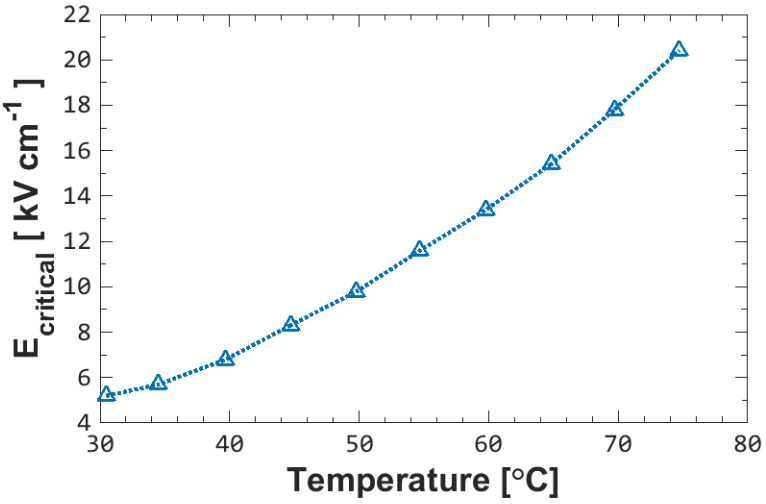

Figure 7.17: Electric field criticality of PMN-PT (a) as a field normalised temperature change with respect to temperature and electric field, and (b) extracted value of critical field as a function of temperature.

7.8.4 Secondary contributions to the electrocaloric effect

The electrocaloric effect primarily originates from dipole moment changes at constant strain resulting in the corresponding temperature change of such body. However, such a body under electric field will also undergo deformation. This can be followed on the Heckmann diagram as the $E \rightarrow u \rightarrow S$ (for more details see Section 2.3.1). Hence the isothermal electrocaloric entropy change expanded with a secondary contribution and can

be found below in equation [2]:

$$\Delta S_{T,\sigma} = \int_{E_1}^{E_2} \left(\frac{\partial P}{\partial T}\right)_{T,\epsilon} \mathrm{d}E + s \int_{E_1}^{E_2} \left(\frac{\partial \epsilon}{\partial T}\right)_{E,T} \left(\frac{\partial \epsilon}{\partial E}\right)_{T,\sigma} \mathrm{d}E \tag{7.2}$$

where the additional term consists of the $s = \frac{\partial \sigma}{\partial \epsilon}$ – elastic stiffness and components under integral are subsequently the Maxwell relations given in eq. 2.9 and 2.10, which are simply the piezoelectric coefficient d and thermal expansion α, respectively.
These parameters are estimated in a subsequent paragraph and further are utilised to calculate the secondary contribution.

Coefficients estimation

Piezoelectric d_{33}[3] and thermal expansion α coefficients were estimated using the strain dataset shown in Figure 7.14 and equations 2.9 and 2.10. Figures 7.18 (a) and (b) show the dependence of these parameters with respect to the temperature, which are selected for three different temperatures, representing different regimes of the PMN-PT phase diagram: (I) 30 °C, relaxor phase (II) 60 °C, vicinity of the phase transition and (III) 115 °C, paraelectric phase.
The calculated d_{33} largely depends on the electric field for temperatures < 70 °C and presents a maximum at the critical electric field. The peak value of d_{33} displays its largest value of $\approx 11 \times 10^{-10}\ m\,V^{-1}$ at 30 °C and diminishes to $\approx 2 \times 10^{-10}\ m\,V^{-1}$ at the maximum field of 21 $kV\,cm^{-1}$. The position of the peak value of d_{33} decreases and shifts towards higher fields with rising temperature and reaches the lowest value of $\approx 2 \times 10^{-10}\ m\,V^{-1}$. Figure 7.18 (b) shows the dependence of the electric field on the calculated thermal expansion α. The change of almost an order of magnitude, from $-1{\times}10^{-5}$ to $-1{\times}10^{-6}\ °C^{-1}$ is observed at 30 °C for 0 and $\approx 4\ kV\,cm^{-1}$, respectively. The critical field of which the existence of the α peak values is shifted with the temperature highlighting strong dependence on both the temperature and the electric field. When scaling up with the temperature the extreme value of α appears at higher electric fields

[3] '$_{33}$' notation indicates z-axis along which displacement is measured and same axis electric field is applied.

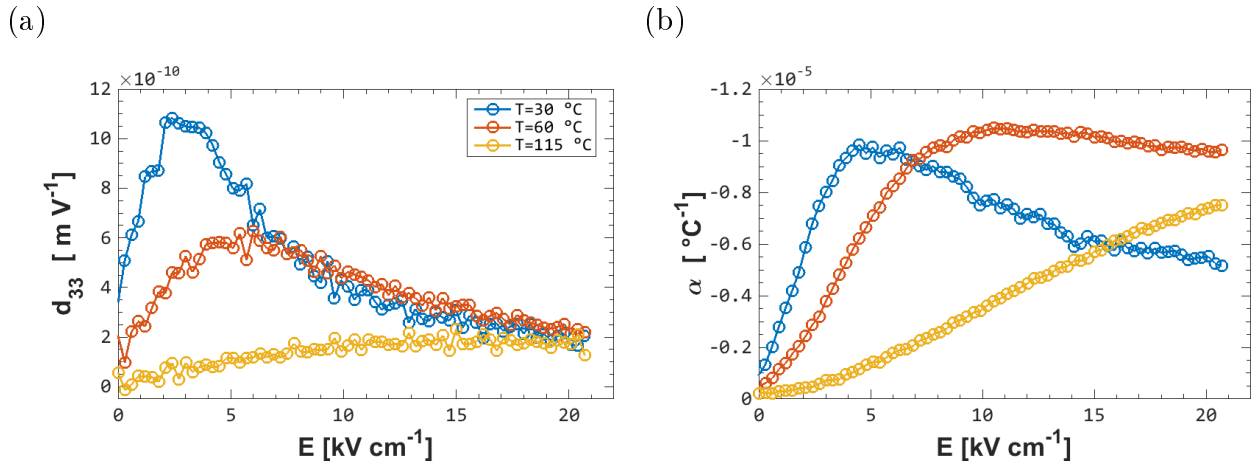

Figure 7.18: Computed (a) piezoelectric coefficient d_{33} and (b) thermal expansion α for PMN-PT ceramic as a function of electric field E at selected temperatures.

and reaches it highest applied value of 21 $kV\,cm^{-1}$ at the phase transition temperature around 75 °C. At that point the maximal value of the thermal expansion is equal to -1.1×10^{-6} $°C^{-1}$. Above this point, the critical behaviour vanishes and the non-linearity reduces. From around 115 °C the thermal expansion becomes linear and gradually with higher temperatures drops its value below the -0.6×10^{-6} $°C^{-1}$.

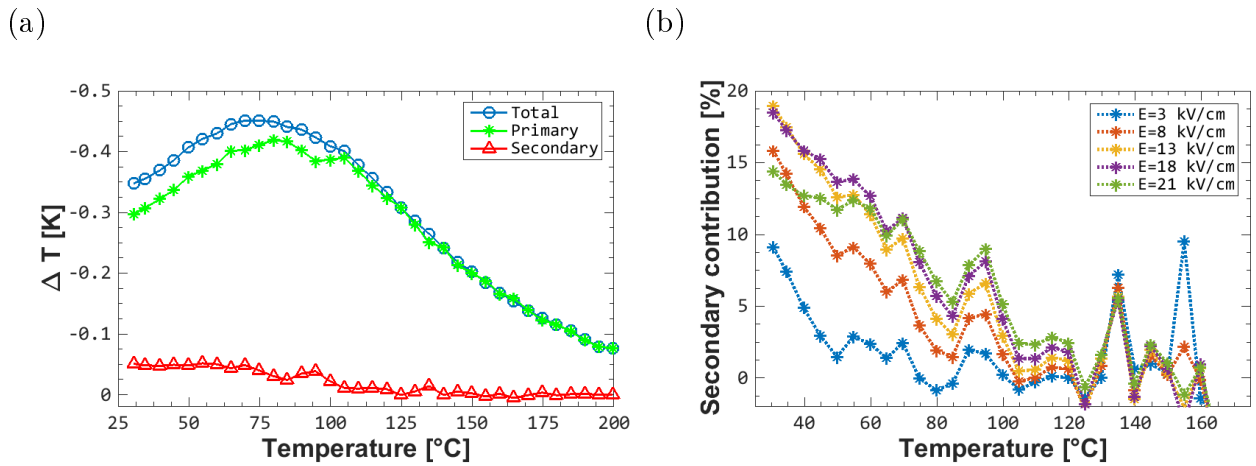

Figure 7.19: The secondary contribution (a) displayed as the primary (green asterisk), secondary (red triangles) and total (blue circles) electrocaloric effect ΔT as a function of the temperature estimated at the highest applied electric field of 21 $kV\,cm^{-1}$ and (b) as a percentage of its contribution to total electrocaloric effect with respect to temperature for the selected electric fields.

Contribution to electrocaloric effect

Returning to the secondary contribution, the rate was calculated based on estimated values of electrocaloric effect as briefly shown in Section 7.8.3. Figure 7.19 (a) shows the estimated ECE for the highest applied electric field of 21 $kV\,cm^{-1}$ marked with the blue circles and its separation into two sources; the primary source (green asterisks) and secondary source (red triangles). The secondary cause of ΔT has the highest magnitude at the lower temperature region up to 100 °C and above this temperature its contribution diminishes and eventually becomes close to zero. The local peaks of primary electrocaloric effect are visible especially at around 80–85 °C and 95 °C, for primary and secondary temperature changes, respectively. However, due to coarse spacing of the temperature sampling every 5 °C and the number of numerical operations based on data (including the noise on the measured values) it is difficult to determine the quality of these peaks. Figure 7.19 (b) shows the relative value of the secondary to primary ΔT contribution expressed in percentiles. A maximum of 19% is observed at 30 °C for the medium range of fields, between 8–18 $kV\,cm^{-1}$. For the highest electric field of 21 $kV\,cm^{-1}$ the ratio reaches the highest magnitude at $T > 75$ °C when compared to lower fields. The significance of the secondary ΔT effects gradually decreases with the temperature of 80 °C with a pronounced local peak around 90 °C, which is more visible than in Figure 7.19 (a). Due to the low magnitude of the secondary activities over 120 °C the noise to signal ratio and the sensitivity (as $\Delta T_{EC,Secondary} \longrightarrow 0$) of the normalisation becomes a significant factor. Thus the ratio between primary and secondary contributions of ΔT is scattered as displayed at the 125–160 °C region, and not shown for higher values.

7.9 Discussion

One of the main challenges in relaxor materials, apart from polar nano regions, is the pseudocubic crystals configuration which allows three different monoclinic transitions resulting in high anisotropy in principal properties, strongly coupled to the electric field

[157].

Direct measurements

Directly measured ECE displayed small values of ΔT_{EC}, due to the low applied electric field which was less than 10 $kV\,cm^{-1}$. Unfortunately, the breakdown of specimens prevents further investigations. Issues such an ageing, fatigue or as in our case, dielectric breakdown seems to be quite common in the electrocaloric community, both based on the author's experience and in communications with Gael Sebald (Private communication February 2016, at the The Royal Society event: 'Taking the temperature of phase transitions in cool materials').

Indirect estimation and electrocaloric strength

Indirect estimation is usually treated qualitatively especially in the relaxor family, however, recent work has shown that at sufficiently low frequency of P–E loops, quantitative values could be obtained [41]. The high coupling to the electrical field in the PMN-PT is verified. The shift of the peak values of either, entropy or temperature change, with an increase of applied field shifts it position towards the higher temperatures and stops at around 75 °C. Such behaviour has been reported before, as the double-peak behaviour, for rather thinner samples and for much greater E-fields [51].

For calculation of the temperature change ΔT, a constant Cp was used. The heat capacity in ferroelectric materials and especially in relaxors should be dependent on both electric field and temperature which has been reported in the literature (for more details see 2.3.2). Therefore the constant value of Cp is not the best approach and may affect results, and prevents the observation of additional anomalies in temperature plots. The peak values of the secondary contribution has been found at the lowest temperature and corresponded to almost 20% of total value, and roughly around $5-10\%$ for the medium to high fields at the broad temperature of around 60–90 °C. Additionally, one can consider an external

parameter (pressure or strain), which could be utilised to tune the ECE peak e.g. shift or broaden the phase transition.

Another important aspect of non-linear behaviour is the strength of the ECE in relaxor materials. When the ECE is normalised to its direct 'force', namely the $\frac{\Delta T}{\Delta E}$, the rate at which effect is delivered can be obtained. This relation is quite often reported as quality figure (figure of merit), which defines a material's ability to exhibit ECE, and can be seen throughout reviews e.g. [20]. In this case, the EC strength varies for the highest magnitude at low temperature is around $-4 \times 10^{-6}\ K\,cm^{-1}$, which is almost twice that than when calculated at the maximum ΔT_{EC} magnitude estimated via the indirect method. This signals existence of an internal resistance, with optimal performance outside of the maximal values (electric field and temperature). This two dimensional non-linear strength parameter, is shown in Figure 7.17. In general, for the region of interest where $\Delta T \geq 80\%\ \Delta T_{max}$ the temperature span is around 35–115 °C. In this region a strength parameter reduces with the rise of temperature and increases with applied electric field. Also, a monotonic increase of the critical electric field value, where the maximum of the strength parameter is observed at given temperature, increases up to 75 °C which happens to be the phase transition peak for that field. This agrees with a prediction of a double-peak.The overall magnitudes of EC strength are higher at the low temperatures and drop nearly linearly in comparison with values up to 85 °C, evidence for lower 'efficiency' in electro-thermal coupling.

Secondary contributions to the ΔT

The secondary contribution itself seems to be a vital part of the whole electrocaloric effect. Typically, this is neglected, because of its low values, where usually $< 1\%$ are predicted for non-ferroelectric crystals of the alternative coupling ($E \rightarrow u \rightarrow S$) [30]. The complexity of the relaxors, the strong field interaction, and the field criticality has been observed also in the calculated piezoelectric and thermal expansion coefficients. The complex relation between the primary and secondary causation of the effect and the E-field criticality was

revealed in this thesis.

The negative thermal expansion is related to the pressure dependency of entropy at the level of metastable microstates [158], and has been found in PMN-PT [159]. Another study, predicts this phenomenon is possible in ferroelectric material under high temperatures, with large entropy changes in small volumes as the cubic phase stabilises [160].
The electrocaloric effect exhibits directionality and other simultaneous couplings, as described in the literature background. In contrast to the magnetocaloric effect, where for crystal symmetry reasons directionality will not be present, the secondary effect here was found to contribute up to almost 20%. A similar order of magnitude, of around 26%, for secondary contributions has been estimated for thick film ferroelectric polymer [36]. To the author's knowledge apart from that work, there are no studies on secondary entropy contribution in ECE.
Hypothetically, the mechanical contribution can possess a negative and positive sign, thus a reduction or increase in the effect on the primary values is permitted. By studying this interrelation further, a possible route to enhancing the effect could be achieved.

7.10 Conclusions

The relaxor nature of the specimen was confirmed by dielectric spectroscopy in the range of 1 kHz to 1 MHz. Based on the indirect estimation method of ECE, performed between 30–200 °C, the maximum of the ECE was found to be $\Delta T = 0.45\ K$ at 75 °C under a field of 21 $kV\,cm^{-1}$. The broad phase transition represents 80% the ΔT_{max} value over temperature range of 35–115 °C. For the direct EC measurements the maximum value was $-0.16\ K \pm 0.04\ K$ where the $\pm$ is a reproducibility based on 3 measurements at room temperature was acquired under a field of 9 $kV\,cm^{-1}$. Due to the low values of electric fields the quantified magnitude has been found to be lower than the uncertainty of the measurements, which was equal $\pm 0.2\ K$ ($k = 2$).
Here, a fairly simple method, comparable with Lu et al. [36] has been proposed. Based

on displacement measurements as a function of electric field over temperature span of interest, the additional contribution to ECE has been quantified.

The behaviour of PMN-PT relaxor ceramics has been thoroughly investigated since 2007 by Kutnjak [157] and later on by his group [93, 20] and optimised PMN-PT ceramic has also been implemented in a cooler prototype [91], which justify the importance of studying this materials.

Herein it has been proposed that the ECE possesses an additional ΔT contribution and values, from 1/10th to 1/5th of the overall effect were found. An over- or under-estimation of ECE is possible, due to the directional nature of ferroelectric crystals and was reviewed in Section 2.3.1. This study was based only on a displacement along one axis, and other aspects of transient e.g volumetric changes with respect to any other coupled properties still remain unknown and should be explored in order to understand electrocaloric a full nature of this effect.

Chapter 8

Thesis conclusions

8.1 Summary of thesis achievements

An electrocaloric temperature change test-bench has been set-up at the National Physical Laboratory. The state-of-the art infrared camera was been combined with a ferroelectric tester with uncertainty of 0.11 °C ($k = 1$) shown in the example in Section 4.5.11. The measurement error depends on multiple factors from the such as: environment (i.e. thermal losses), to the sample (i.e. its surface emissivity, Bi ratio[1]) and internal factors (i.e. physics of electrocaloric effect – secondary contribution to ΔT_{EC}).

Calibration of the infrared camera was performed against an state-of-the-art infrared reference standard, providing a traceability to the current temperature standard (the ITS-90). The instrument performed in a linear manner once compared against the reference standard. The apparatus, apart from the offsets to absolute temperature values, is very sensitive to temperature $\pm 8\ mK$ ($k = 1$), provides stability of around 0.1 °C ($k = 1$) for a 20 minutes measurement period with repeatability of < 0.1 °C ($k = 1$). For this kind of instrument, a new type of temperature radiation standard has to be developed in future and appropriate steps have been taken toward this direction. An innovative

[1]Ratio of thermal resistance determined by heat transfer from outside surface to inside (thermal conductivity) of a body.

vertically aligned multiwall carbon nanotube artefact was designed and characterised. This artefact was used to characterise the size-of-source effect in the apparatus and initially allowed us to establish a 2.5% reduction in object size to around 30 μm in diameter. The estimated drop in performance for objects down to pixel size, which here is 5 μm would correspond to a reduction of 4% in magnitude.

The uncertainty budget for an electrocaloric measurement based on non-contact temperature measurement technique has been completed. The measurement error of around 1 °C provided by the manufacturer for absolute value, has been reduced to expanded uncertainty ($k = 2$) of around 0.30 °C with probablity of 95% of confidence interval. This was possible due to the application of differential temperature measurements.
Multiple aspects of uncertainty sources in measurement process have been quantified. The most prominent uncertainties were found to be the emissivity compensation (especially for large ΔT), calibration and short term drift.

The characterisation of 'dummy' resistive samples was employed to the investigate validity of IR measurement in a test environment. The acquired ΔT followed the trends of various temperature sensors supporting the correctness of the acquired data. However, for such sensitive measurements location of the sensor and the means of its acquisition influence the results. The lowest detectable temperature has been found to be around 20 mK close to infrared camera noise. Once the synchronised acquisition is performed, as in the case of the EC sample, the established lowest temperature changes can be as around 10–15 mK close to the sensitivity of the instrument. Further improvements are possible for infrared technique and are mentioned in future work below.

8.2 Inter-laboratory comparison

The comparison of electrocaloric samples has been made between three independent laboratories, employing different apparatus. Interesting findings have been concluded, from the perspective of metrology. The temperature of a surface acquired with infrared

camera should not be directly compared with a DSC 'thermodynamic' values. These temperatures are two different properties. In order to perform a full comparison a thermal model i.e. finite element methods should be employed to simulate thermal gradients through the specimen, heat conduction to sample surrounding and heat accumulation within i.e. connection terminals.

Electrocaloric heat change for two different differential scanning calorimeters measurements were compared. The two-pan model of such calorimeter at Imperial College of London seems to underestimate the electrocaloric heat up to around 10% which arises for the highest electric field, in compare to Calvet 3D differential scanning calorimeter based at Laboratoire national d'essais. Due to these variances and differences in heat capacity correspondingly the estimated temperature change for DSCs expanded the underestimation to 15%. More importantly it has been shown based on current example, the uncertainty for such ΔT_{EC} estimate propagated to $> 20\%$.

8.3 Investigations in commercial samples

The novel approach of micro-size *in-situ* investigation of multilayer ceramic capacitors has been performed. The thermal propagation through the sample has been recognised, due to the infrared technique ability of high spatial and temporal resolved measurements to be carried out. Based on differences in the response of a short scale pulses, we can distinguish thermally inactive layers of capacitor.

Theoretical work has been performed to establish a deeper understanding of EC phenomena. This helps to identify any potential uncertainty related to ECE itself. The secondary contribution has been found to contribute up to 20% of the total temperature change in PMN-PT ceramic. Also, a relatively simple method to estimate the secondary contribution has been presented. Based on the polar properties of ferroelectric materials the mechanical secondary effects, analogous to the pyroelectric effect, are expected to be directional. Hence, the directly measured temperature will exhibit a total effect, which could be easily

increased or reduced be secondary input depending on the direction (sign).

8.4 Future developments

Throughout this work (i.e. characterisation of setup with resistor, in comparison study, MLCC) we see a disadvantage of a hot-plate heater operating at air environment, due to thermal losses and thermal gradients. Hence the examination of ECE in a vacuum atmosphere, where the convective cooling is not present, could improve measurements by introducing closer to adiabatic conditions. However, this may cause problems with ensuring good thermal and electrically non-conductive contact with specimen, which will affect its temperature. The further investigation of measurement conditions aspect could potentially improve the ΔT_{EC} results.

Based on current uncertainty budget the most prominent errors sources e.g. calibration or emissivity error could be reduced. For instance use of calibrated black paint could improve results. This and any further mitigation would improve the quality of obtained temperature maps.

The carbon nanotubes artefact structure and manufacturing process could be optimised to achieve the better artefact. Theoretically smaller sizes, up to few μm for size-of-source effect are possible, same as various kinds of features could expand NPLs calibration capabilities. Furthermore, by integration of the standard resistive temperature detectors (RTDs) into the structure and adequate calibrations to ITS-90, an innovative flat reference sample could be achieved. Such reference could be used for the absolute temperature calibrations and could compromise the limits of a current infrared calibration standards. Producing of uniform larger sample with standard reference RTD could be employed for uniformity of calibration. Due to small focal distances such a calibration facility would be limited on the higher temperature scale and potentially be in a region of from i.e. -40 °C up to 200 °C. This seems to be a reasonable range which would cover the temperature region of interest for electrocaloric applications.

Recent studies show that certain EC materials naturally might exhibit a mechanical origins of large caloric behaviour [48]. This agrees with the mechanical origin secondary contributions in electrocaloric effect as founded in PMN-PT sample. Hence, it is important to detect the origin of the caloric effect, whether the stimulus electric field or mechanical force is the major source, or if the EC material is not exhibiting internal resistance, which due to stress is not reducing the total value. It is suggested that secondary effects should be investigated on a routine basis along with direct measurements. This would allow to understand the nature of ECE in each composition.

Lastly, the infrared technique has the possibility to operate in combination with various external stimulus enabling acquisition of additional information of materials e.g. defect detection correlated with difference in speed of heat diffusion. Thus, the additional techniques types should be in electrocaloric interest are the in group of an active thermography. Lock-in thermography should be investigated in future. This would reduce noise and increase sensitivity below 1 mK. Such an approach potently could be employed to measure a thin films, which due to their structure still are extremely difficult to be measured.

Bibliography

[1] N. A. S. Smith, M. K. Rokosz, and T. M. Correia, "Experimentally validated finite element model of electrocaloric multilayer ceramic structures," *Journal of Applied Physics*, vol. 116, pp. 1–6, July 2014.

[2] T. M. Correia and M. Rokosz, "Investigations of Secondary Contribution to Electrocaloric Effect in Relaxor PMN-PT Ceramic," *Ferroelectrics*, vol. 478, pp. 165–169, April 2015.

[3] T. Buchacher, M. K. Rokosz, R. Dorey, J. Allam, and A. Gregory, "Electrocaloric induced retarded ferroelectric switching," *Applied Physics Letters*, vol. 110, no. 2, p. 22901, 2017.

[4] X. Moya, S. Kar-Narayan, and N. D. Mathur, "Caloric materials near ferroic phase transitions.," *Nature materials*, vol. 13, no. 5, pp. 439–50, 2014.

[5] W. Thomson, "II. On the thermoelastic, thermomagnetic, and pyroelectric properties of matter," *Philosophical Magazine Series 5*, vol. 5, no. 28, pp. 4–27, 1878.

[6] P. Kobeko and J. Kurtschatov, "Dielektrische Eigenschaften der Seignettesalzkristalle (Eng. trans. Dielectric properties of Rochelle salt crystal)," *Zeitschrift für Physik*, vol. 66, no. May 1918, pp. 192–205, 1930.

[7] J. F. Hautzenlaub, *Electric and dielectric behaviour of potassium dihydrogen phosphate*. PhD thesis, Massachusetts Institute of Technology, 1943.

[8] G. G. Wiseman and J. K. J. Kuebler, "Electrocaloric effect in ferroelectric Rochelle salt," *Physical Review*, vol. 192, no. 1930, pp. 2023–2027, 1963.

[9] C. A. Randall, R. E. Newnham and L. Cross, "History of the First Ferroelectric Oxide, BaTiO3." `https://ceramics.org/wp-content/uploads/2009/05/first_ferroelectric_oxide_ba_tio3.pdf`, 2004 (accessed on 07 October 2016). The American Ceramic Society.

[10] B. T. Matthias, "New ferroelectric crystals," *Physical Review*, vol. 75, no. 11, p. 1771, 1949.

[11] B. Matthias and J. Remeika, "Ferroelectricity in the Ilmenite Structure," *Physical Review*, vol. 76, no. 12, pp. 1886–1887, 1949.

[12] G. Shirane, S. Hoshino, and K. Suzuki, "X-Ray Study of the Phase Transition in Lead Titanate," *Physical Review*, vol. 80, no. 6, pp. 1105–1106, 1950.

[13] A. I. Karchevskii and A. I. Karachevskii, "Electrocaloric effect in polycrystaline barium titanate," *Sov. Phys. Solid State (Eng. Translation)*, vol. 3, no. 10, pp. 2249–2254, 1962.

[14] W. N. Lawless and W. N. Lawless, "Specific heat and electrocaloric properties of KTa03 at low temperatures," vol. 16, no. 1, 1977.

[15] P. D. Thacher, "Electrocaloric Effects in Some Ferroelectric and Antiferroelectric Pb(Zr, Ti)O3 Compounds," *Journal of Applied Physics*, vol. 39, no. 4, pp. 1996–2002, 1968.

[16] L. Shebanovs, K. Borman, W. N. Lawless, and A. Kalvane, "Electrocaloric effect in some perovskite ferroelectric ceramics and multilayer capacitors," *Ferroelectrics*, vol. 273, no. April 2013, pp. 137–142, 2002.

[17] Y. V. Sinyavsky, N. D. Pashkov, Y. M. Gorovoy, G. E. Lugansky, and L. Shebanov, "The optical ferroelectric ceramic as working body for electrocaloric refrigeration," *Ferroelectrics*, vol. 90, no. 1, pp. 213–217, 1989.

[18] Y. Sinyavskii, "Electrocaloric refrigerators: A promising alternative to current low-temperature apparatus," *Chemical and Petroleum Engineering*, vol. 31, no. 6, pp. 5–12, 1995.

[19] M. Valant, "Electrocaloric materials for future solid-state refrigeration technologies," *Progress in Materials Science*, vol. 57, pp. 980–1009, July 2012.

[20] T. Correia and Q. Zhang, eds., *Electrocaloric Materials: New Generation of Coolers*, vol. 34 of *Engineering Materials*. Berlin, Heidelberg: Springer Berlin Heidelberg, August 2014.

[21] A. S. Mischenko, Q. Zhang, J. F. Scott, R. W. Whatmore, and N. D. Mathur, "Giant electrocaloric effect in thin-film PbZr(0.95)Ti(0.05)O3.," *Science (New York, N.Y.)*, vol. 311, pp. 1270–1, March 2006.

[22] Y. Liu, J. F. Scott, B. Dkhil, Y. Liu, J. F. Scott, and B. Dkhil, "Direct and indirect measurements on electrocaloric effect: Recent developments and perspectives," *Applied Physics Reviews*, vol. 3, p. 031102, September 2016.

[23] T. M. Correia, J. S. Young, R. W. Whatmore, J. F. Scott, N. D. Mathur, and Q. Zhang, "Investigation of the electrocaloric effect in a PbMg 2/3 Nb 1/3 O3 - PbTiO3 relaxor thin film," *Applied Physics Letters*, vol. 95, no. 18, p. 182904, 2009.

[24] S. G. Lu, B. Rožič, Q. M. Zhang, Z. Kutnjak, X. Li, E. Furman, L. J. Gorny, M. Lin, B. Malič, M. Kosec, R. Blinc, and R. Pirc, "Organic and inorganic relaxor ferroelectrics with giant electrocaloric effect," *Applied Physics Letters*, vol. 97, no. 16, p. 162904, 2010.

[25] B. Peng, H. Fan, Q. Zhang, . Biaolin Peng , Huiqing Fan, Q. Z. *, B. Peng, H. Fan, and Q. Zhang, "A giant electrocaloric effect in nanoscale antiferroelectric and ferroelectric phases coexisting in a relaxor Pb0.8Ba 0.2ZrO3 thin film at room temperature," *Advanced Functional Materials*, vol. 23, no. 111, pp. 2987–2992, 2013.

[26] S. G. Lu, B. Rožič, Q. M. Zhang, Z. Kutnjak, R. Pirc, M. Lin, X. Li, and L. Gorny, "Comparison of directly and indirectly measured electrocaloric effect in relaxor ferroelectric polymers," *Applied Physics Letters*, vol. 97, no. 20, pp. 1–4, 2010.

[27] M. E. Lines and A. M. Glass, *Principles and Applications of Ferroelectrics and Related Materials*, vol. 1. Oxford University Press, February 2001.

[28] M. Ožbolt, A. Kitanovski, J. Tušek, and a. Poredoš, "Electrocaloric refrigeration: Thermodynamics, state of the art and future perspectives," *International Journal of Refrigeration*, vol. 40, pp. 174–188, April 2014.

[29] T. M. Correia, S. Kar-Narayan, J. S. Young, J. F. Scott, N. D. Mathur, R. W. Whatmore, and Q. Zhang, "PST thin films for electrocaloric coolers," *Journal of Physics D: Applied Physics*, vol. 44, p. 165407, April 2011.

[30] J. Nye, *Physical Properties of Crystals: Their Representation by Tensors and Matrices*. Oxford science publications, Clarendon Press, 1985.

[31] G. Heckmann, "Ergebnisse der exakten naturwissenschaften," in *Springer Tracts in Modern Physics* (W. Kilian, ed.), ch. Die Gitter, pp. 100–153, Springer-Verlag, 1925.

[32] Y. Bai, G. P. G.-P. Zheng, and S. Q. S.-Q. Shi, "Kinetic electrocaloric effect and giant net cooling of lead-free ferroelectric refrigerants," *Journal of Applied Physics*, vol. 108, no. 10, p. 104102, 2010.

[33] S. Bhalla, A.S. Cook, W.R. Liu, *Low Frequency Properties of Dielectric Crystals: Piezoelectric, Pyroelectric, and Related Constants*, vol. 29b of *Landolt-Börnstein - Group III Condensed Matter*. Berlin/Heidelberg: Springer-Verlag, 1993.

[34] R. E. Newnham, *Properties of Materials: Anisotropy, Symmetry, Structure*. OUP Oxford, 2005.

[35] M. Botea, A. Iuga, and L. Pintilie, "Giant pyroelectric coefficient determined from the frequency dependence of the pyroelectric signal generated by epitaxial

Pb(Zr0.2Ti 0.8)O3 layers grown on single crystal SrTiO3 substrates," *Applied Physics Letters*, vol. 103, no. 23, pp. 2–6, 2013.

[36] S. G. Lu, B. Rožič, Q. M. Zhang, Z. Kutnjak, and R. Pirc, "Electrocaloric effect in ferroelectric polymers," *Applied Physics A: Materials Science and Processing*, vol. 107, no. 3, pp. 559–566, 2012.

[37] A. Khodayari and S. Mohammadi, "Solid-state cooling line based on the electrocaloric effect.," *IEEE transactions on ultrasonics, ferroelectrics, and frequency control*, vol. 58, pp. 503–8, March 2011.

[38] R. W. Munn, "Thermodynamic and physical properties of solids in electric fields," *Journal of Physics C: Solid State Physics*, vol. 3213, 1973.

[39] Y. Bai, K. Ding, G. P. Zheng, S. Q. Shi, and L. Qiao, "Entropy-change measurement of electrocaloric effect of BaTiO3 single crystal," *Physica Status Solidi (A) Applications and Materials Science*, vol. 209, no. 5, pp. 941–944, 2012.

[40] S. E. Rowley, M. Hadjimichael, M. N. Ali, Y. C. Durmaz, J. C. Lashley, R. J. Cava, and J. F. Scott, "Quantum criticality in a uniaxial organic ferroelectric," *Journal of Physics: Condensed Matter*, vol. 27, p. 395901, oct 2015.

[41] S. Crossley, T. Usui, B. Nair, S. Kar-Narayan, X. Moya, S. Hirose, A. Ando, and N. D. Mathur, "Direct electrocaloric measurement of 0.9Pb(Mg1/3Nb2/3)O3-0.1PbTiO3 films using scanning thermal microscopy," *Applied Physics Letters*, vol. 108, no. 3, p. 032902, 2016.

[42] M. M. Vopson, "Theory of giant-caloric effects in multiferroic materials," *Journal of Physics D: Applied Physics*, vol. 46, p. 345304, August 2013.

[43] T. Strässle, a. Furrer, Z. Hossain, and C. Geibel, "Magnetic cooling by the application of external pressure in rare-earth compounds," *Physical Review B*, vol. 67, no. 5, p. 054407, 2003.

[44] S. Yuce, M. Barrio, B. Emre, E. Stern-Taulats, A. Planes, J. L. Tamarit, Y. Mudryk, K. A. Gschneidner, V. K. Pecharsky, and L. Mañosa, "Barocaloric effect in the magnetocaloric prototype Gd 5Si 2Ge 2," *Applied Physics Letters*, vol. 101, no. 7, 2012.

[45] E. Bonnot, R. Romero, L. Mañosa, E. Vives, and A. Planes, "Elastocaloric effect associated with the martensitic transition in shape-memory alloys," *Physical Review Letters*, vol. 100, no. 12, pp. 1–4, 2008.

[46] E. A. Pieczyska, S. P. Gadaj, W. K. Nowacki, and H. Tobushi, "Phase-Transformation Fronts Evolution for Stress- and Strain-Controlled Tension Tests in TiNi Shape Memory Alloy," *Experimental Mechanics*, vol. 46, no. 4, pp. 531–542, 2006.

[47] I. Shephered and G. Feher, "Cooling by adiabatic depolorization of OH- molecules in KCl+," *Physical Review Letters*, vol. 15, no. 5, pp. 194–198, 1965.

[48] Y. Liu, J. Wei, P.-E. E. Janolin, I. C. Infante, X. Lou, and B. Dkhil, "Giant room-temperature barocaloric effect and pressure-mediated electrocaloric effect in BaTiO3 single crystal," *Applied Physics Letters*, vol. 104, pp. 2012–2017, April 2014.

[49] Y. Liu, J. Wei, X. Lou, L. Bellaiche, J. F. Scott, and B. Dkhil, "Influence of epitaxial strain on elastocaloric effect in ferroelectric thin films," *Applied Physics Letters*, vol. 106, no. 3, pp. 4–9, 2015.

[50] S. Crossley, N. D. Mathur, and X. Moya, "New developments in caloric materials for cooling applications," *AIP Advances*, vol. 5, no. 6, 2015.

[51] R. Pirc, Z. Kutnjak, R. Blinc, and Q. M. Zhang, "Electrocaloric effect in relaxor ferroelectrics," *Journal of Applied Physics*, vol. 110, no. 7, p. 074113, 2011.

[52] M. Ožbolt, A. Kitanovski, J. Tušek, and A. Poredoš, "Electrocaloric vs. magnetocaloric energy conversion," *International Journal of Refrigeration*, vol. 37, pp. 16–27, January 2014.

[53] Z. Kutnjak, B. Rožič, and R. Pirc, *Electrocaloric Effect: Theory, Measurements, and Applications*, pp. 1–19. John Wiley and Sons, Inc., 2015.

[54] V. K. Pecharsky and K. A. Gschneidner, Jr., "Giant Magnetocaloric Effect in Gd5(Si2Ge2)," *Physical Review Letters*, vol. 78, no. 23, pp. 4494–4497, 1997.

[55] K. M. Rabe, C. H. Ahn, J. M. M. Triscone, M. Dawber, and C. Lichtensteiger, *Physics of Ferroelectrics*, vol. 105. 2007.

[56] J. Valasek, "Piezo-electric and allied phenomena in Rochelle salt," *Physical Review*, vol. 17, no. 4, pp. 475–481, 1921.

[57] V. Sharma, G. Pilania, G. A. Rossetti, K. Slenes, and R. Ramprasad, "Comprehensive examination of dopants and defects in BaTiO3 from first principles," *Physical Review B*, vol. 87, no. 13, p. 134109, 2013.

[58] X. Q. Liu, T. T. Chen, Y. J. Wu, and X. M. Chen, "Enhanced electrocaloric effects in spark plasma-sintered Ba0.65 Sr0.35 TiO3-based ceramics at room temperature," *Journal of the American Ceramic Society*, vol. 96, no. 4, pp. 1021–1023, 2013.

[59] Y. Zhang, X. L. Zhong, M. Vopson, J. B. Wang, and Y. C. Zhou, "Thermally activated polarization dynamics under the effects of lattice mismatch strain and external stress in ferroelectric film," *Journal of Applied Physics*, vol. 112, no. 1, p. 014112, 2012.

[60] B. Li, X. Zhang, J. Wang, X. Zhong, F. Wang, and Y. Zhou, "Giant electrocaloric effect of PbTiO3 thin film tuned in a wide temperature range by the anisotropic misfit strain," *Mechanics Research Communications*, vol. 55, pp. 40–44, January 2014.

[61] M. Vrabelj, H. Uršič, Z. Kutnjak, B. Rožič, S. Drnovšek, A. Benčan, V. Bobnar, L. Fulanović, and B. Malič, "Large electrocaloric effect in grain-size-engineered 0.9Pb(Mg1/3Nb2/3)O3-0.1PbTiO3," *Journal of the European Ceramic Society*, vol. 36, no. 1, pp. 75–80, 2016.

[62] A. A.-B. M. A. Ibrahim, R. Murgan, M. Rahman, J. Osman, M. K. Abd Rahman, and J. Osman, "Morphotropic Phase Boundary in Ferroelectric Materials," *Ferroelectrics - Physical Effects*, August 2011.

[63] X. S. Qian, S. G. Lu, X. Li, H. Gu, L. C. Chien, and Q. Zhang, "Large electrocaloric effect in a dielectric liquid possessing a large dielectric anisotropy near the isotropic-nematic transition," *Advanced Functional Materials*, vol. 23, no. 22, pp. 2894–2898, 2013.

[64] P. F. Liu, J. L. Wang, X. J. Meng, J. Yang, B. Dkhil, and J. H. Chu, "Huge electrocaloric effect in langmuir-blodgett ferroelectric polymer thin films," *New Journal of Physics*, vol. 12, 2010.

[65] E. C. Subbarao, "Ferroelectric and antiferroelectric materials," *Ferroelectrics*, vol. 5, no. 1, pp. 267–280, 1973.

[66] J. Scott, "Electrocaloric Materials," *Annual Review of Materials Research*, vol. 41, pp. 229–240, August 2011.

[67] S. Kar-Narayan, S. Crossley, X. Moya, V. Kovacova, J. Abergel, a. Bontempi, N. Baier, E. Defay, and N. D. Mathur, "Direct electrocaloric measurements of a multilayer capacitor using scanning thermal microscopy and infra-red imaging," *Applied Physics Letters*, vol. 102, no. 3, pp. 4–7, 2013.

[68] B. Kwon, I.-J. J. Roh, S.-H. H. Baek, S. Keun Kim, J.-S. S. Kim, and C.-Y. Y. Kang, "Dynamic temperature response of electrocaloric multilayer capacitors," *Applied Physics Letters*, vol. 104, p. 213902, May 2014.

[69] Y. Liu, B. Dkhil, and E. Defay, "Spatially Resolved Imaging of Electrocaloric Effect and the Resultant Heat Flux in Multilayer Capacitors," *ACS Energy Letters*, p. acsenergylett.6b00232, 2016.

[70] N. Novak, R. Pirc, and Z. Kutnjak, "Impact of critical point on piezoelectric and electrocaloric response in barium titanate," *Physical Review B - Condensed Matter and Materials Physics*, vol. 87, no. 10, pp. 1–5, 2013.

[71] X. Moya, E. Stern-Taulats, S. Crossley, D. Gonzàlez-Alonso, S. Kar-Narayan, A. Planes, L. Mañosa, and N. D. Mathur, "Giant electrocaloric strength in single-crystal BaTiO3," *Advanced Materials*, vol. 25, no. 9, pp. 1360–1365, 2013.

[72] N. Novak, Z. Kutnjak, and R. Pirc, "High-resolution electrocaloric and heat capacity measurements in barium titanate," *EPL (Europhysics Letters)*, vol. 103, no. 4, p. 47001, 2013.

[73] M. Sanlialp, V. V. Shvartsman, D. C. Lupascu, C. Molin, and S. Gebhardt, "Direct electrocaloric measurements using a differential scanning calorimeter," in *2015 Joint IEEE International Symposium on the Applications of Ferroelectric, International Symposium on Integrated Functionalities and Piezoelectric Force Microscopy Workshop, ISAF/ISIF/PFM 2015*, pp. 159–162, 2015.

[74] K. Ding and G. P. Zheng, "Scaling for the refrigeration effects in lead-free barium titanate based ferroelectric ceramics," *Journal of Electroceramics*, vol. 32, no. 2-3, pp. 169–174, 2014.

[75] Y. Bai, G.-P. P. Zheng, and S.-Q. Q. Shi, "Abnormal electrocaloric effect of Na0.5Bi0.5TiO 3-BaTiO3 lead-free ferroelectric ceramics above room temperature," *Materials Research Bulletin*, vol. 46, pp. 1866–1869, November 2011.

[76] M. Davis, "Picturing the elephant: Giant piezoelectric activity and the monoclinic phases of relaxor-ferroelectric single crystals," *Journal of Electroceramics*, vol. 19, no. 1, pp. 23–45, 2007.

[77] S. W. Choi, R. T. R. Shrout, S. J. Jang, and A. S. Bhalla, "Dielectric and pyroelectric properties in the Pb(Mg 1/3 Nb 2/3)O 3 -PbTiO 3 system," *Ferroelectrics*, vol. 100, pp. 29–38, December 1989.

[78] Z. G. Ye, "Relaxor ferroelectric complex perovskites: Structure, properties and phase transitions," *Key Engineering Materials*, vol. 155-156, pp. 81–122, 1998.

[79] J. Zhao, Q. M. Zhang, N. Kim, and T. Shrout, "Electromechanical properties of relaxor ferroelectric lead magnesium niobate-lead titanate ceramics," *Japanese Journal of Applied Physics*, vol. 34, no. 10, pp. 5658–5663, 1995.

[80] V. A. Shuvaeva, A. M. Glazer, and D. Zekria, "The macroscopic symmetry of Pb(Mg 1/3 Nb 2/3) 1-x Ti x O 3 in the morphotropic phase boundary region (x = 0.25-0.5)," *Journal of Physics: Condensed Matter*, vol. 17, pp. 5709–5723, September 2005.

[81] B. Noheda, J. Gonzalo, L. Cross, and R. Guo, "Tetragonal-to-monoclinic phase transition in a ferroelectric perovskite: The structure of PbZr0.52 Ti0.48 O3," *Physical Review B*, vol. 61, no. 13, pp. 8687–8695, 2000.

[82] T. M. P. Correia, *Exploring Electrocaloric Effect in Thin Films.* PhD thesis, Cranfield University - School of Applied Sciences, 2010.

[83] A. A. Bokov and Z. G. Ye, "Recent progress in relaxor ferroelectrics with perovskite structure," *Journal of Materials Science*, vol. 41, no. 1, pp. 31–52, 2006.

[84] L. J. Dunne, M. Valant, A.-K. Axelsson, G. Manos, and N. McN Alford, "Statistical mechanical lattice model of the dual-peak electrocaloric effect in ferroelectric relaxors and the role of pressure," *J. Phys. D: Appl. Phys. J. Phys. D: Appl. Phys*, vol. 44, no. 44, pp. 375404–5, 2011.

[85] Z. Kutnjak, J. Petzelt, and R. Blinc, "The giant electromechanical response in ferroelectric relaxors as a critical phenomenon.," *Nature*, vol. 441, no. 7096, pp. 956–959, 2006.

[86] H. Hagberg, Juha ; Uusimäki, Antti ; Jantunen, J. Hagberg, A. Uusimäki, and H. Jantunen, "Electrocaloric characteristics in reactive sintered 0.87 Pb(Mg1/3Nb2/3)O3–0.13PbTiO3," *Applied Physics Letters*, vol. 92, no. 13, p. 132909, 2008.

[87] L. Shebanovs, K. Borman, W. N. Lawless, and a. Kalvane, "Electrocaloric Effect in Some Perovskite Ferroelectric Ceramics and Multilayer Capacitors," *Ferroelectrics*, vol. 273, pp. 137–142, January 2002.

[88] C. A. Randall, A. S. Bhalla, T. R. Shrout, and L. E. Cross, "Classification and consequences of complex lead perovskite ferroelectrics with regard to B-site cation order," *Journal of Materials Research*, vol. 5, no. 4, pp. 829–834, 1990.

[89] G. Xu, Z. Zhong, Y. Bing, Z.-G. Ye, and G. Shirane, "Electric-field-induced redistribution of polar nano-regions in a relaxor ferroelectric.," *Nat. Mater.*, vol. 5, no. February, pp. 134–140, 2006.

[90] R. Pirc and R. Blinc, "Spherical random-bond–random-field model of relaxor ferroelectrics," *Physical Review B*, vol. 60, no. 19, pp. 13470–13478, 1999.

[91] U. Plaznik, A. Kitanovski, B. Rožič, B. Malič, H. Uršič, S. Drnovšek, J. Cilenšek, M. Vrabelj, A. Poredoš, and Z. Kutnjak, "Bulk relaxor ferroelectric ceramics as a working body for an electrocaloric cooling device," *Applied Physics Letters*, vol. 106, p. 043903, January 2015.

[92] R. Zhang, S. Peng, D. Xiao, Y. Wang, B. Yang, J. Zhu, P. Yu, and W. Zhang, "Preparation and Characterization of (1 -x)Pb(Mg1/3Nb2/3)O3 - x PbTiO3 Electrocaloric Ceramics," *Crystal Research and Technology*, vol. 33, no. 5, pp. 827–832, 1998.

[93] B. Rožič, M. Kosec, H. Uršič, J. Holc, B. Malič, Q. M. Zhang, R. Blinc, R. Pirc, and Z. Kutnjak, "Influence of the critical point on the electrocaloric response of relaxor ferroelectrics," *Journal of Applied Physics*, vol. 110, no. 6, p. 064118, 2011.

[94] S. Hirose, T. Usui, S. Crossley, B. Nair, A. Ando, X. Moya, and N. D. Mathur, "Progress on electrocaloric multilayer ceramic capacitor development," *APL Materials*, vol. 4, no. 6, p. 064105, 2016.

[95] A. A. Bokov and Z.-G. Ye, "Dielectric Relaxation in Relaxor Ferroelectrics," *Journal of Advanced Dielectrics*, vol. 02, no. 02, p. 1241010, 2012.

[96] S. Lisenkov and I. Ponomareva, "Intrinsic electrocaloric effect in ferroelectric alloys from atomistic simulations," *Physical Review B*, vol. 80, p. 140102, oct 2009.

[97] S. G. Lu, B. Rožič, Q. M. Zhang, Z. Kutnjak, and B. Neese, "Enhanced electrocaloric effect in ferroelectric poly(vinylidene-fluoride/trifluoroethylene) 55/45 mol % copolymer at ferroelectric-paraelectric transition," *Applied Physics Letters*, vol. 98, no. 12, p. 122906, 2011.

[98] Z. Luo, D. Zhang, Y. Liu, D. Zhou, Y. Yao, C. Liu, B. Dkhil, X. Ren, and X. Lou, "Enhanced electrocaloric effect in lead-free BaTi1-xSnx03 ceramics near room temperature," *Applied Physics Letters*, vol. 105, p. 102904, September 2014.

[99] X.-C. Zheng, G.-P. Zheng, Z. Lin, and Z.-Y. Jiang, "Electro-caloric behaviors of lead-free Bi0.5Na0.5TiO3-BaTiO3 ceramics," *Journal of Electroceramics*, vol. 28, pp. 20–26, December 2012.

[100] B. A. Strukov, S. A. Taraskin, and V. M. Varikash, "Thermal and electrocaloric properties of ferroelectric triglycine selenate near the Currie point," *Fizika Tverdogo Tela*, vol. 10, no. 6, pp. 1836–1842, 1968.

[101] B. A. Strukov, "Electrocaloric effect in single-crystal triglycine sulfate," *SOVIET PHYSICS CRYSTALLOGRAPHY, USSR*, vol. 11, no. 6, p. 757, 1967.

[102] L. Shebanov and K. Borman, "On lead-scandium tantalate solid solutions with high electrocaloric effect," *Ferroelectrics*, vol. 127, no. June 2013, pp. 143–148, 1992.

[103] M. McGlashan, "The international temperature scale of 1990 (ITS-90)," *The Journal of Chemical Thermodynamics*, vol. 22, pp. 653–663, July 1990.

[104] R. L. Rusby, "Introduction to temperature measurement," *Measurement Good Practice Guide No. 125*, no. 125, 2015.

[105] L. Michalski, K. Eckersdorf, J. Kucharski, and J. McGhee, *Temperature Measurement*, vol. 9. Chichester, UK: John Wiley & Sons, Ltd, November 2001.

[106] R. Park, R. Carroll, G. Burns, R. Desmaris, F. Hall, M. Herzkovitz, D. MacKenzie, E. McGuire, R. Reed, L. Sparks, and T. Wang, *Manual on the Use of Thermocouples in Temperature Measurement, Fourth Edition, Sponsored by ASTM Committee E20 on Temperature Measurement.* ASTM International, January 1993.

[107] "Standard Specification for Mineral-Insulated, Metal-Sheathed Base Metal Thermocouples." `https://doi.org/10.1520/E0608_E0608M`, 2012 (accessed on 9 November 2016).

[108] E. H. Birks, "The electrocaloric effect in Pb(Sc0.5Nb0.5)O3 ceramic," *Physica Status Solidi (a)*, vol. 94, no. 2, pp. 523–527, 1986.

[109] S. Crossley, *Electrocaloric materials and devices.* PhD thesis, King's College, University of Cambridge, 2013.

[110] G. Sebald, L. Seveyrat, J. F. Capsal, P. J. Cottinet, and D. Guyomar, "Differential scanning calorimeter and infrared imaging for electrocaloric characterization of poly(vinylidene fluoride-trifluoroethylene- chlorofluoroethylene) terpolymer," *Applied Physics Letters*, vol. 101, no. 2, pp. 2010–2013, 2012.

[111] P. K. Gallagher and M. E. Brown, eds., *HANDBOOK OF THERMAL ANALYSIS AND CALORIMETRY: Recentes Advances, Techiniques and Applications*, vol. 5. Elsevier, 2008.

[112] Z. Kutnjak, S. Kralj, G. Lahajnar, and S. Zumer, "Thermal study of octylcyanobiphenyl liquid crystal confined to controlled-pore glass," *Fluid Phase Equilibria*, vol. 222-223, pp. 275–281, 2004.

[113] H. Yao, K. Ema, and C. Garland, "Nonadiabatic scanning calorimeter," *Review of scientific instruments*, vol. 69, no. 1998, pp. 172–178, 1998.

[114] B. Rožič, B. Malič, H. Uršič, J. Holc, M. Kosec, S.-G. Lu, Q. M. Zhang, and Z. Kutnjak, "The Giant Electrocaloric Effect in Inorganic and Organic Ferroelectric Relaxor Systems," 2012.

[115] G. Zhang, Q. Li, H. Gu, S. Jiang, K. Han, M. R. Gadinski, M. A. Haque, Q. Zhang, and Q. Wang, "Ferroelectric polymer nanocomposites for room-temperature electrocaloric refrigeration," *Advanced Materials*, vol. 27, no. 8, pp. 1450–1454, 2015.

[116] Q. Li, G. Zhang, X. Zhang, S. Jiang, Y. Zeng, and Q. Wang, "Relaxor Ferroelectric-Based Electrocaloric Polymer Nanocomposites with a Broad Operating Temperature Range and High Cooling Energy," *Advanced Materials*, vol. 27, no. 13, pp. 2236–2241, 2015.

[117] B. Rožič, B. Malič, H. Uršič, J. Holc, M. Kosec, B. Neese, Q. M. Zhang, and Z. Kutnjak, "Direct Measurements of the Giant Electrocaloric Effect in Soft and Solid Ferroelectric Materials," *Ferroelectrics*, vol. 405, pp. 26–31, oct 2010.

[118] "Evaluation of measurement data - Guide to the expression of uncertainty in measurement," tech. rep., Joint Committee For Guides In Metrology, 2008.

[119] G. W. H. Höhne, W. F. Hemminger, and H.-J. Flammersheim, *Differential Scanning Calorimetry*, vol. 53. 2003.

[120] F. L. Goupil, A. Berenov, A.-K. Axelsson, M. Valant, and N. M. Alford, "Direct and indirect electrocaloric measurements on ⟨001⟩-PbMg1/3Nb2/3O3-30PbTiO3 single crystals," *Journal of Applied Physics*, vol. 111, no. 12, p. 124109, 2012.

[121] W. Boettinger, U. Kattner, K.-W. Moon, and J. Perepezko, "DTA and Heat-flux DSC Measurements of Alloy Melting and Freezing," *NIST Special Publication*, vol. 960-15, p. 90, 2006.

[122] G. Sebald, L. Seveyrat, D. Guyomar, L. Lebrun, B. Guiffard, and S. Pruvost, "Electrocaloric and pyroelectric properties of 0.75Pb(Mg 1/3Nb2/3)O3-0.25PbTiO3 single crystals," *Journal of Applied Physics*, vol. 100, no. 2006, pp. 0–6, 2006.

[123] G. Akcay, S. P. Alpay, G. A. Rossetti, and J. F. Scott, "Influence of mechanical boundary conditions on the electrocaloric properties of ferroelectric thin films," *Journal of Applied Physics*, vol. 103, no. 2, 2008.

[124] D. Guo, J. Gao, Y. J. Yu, S. Santhanam, G. K. Fedder, A. J. H. McGaughey, and S. C. Yao, "Electrocaloric characterization of a poly(vinylidene fluoride-trifluoroethylene-chlorofluoroethylene) terpolymer by infrared imaging," *Applied Physics Letters*, vol. 105, no. 3, 2014.

[125] E. Vives, S. Burrows, R. S. Edwards, S. Dixon, L. Maosa, A. Planes, and R. Romero, "Temperature contour maps at the strain-induced martensitic transition of a Cu-Zn-Al shape-memory single crystal," *Applied Physics Letters*, vol. 98, no. 1, pp. 20–23, 2011.

[126] J. Cui, Y. Wu, J. Muehlbauer, Y. Hwang, R. Radermacher, S. Fackler, M. Wuttig, and I. Takeuchi, "Demonstration of high efficiency elastocaloric cooling with large temperature change using NiTi wires," *Applied Physics Letters*, vol. 101, no. 7, pp. 1–5, 2012.

[127] J. Tušek, K. Engelbrecht, L. P. Mikkelsen, and N. Pryds, "Elastocaloric effect of Ni-Ti wire for application in a cooling device," *Journal of Applied Physics*, vol. 117, no. 12, 2015.

[128] S. G. Lu, Z. Fang, E. Furman, Y. Wang, Q. M. Zhang, Y. Mudryk, K. A. Gschneidner, V. K. Pecharsky, and C. W. Nan, "Thermally mediated multiferroic composites for the magnetoelectric materials," *Applied Physics Letters*, vol. 96, no. 10, pp. 2008–2011, 2010.

[129] Y. B. Gianchandani and K. Najafi, "A silicon micromachined scanning thermal profiler with integrated elements for sensing and actuation," *IEEE Transactions on Electron Devices*, vol. 44, no. 11, pp. 1857–1868, 1997.

[130] S. B. Lang and D. K. Das-Gupta, "A technique for determining the polarization distribution in thin polymer electrets using periodic heating," *Ferroelectrics*, vol. 39, no. 1, pp. 1249–1252, 1981.

[131] S. B. Lang and D. K. Das-Gupta, "Laser-intensity-modulation method: A technique for determination of spatial distributions of polarization and space charge in polymer electrets," *Journal of Applied Physics*, vol. 59, no. 6, pp. 2151–2160, 1986.

[132] G. Suchaneck, a. V. Solnyshkin, D. A. Kiselev, A. A. Bogomolov, and G. Gerlach, "The LIMM problem for ferroelectric thin films comprising space charge layers," *Journal of the European Ceramic Society*, vol. 25, no. 12 SPEC. ISS., pp. 2363–2368, 2005.

[133] A. A. Movchikova, G. Suchaneck, O. V. Malyshkina, and G. Gerlach, "Characterization of ferroelectrics by thermal wave methods," *Journal of the European Ceramic Society*, vol. 27, no. 13-15, pp. 4007–4010, 2007.

[134] G. Gerlach, G. Suchaneck, A. Movchikova, and O. Malyshkina, "Nondestructive testing of ferroelectrics by thermal wave methods," in *The International Society for Optical Engineering* (K. J. Peters, ed.), p. 65300B, Apr 2007.

[135] M. Stewart and M. Cain, "Use of scanning limm (laser intensity modulation method) to characterise polarisation variability in dielectric materials," *Journal of Physics: Conference Series*, vol. 183, no. 1, p. 012001, 2009.

[136] A. Kleiner, G. Suchaneck, A. Eydam, G. Gerlach, and L. Liu, "Reactively sputtered pmn-pt thin films for electrocaloric applications," in *2014 Joint IEEE International Symposium on the Applications of Ferroelectric, International Workshop on Acoustic Transduction Materials and Devices Workshop on Piezoresponse Force Microscopy*, pp. 1–4, May 2014.

[137] T. Sandner, G. Suchaneck, and R. Koehler, "Integrated Ferroelectrics: An High Frequency LIMM - A Powerful Tool for Ferroelectric Thin Film Characterization," no. December 2014, pp. 37–41, 2002.

[138] A. Kleiner, G. Suchaneck, A. Eydam, G. Gerlach, L. Liu, A. Günther, and N. Neumann, "Mn-doped pmn-pt thin films for electrocaloric applications," in *2015 Joint IEEE International Symposium on the Applications of Ferroelectric (ISAF),*

International Symposium on Integrated Functionalities (ISIF), and Piezoelectric Force Microscopy Workshop (PFM), pp. 200–202, May 2015.

[139] M. Dawber, K. M. Rabe, and J. F. Scott, "Physics of thin-film ferroelectric oxides," *October*, vol. 77, no. October, pp. 1083–1130, 2005.

[140] X. Li, S.-G. Lu, X.-Z. Chen, H. Gu, X.-s. Qian, and Q. M. Zhang, "Pyroelectric and electrocaloric materials," *Journal of Materials Chemistry C*, vol. 1, no. 1, p. 23, 2013.

[141] P. De Bièvre, "The 2012 international vocabulary of metrology: "vim"," *Accreditation and Quality Assurance*, vol. 17, no. 2, pp. 231–232, 2012.

[142] A. L. Chun, "Carbon nanotubes: Blacker than black," *Nature Nanotechnology*, January 2008.

[143] G. C. Holst and T. S. Lomheim, *CMOS/CCD Senors and Camera Systems*. JCD Publishing and Spie press, 2007.

[144] P. Saunders, "MSL Technical Guide 26 Size-of-Source Effect in Infrared Thermometers Measuring the SSE during Calibration," tech. rep., Measurement Standards Laboratory of New Zealand, 2012.

[145] D. P. DeWitt, *Applications of Radiation Thermometry: A Symposium, Issue 895*. American Society for Testing and Materials, 1985.

[146] K. Mizuno, J. Ishii, H. Kishida, Y. Hayamizu, S. Yasuda, D. N. Futaba, M. Yumura, and K. Hata, "A black body absorber from vertically aligned single-walled carbon nanotubes.," *Proceedings of the National Academy of Sciences of the United States of America*, vol. 106, no. 15, pp. 6044–6047, 2009.

[147] N. G. Shang, Y. Y. Tan, V. Stolojan, P. Papakonstantinou, and S. R. P. Silva, "High-rate low-temperature growth of vertically aligned carbon nanotubes.," *Nanotechnology*, vol. 21, no. 50, p. 505604, 2010.

[148] C. R. Nave, "Coma and Astigmatism." Online source `http://hyperphysics.phy-astr.gsu.edu/hbase/geoopt/coma.html`, 2009 (accessed on 15 November 2016).

[149] A. Whittam, R. Simpson, and H. McEvoy, "Performance tests of thermal imaging systems to assess their suitability for quantitative temperature measurement," in *Proceedings of the 2014 International Conference on Quantitative InfraRed Thermography*, pp. 5–7, QIRT Council, 2014.

[150] "The added value of 3d sensors." Online source `http://www.setaram.com/`2d-plate-shaped-or-cylindrical-3d-calvet-sensor-uncertainty-propagation-or-accuracy-propagatic (accessed on 11 August 2016). SETARAM Instrumentation, technical note.

[151] A. Berenov, F. Le Goupil, and N. Alford, "Effect of ionic radii on the Curie temperature in Ba1-x-ySrxCayTiO3 compounds," *Scientific Reports*, vol. 6, p. 28055, 2016.

[152] M. Marathe, A. Grünebohm, T. Nishimatsu, P. Entel, and C. Ederer, "First principles-based calculation of the electrocaloric effect in BaTiO3: comparison between direct and indirect methods," *Phys. Rev. B*, vol. 93, p. 054110, February 2016.

[153] "X7R - Syfer." Online source http://www.knowlescapacitors.com/syfer/en/gn/news–events/new-proc accessed on 14 December 2015.

[154] S. Kar-Narayan and N. D. Mathur, "Direct and indirect electrocaloric measurements using multilayer capacitors," *Journal of Physics D: Applied Physics*, vol. 43, p. 032002, January 2010.

[155] S. Kar-Narayan and N. D. Mathur, "Predicted cooling powers for multilayer capacitors based on various electrocaloric and electrode materials," *Applied Physics Letters*, vol. 95, no. 24, p. 242903, 2009.

[156] S. Crossley, J. R. McGinnigle, S. Kar-Narayan, and N. D. Mathur, "Finite-element optimisation of electrocaloric multilayer capacitors," *Applied Physics Letters*, vol. 104, p. 082909, February 2014.

[157] Z. Kutnjak, R. Blinc, and Y. Ishibashi, "Electric field induced critical points and polarization rotations in relaxor ferroelectrics," *Physical Review B - Condensed Matter and Materials Physics*, vol. 76, no. 10, pp. 1–8, 2007.

[158] Z.-K. Liu, Y. Wang, and S. L. Shang, "Thermal Expansion Anomaly Regulated by Entropy," *Scientific Reports*, pp. 1–6, 2014.

[159] Y. Tang, L. Chen, X. Zhao, W. Jin, and H. Luo, "Anisotropic thermal expansion and phase transitions in Pb(Mg1/3Nb2/3)O3-0.3PbTiO3 single crystals," *Physica B: Condensed Matter*, vol. 382, no. 1-2, pp. 205–208, 2006.

[160] Z. K. Liu, Y. Wang, and S. L. Shang, "Origin of negative thermal expansion phenomenon in solids," *Scripta Materialia*, vol. 65, no. 8, pp. 664–667, 2011.

Appendix A

Calibration Facility at NPL

A.1 Facility

Table A.1 presents the example of uncertainty budget for typical calibration including the uncertainty of reference source for the measurement of 60 °C. Based on this assessment performed with the Infratec ImageIR 8320 and according to the procedure developed at NPL to calibrate IR sensors the following results for operating span of 20–200 °C and the reference source uncertainties for individual temperature are shown in Figure A.1.

Table A.1: Uncertainty budget for the H_2O cooled black body reference at 60 °C.

Source of uncertainty	Value [°C]	Probability Distribution	value Divisor	Conversation factor	u [°C]	Numbers of readings
Reference source (k=1)	0.025	N	1	1	0.03	large
Wavelength (μm)	0.01	R	1.732	1	0.01	large
Stability ref source	0.01	N	3.464	1	0.00	12
Stability IRT output	0.01	N	3.464	1	0.00	12
Resolution IRT output	0.01	R	3.464	1	0.00	large
Alignment	0.05	R	1.732	1	0.03	large
Repeatability of calbrtn	0.1	R	1.732	1	0.06	8
Drift allowance	0.1	R	1.732	1	0.06	large
Combined uncertainty		n			0.09	
Expanded uncertainty		n (k=2)			0.18	
Expanded uncertainty		k =	2.061		0.19	
Effective degrees of freedom						42.2
Approximate k_p						2.1

Where N-normal distribution and R- rectangular distribution.

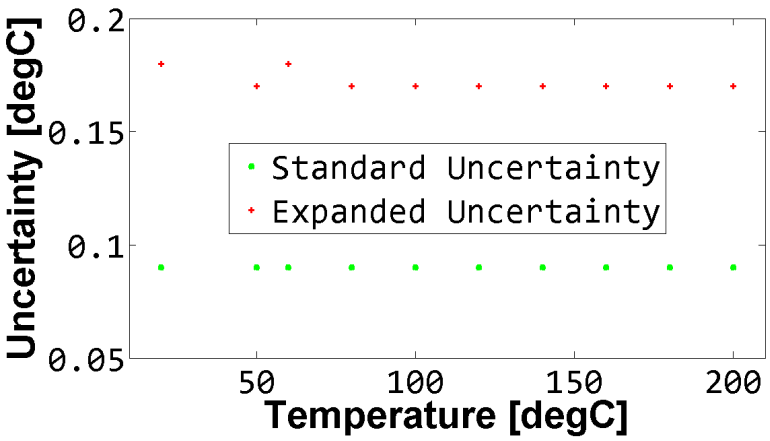

Figure A.1: Uncertainty of NPL's reference black body cavity as a function of temperature used for calibration of infrared imager.

Appendix B

Uncertainty table for electrocaloric effect example

The selected example of full uncertainty budget table is presented in Table B.1.

Table B.1: Full uncertainty budget for measurement of $\Delta T_{apparent} = 1$ °C acquired at 20 °C for the specimen with estimated emissivity $\epsilon = 0.8$.

Source of uncertainty	Value [°C]	Probability Distribution	Conversion Divisor	Numbers Factor	u [°C]	Number of readings
Drift	0.10	R	$\sqrt{3}$	1	0.06	∞
Sensitivity	0.009	N	1.00	1	0.01	200
Alignment	0.10	R	$\sqrt{3}$	0.4	0.02	7
Emissivity compensation	0.04	R	$\sqrt{3}$	1	0.02	∞
Calibration	0.09	N	1.00	1	0.09	8
Combined uncertainty	n			0.11		
Expanded uncertainty	n (k=2)			0.22		
Expanded uncertainty	k=	2.17		0.24		
Effective degrees of freedom					16.8	
Approximate k_p					2.17	

Where N-normal distribution and R- rectangular distribution.

Appendix C

Characterisation of bulk resistor

Resistor calibration

The standard resistor was calibrated in the oven for selected temperatures. The sample under test with soldered copper $\phi = 120\ \mu m$ wire was attached to the 1mm thick $10 \times 10\ mm$ alumna plate with kepton tape. The tape was wrapped around the plate to ensure good contact with larger thermal mass. Moreover the T-type thermocouple was placed on the top of sample with the thermally conductive paste. The resistance was measured with the standard Keithley kelvin probes attached to calibrated Keithley 2001, 7.5 digit digital multimeter (with accuracy $\pm 0.0039\ \Omega$). Temperature was recorded with the Picoscope TC-08 data logger and K-type thermocouple (with accuracy $\pm 0.5\ K$). Fitted results are shown on the Figure C.1.

The heat capacity of the resistor specimen has been acquired in the differential scanning calorimeter, the DSC 200 F3 Maia (Netzsch), for the temperature range 25–200 °C at ICL. The fitted results are shown on the Figure C.2.

Other temperature measurements

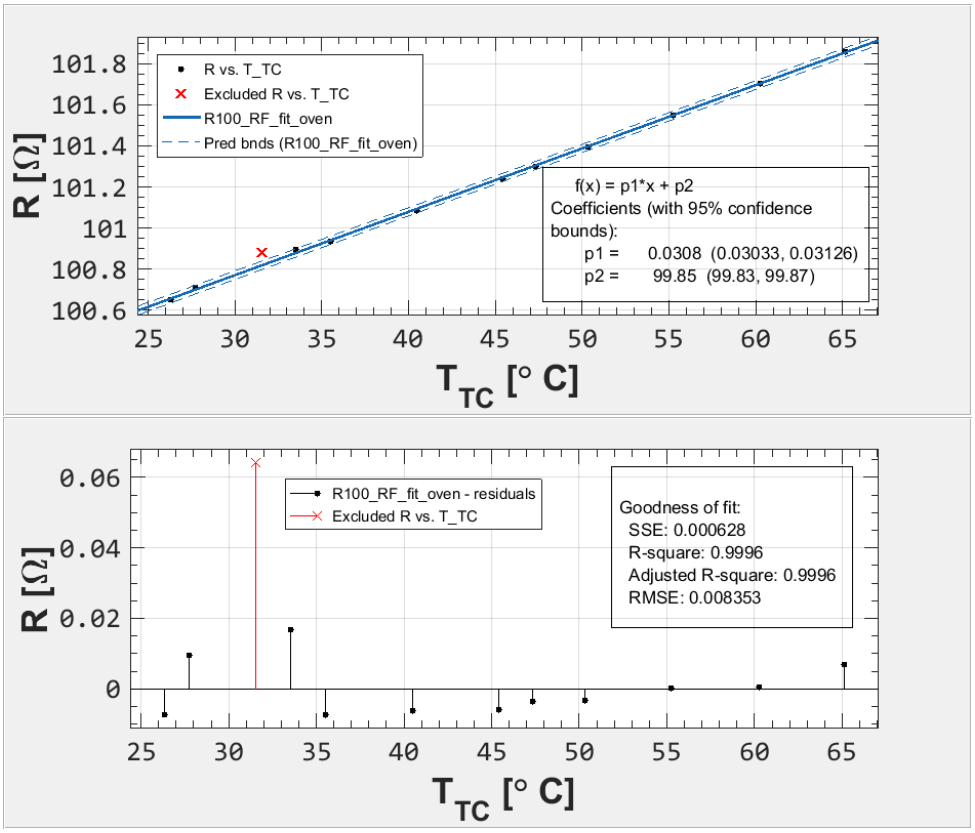

Figure C.1: Fitting of the resistor calibration in oven against the T-type thermocouple.

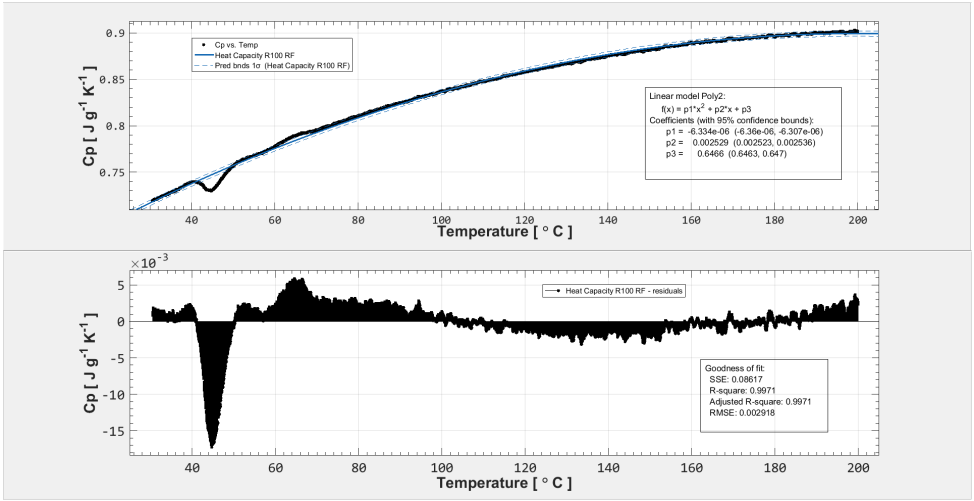

Figure C.2: Fitting of heat capacity of the resistor.

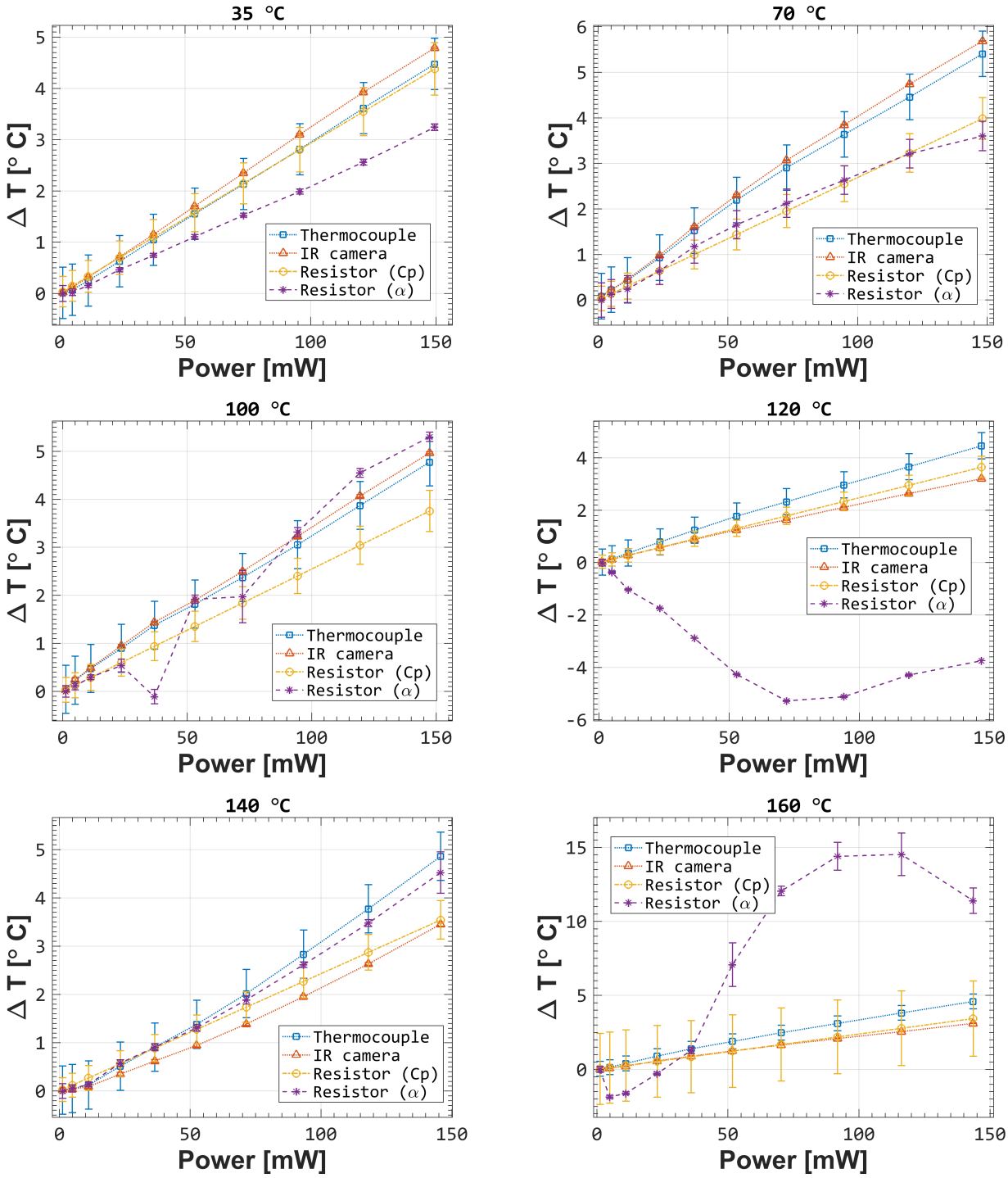

Figure C.3: Characterisation results a the various temperature of surroundings from 35 $^\circ C$ to 160 $^\circ C$, plotted as the acquired temperature change acquired via IR camera, TC and resistor measurements (based on temperature coefficient α and Cp) as a function of delivered power.

Appendix D

Element analysis of X7R capacitor

Supplementary data of energy dispersive X-ray spectroscopy (EDX) analysis taken on the X7R capacitor cross-section with an example of the results shown in Figure D.1 and the detected composition listed in Table D.1.

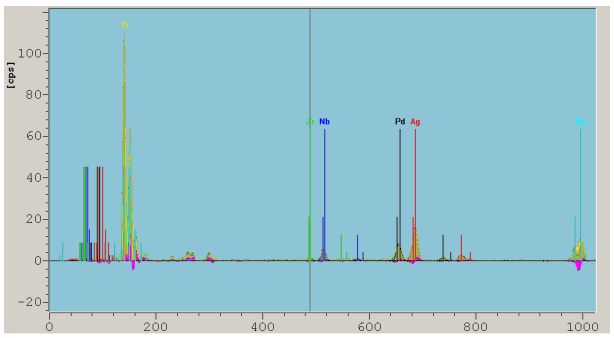

Figure D.1: An example of the EDX results acquired on X7R capacitor.

Table D.1: Results of elements composition analysis on the X7R capacitor dielectric layer and connection terminal.

Elements	Dielectric layer (%)	Terminal (%)
Ag	5.06	53.03
Ba	60.37	2.84
Nb	0.71	0.20
Pd	2.30	0.06
Sn	-	22.25
Ni	-	21.10
Ti	31.70	-
Zr	0.13	0.06

Appendix E

Permissions

The below permission is regarded reproducing graph in Figure 2.1 from the page number 8.

From: KENNEDY, Ben <ben.kennedy@oup.com>
Sent: 30 November 2016 10:27
To: Maciej Rokosz
Subject: FW: Academic Permissions Request Form

Dear Maciej,
Thank you for your enquiry. You have our permission to use the OUP Material you list in your email below in your thesis for submission to Imperial College London. If at some future date your thesis is published it will be necessary to re-clear this permission. Please also note that if the material to be used is acknowledged to any other source, you will need to clear permission with the rights holder.

Best wishes,
Ben Kennedy
Permissions Team Lead
Academic Rights & Journals
Permissions
Oxford University Press
Great Clarendon Street
Oxford
OX2 6DP
Direct tel. +44 (0)1865 354728
Direct fax +44 (0)1865 353429
e mail: ben.kennedy@oup.com